

Projections of future physical and biogeochemical conditions in the Gulf of St. Lawrence, on the Scotian Shelf and in the Gulf of Maine

Diane Lavoie, Nicolas Lambert, Shani Rousseau, Jacqueline Dumas, Joël Chassé, Zhenxia Long, William Perrie, Michel Starr, David Brickman, and Kumiko Azetsu-Scott

Pelagic and Ecosystem Science Branch
Maurice Lamontagne Institute
P. O. Box 1000
850 route de la mer
Mont-Joli (Québec)
G5H 3Z4

2020

**Canadian Technical Report of
Hydrography and Ocean Sciences 334**



Fisheries and Oceans
Canada

Pêches et Océans
Canada

Canada

Canadian Technical Report of Hydrography and Ocean Sciences

Technical reports contain scientific and technical information of a type that represents a contribution to existing knowledge but which is not normally found in the primary literature. The subject matter is generally related to programs and interests of the Oceans and Science sectors of Fisheries and Oceans Canada.

Technical reports may be cited as full publications. The correct citation appears above the abstract of each report. Each report is abstracted in the data base *Aquatic Sciences and Fisheries Abstracts*.

Technical reports are produced regionally but are numbered nationally. Requests for individual reports will be filled by the issuing establishment listed on the front cover and title page.

Regional and headquarters establishments of Ocean Science and Surveys ceased publication of their various report series as of December 1981. A complete listing of these publications and the last number issued under each title are published in the *Canadian Journal of Fisheries and Aquatic Sciences*, Volume 38: Index to Publications 1981. The current series began with Report Number 1 in January 1982.

Rapport technique canadien sur l'hydrographie et les sciences océaniques

Les rapports techniques contiennent des renseignements scientifiques et techniques qui constituent une contribution aux connaissances actuelles mais que l'on ne trouve pas normalement dans les revues scientifiques. Le sujet est généralement rattaché aux programmes et intérêts des secteurs des Océans et des Sciences de Pêches et Océans Canada.

Les rapports techniques peuvent être cités comme des publications à part entière. Le titre exact figure au-dessus du résumé de chaque rapport. Les rapports techniques sont résumés dans la base de données *Résumés des sciences aquatiques et halieutiques*.

Les rapports techniques sont produits à l'échelon régional, mais numérotés à l'échelon national. Les demandes de rapports seront satisfaites par l'établissement auteur dont le nom figure sur la couverture et la page de titre.

Les établissements de l'ancien secteur des Sciences et Levés océaniques dans les régions et à l'administration centrale ont cessé de publier leurs diverses séries de rapports en décembre 1981. Vous trouverez dans l'index des publications du volume 38 du *Journal canadien des sciences halieutiques et aquatiques*, la liste de ces publications ainsi que le dernier numéro paru dans chaque catégorie. La nouvelle série a commencé avec la publication du rapport numéro 1 en janvier 1982.

Canadian Technical Report of
Hydrography and Ocean Sciences 334

2020

PROJECTIONS OF FUTURE PHYSICAL AND BIOCHEMICAL CONDITIONS IN THE
GULF OF ST. LAWRENCE, ON THE SCOTIAN SHELF AND IN THE GULF OF MAINE
USING A REGIONAL CLIMATE MODEL

by

Diane Lavoie¹, Nicolas Lambert², Shani Rousseau¹, Jacqueline Dumas¹, Joël Chassé², Zhenxia Long³, William Perrie³, Michel Starr¹, David Brickman³, and Kumiko Azetsu-Scott³

¹Maurice Lamontagne Institute
Fisheries and Oceans Canada
850, Route de la Mer, P. O. Box 1000
Mont-Joli, Québec, G5H 3Z4

³Bedford Institute of Oceanography
Fisheries and Oceans Canada
P. O. Box 1006
Dartmouth, Nova Scotia, B2Y 4A2

²Gulf Fisheries Centre
Fisheries and Oceans Canada
343 Université Avenue, PO Box 5030
Moncton, New Brunswick, E1C 9B6

© Her Majesty the Queen in Right of Canada, 2020.
Cat. No. Fs 97-18/334E-PDF ISBN 978-0-660-36159-8 ISNN 1488-5417

Correct citation for this publication:

Lavoie, D., Lambert, N., Rousseau, S., Dumas, J., Chassé, J., Long, Z., Perrie, W., Starr, M., Brickman, D., and Azetsu-Scott, K. 2020. Projections of future physical and biochemical conditions in the Gulf of St. Lawrence, on the Scotian Shelf and in the Gulf of Maine using a regional climate model. Can. Tech. Rep. Hydrogr. Ocean Sci. 334: xiii + 102 p.

TABLE OF CONTENT

LIST OF TABLES	iv
LIST OF FIGURES	iv
ABSTRACT.....	xi
RÉSUMÉ	xii
LIST OF ACRONYMS	xiii
1 INTRODUCTION	1
2 MATERIAL AND METHODS	2
2.1 OCEAN MODEL	2
2.2 BIOGEOCHEMICAL MODEL.....	3
2.3 ATMOSPHERIC CONDITIONS	3
2.4 RIVERS.....	3
2.5 OCEANIC BOUNDARY CONDITIONS	4
2.6 EXPERIMENTAL DESIGN.....	5
3 RESULTS	5
3.1 HISTORICAL PERIOD.....	5
3.2 PROJECTIONS.....	7
3.2.1 Sea-ice thickness and concentration	7
3.2.2 Temperature	8
3.2.3 Salinity	8
3.2.4 Stratification.....	9
3.2.5 Nitrate concentration.....	10
3.2.6 Ammonium concentration	10
3.2.7 Diatoms	11
3.2.8 Flagellates	11
3.2.9 Chlorophyll a concentration.....	12
3.2.10 Diatom to flagellate ratio	12
3.2.11 Mesozooplankton.....	13
3.2.12 Microzooplankton	13
3.2.13 Detrital particulate organic nitrogen	14
3.2.14 Dissolved organic nitrogen	14
3.2.15 Dissolved inorganic carbon.....	14
3.2.16 Alkalinity	15
3.2.17 pH.....	16
3.2.18 Aragonite and calcite saturation states.....	16
3.2.19 Time to reach critical aragonite and calcite saturation thresholds.....	17
3.2.20 Cumulative stressors index	18
4 SUMMARY AND DISCUSSION.....	19
4.1 PHYSICAL ENVIRONMENT	19
4.2 BIOLOGICAL VARIABLES	19
4.3 ACIDIFICATION	20
5 CONCLUSION.....	21
ACKNOWLEDGEMENTS.....	23
REFERENCES	24
TABLES	28
FIGURES.....	31

LIST OF TABLES

Table 1. Water temperature trends ($^{\circ}\text{C dec}^{-1}$) over the 1980 to 2099 period in three different depth layers, for the Gulf of St. Lawrence (GSL), Scotian Shelf (SS) and Gulf of Maine (GoM) for the simulations forced with MPI-ESM-LR, HadGEM2-ES, and CanESM2 under the RCP 8.5 scenario.	28
Table 2. Water salinity trends (PSU dec^{-1}) over the 1980 to 2099 period in three different depth layers, for the Gulf of St. Lawrence (GSL), Scotian Shelf (SS) and Gulf of Maine (GoM) for the simulations forced with MPI-ESM-LR, HadGEM2-ES, and CanESM2 under the RCP 8.5 scenario.	28
Table 3. Dissolved inorganic carbon trends ($\text{mmol C m}^{-3} \text{ dec}^{-1}$) over the 1980 to 2099 period in three different depth layers, for the Gulf of St. Lawrence (GSL), Scotian Shelf (SS) and Gulf of Maine (GoM) for the simulations forced with MPI-ESM-LR, HadGEM2-ES, and CanESM2 under the RCP 8.5 scenario.	29
Table 4. Total alkalinity trends ($\text{mmol C m}^{-3} \text{ dec}^{-1}$) over the 1980 to 2099 period in three different depth layers, for the Gulf of St. Lawrence (GSL), Scotian Shelf (SS) and Gulf of Maine (GoM) for the simulations forced with MPI-ESM-LR, HadGEM2-ES, and CanESM2 under the RCP 8.5 scenario.	29
Table 5. pH_{total} trends (units per decade) over the 1980 to 2099 period in three different depth layers, for the Gulf of St. Lawrence (GSL), Scotian Shelf (SS) and Gulf of Maine (GoM) for the simulations forced with MPI-ESM-LR, HadGEM2-ES, and CanESM2 under the RCP 8.5 scenario.	30
Table 6. Aragonite saturation trends (units per decade) over the 1980 to 2099 period in three different depth layers, for the Gulf of St. Lawrence (GSL), Scotian Shelf (SS) and Gulf of Maine (GoM) for the simulations forced with MPI-ESM-LR, HadGEM2-ES, and CanESM2 under the RCP 8.5 scenario.	30

LIST OF FIGURES

Figure 1. Map of the study area showing the model domain, with a small sub-area of the grid in the lower right corner. The 200, 300 and 1000 m depth contours are shown. The transects used in Figures 6 to 19 are depicted in pink (Strait of Belle Isle (BI), Shelf Break (SB) and Gulf Stream (GS)). The arrows indicate the positive direction for the currents in Figure 10.	31
Figure 2. Conceptual planktonic ecosystem model including nitrate (NO_3), ammonium (NH_4), large phytoplankton (LP), small phytoplankton (SP), mesozooplankton (MEZ), microzooplankton (MIZ), detrital particulate organic nitrogen (PON), and dissolved organic nitrogen (DON). The dark blue arrows represent nitrogen fluxes between the biological components. The pale blue arrow represents the oxygen (O_2) fluxes (production, consumption and air-sea exchange) and the green arrow represents the air-sea carbon dioxide (CO_2) fluxes and the dissolved inorganic carbon production and consumption.	32
Figure 3. Concentration of carbon dioxide (CO_2) in the atmosphere (ppm) for the Representative Concentration Pathway RCP 8.5.	32
Figure 4. Upper panel (map): Mean discharge of the 78 rivers flowing into the model domain calculated with the hydrological model (Lambert et al., 2013) using precipitation and evaporation from the three Earth System Models averaged over the 1970-2099 period. The mean discharge of 4 majors rivers (A. St. Lawrence, B. Saguenay, C. Manicouagan, D. St. John) is displayed on the left-hand side of the panel. Four lower panels: Annual runoff calculated with each model, and corresponding total river flux of dissolved inorganic carbon (mol C s^{-1}), alkalinity (mol C s^{-1}), and nitrate (mol N s^{-1}).	33
Figure 5. A) Normalized annual cycle of surface nitrate (NO_3) concentration (mmol N m^{-3}) calculated from the surface 2D fields of MPI-ESM-LR at a randomly selected location at the southwest end of the domain. One out of four years (between 2061 and 2070) are shown in gray and the red line shows year 2061. The corresponding annual anomaly calculated from the 3D field is displayed as a dashed line. (B) Schematic of how the anomalies for the biogeochemical variables are applied at the open boundary for every month of each year. The monthly nitrate concentration at the boundary is obtained by adding/removing the monthly anomaly to/from the climatological value. For grid cells above the mixed layer (in green), depicted by the black line, the monthly anomaly estimated in (A) is used. For grid cells below the mixed layer (in blue), the annual anomaly calculated from the 3D fields is used.	34

Figure 6. Mean observed temperature ($^{\circ}\text{C}$) from 1991 to 2010 (climatology) and 1970 to 2099 trends ($^{\circ}\text{C dec}^{-1}$) from the three Earth System Models (MPI-ESM-LR, HadGEM2-ES, and CanESM2), under the RCP 8.5 scenario, that are applied to the climatological values to obtain past and future conditions at the open boundaries. The open boundaries are displayed in the upper panel inset.	35
Figure 7. Yearly mean temperature and decadal trends for the 0-50 m or 100-400 m depth intervals across three open boundary zones (BI, SB, GS) defined in Figure 1, with the three Earth System Models (MPI-ESM-LR, HadGEM2-ES, and CanESM2) under the RCP 8.5 scenario.	36
Figure 8. Mean observed salinity (psu) from 1991 to 2010 (climatology) and 1970 to 2099 trends (psu dec^{-1}) from the three Earth System Models (MPI-ESM-LR, HadGEM2-ES, and CanESM2), under the RCP 8.5 scenario, that are applied to the climatological values to obtain past and future conditions at the open boundaries. The open boundaries are displayed in the upper panel inset.	37
Figure 9. Yearly mean salinity and decadal trends for the 0-50 m or 100-400 m depth intervals across three open boundary zones (BI, SB, GS) defined in Figure 1, with the three Earth System Models (MPI-ESM-LR, HadGEM2-ES, and CanESM2) under the RCP 8.5 scenario.	38
Figure 10. Mean perpendicular current over the 1991 to 2010 period (positive values indicate inflow into the domain, see Figure 1). Future trends at the open boundaries for the three Earth System Models (MPI-ESM-LR, HadGEM2-ES, and CanESM2) under the RCP 8.5 scenario. The trends are applied to the climatological values to obtain past and future boundary conditions.	39
Figure 11. Yearly mean transport (Sv , $1 \text{ Sv} = 10^6 \text{ m}^3 \text{ s}^{-1}$) and decadal trends (Sv per decade) for the 0-50 m or 100-400 m depth intervals across three open boundary zones (BI, SB, GS) defined in Figure 1, with the three Earth System Models (MPI-ESM-LR, HadGEM2-ES, and CanESM2) under the RCP 8.5 scenario.	40
Figure 12. Mean nitrate concentration over 1991 to 2010 (climatology) and 1970 to 2099 trends at the open boundaries from the three Earth System Models (MPI-ESM-LR, HadGEM2-ES, and CanESM2), under the RCP 8.5 scenario, that are applied to the climatological values to obtain past and future boundary conditions. The open boundaries are displayed in the upper panel inset.	41
Figure 13. Yearly mean nitrate concentration and decadal trends for the 0-50 m or 100-400 m depth intervals across three open boundary zones (BI, SB, and GS) defined in Figure 1, with the three Earth System Models (MPI-ESM-LR, HadGEM2-ES, and CanESM2) under the RCP 8.5 scenario.	42
Figure 14. Mean dissolved oxygen concentration ($\text{mmol O}_2 \text{ m}^{-3}$) over 1991 to 2010 (climatology) and 1970 to 2099 trends ($\text{mmol O}_2 \text{ m}^{-3} \text{ dec}^{-1}$) at the open boundaries from the two Earth System Models (MPI-ESM-LR and HadGEM2-ES), and CanESM2) under the RCP 8.5 scenario. CanESM2 did not calculate oxygen concentration so we used the mean of the 7 ESMs available (Lavoie et al., 2019). These trends are applied to the climatological values to obtain future boundary conditions. The open boundaries are displayed in the upper panel inset.	43
Figure 15. Yearly mean dissolved oxygen concentration and decadal trends for the 0-50 m or 100-400 m depth intervals across three open boundary zones (BI, SB, GS) defined in Figure 1, with two Earth System Models (MPI-ESM-LR and HadGEM2-ES) under the RCP 8.5 scenario. CanESM2 did not calculate oxygen concentration so we used the mean of the 7 ESMs available (Lavoie et al., 2019).	44
Figure 16. Mean dissolved inorganic carbon concentration over 1991 to 2010 (climatology) and 1970 to 2099 trends at the open boundaries from the three Earth System Models (MPI-ESM-LR, HadGEM2-ES, and CanESM2), under the RCP 8.5 scenario, that are applied to the climatological values to obtain past and future boundary conditions. The open boundaries are displayed in the upper panel inset.	45
Figure 17. Yearly mean dissolved inorganic carbon (DIC) and decadal trends for the 0-50 m or 100-400 m depth intervals across three open boundary zones (BI, SB, GS) defined in Figure 1, with the three Earth System Models (MPI-ESM-LR, HadGEM2-ES, and CanESM2) under the RCP 8.5 scenario.	46
Figure 18. Mean total alkalinity over 1991 to 2010 (climatology) and 1970 to 2099 trends at the open boundaries from the three Earth System Models (MPI-ESM-LR, HadGEM2-ES, and CanESM2) under the RCP 8.5 scenario, that are applied to the climatological values to obtain past and future boundary conditions. The open boundaries are displayed in the upper panel inset.	47
Figure 19. Yearly mean total alkalinity and 1970 to 2099 decadal trends for the 0-50 m or 100-400 m depth intervals across three open boundary zones (BI, SB, GS) defined in Figure 1, with the three Earth System Models (MPI-ESM-LR, HadGEM2-ES, and CanESM2) under the RCP 8.5 scenario.	48
Figure 20. Taylor (left) and Target (right) diagrams for eight variables (see symbols in the box) for the three simulations (forced with MPI-ESM-LR in blue, with HadGEM2-ES in green, and with CANESM2 in red) for the Gulf of St. Lawrence (see inset in the top right corner). Model output averaged over 14.6 days is compared with in situ data.	49

Figure 21. Taylor (left) and Target (right) diagrams for eight variables (see symbols in the box) for the three simulations (forced with MPI-ESM-LR in blue, with HadGEM2-ES in green, and with CANESM2 in red) for the Scotian Shelf (see inset in the top right corner). Model output averaged over 14.6 days is compared with in situ data.	49
Figure 22. Taylor (left) and Target (right) diagrams for eight variables (see symbols in the box) for the three simulations (forced with MPI-ESM-LR in blue, with HadGEM2-ES in green, and with CANESM2 in red) for the Gulf of Maine (see inset in the top right corner). Model output averaged over 14.6 days is compared with in situ data.	50
Figure 23. Regions used for the trend analysis in the Gulf of St. Lawrence (red box) and seasonal changes.	51
Figure 24. A) Ensemble mean sea-ice thickness (m) over the 1991-2010 period for the simulations forced with MPI-ESM-LR, HadGEM2-ES, and CanESM2 under the RCP 8.5 scenario, B) Mean sea-ice thickness over the 2061-2080 period for each simulation, and C) inter-model change spread in mean sea-ice thickness. In panel B), the dots represent the area where the future change is greater than three times the standard deviation calculated over the historical period, and where all three simulations agree on the sign of change (positive or negative).....	52
Figure 25. A) Ensemble mean sea-ice fraction over the 1991-2010 period for the simulations forced with MPI-ESM-LR, HadGEM2-ES, and CanESM2 under the RCP 8.5 scenario, B) Mean sea-ice fraction over the 2061-2080 period for each simulation, and C) inter-model change spread. In panel B), the dots represent the area where the future change is greater than three times the standard deviation calculated over the historical period, and where all three simulations agree on the sign of change (positive or negative).	53
Figure 26. A) Ensemble mean water temperature (°C) over the 1991-2010 period at four depth intervals (0-50 m, 50-150 m, 150-300 m, and bottom) for the simulations forced with MPI-ESM-LR, HadGEM2-ES, and CanESM2 under the RCP 8.5 scenario, B) Bidecadal temperature change (2061-2080 average minus 1991-2010 average) for each simulation, and C) inter-model change spread. In panel B), the dots represent the area where the future change is greater than three times the standard deviation calculated over the historical period, and where all three simulations agree on the sign of change (positive or negative).	54
Figure 27. Gulf of St. Lawrence annual mean water temperature (°C) at three depth intervals (0-50 m, 50-150 m and 150-300 m), along with the trend (dashed lines, °C per decade) calculated from 1980 to 2099 for the simulations forced with MPI-ESM-LR, HadGEM2-ES, and CanESM2 under the RCP 8.5 scenario. The gray areas cover the historical and future time periods represented in the maps (Figure 26).	55
Figure 28. A) Ensemble mean water salinity (psu) over the 1991-2010 period at four depth intervals (0-50 m, 50-150 m, 150-300 m, and bottom) for the simulations forced with MPI-ESM-LR, HadGEM2-ES, and CanESM2 under the RCP 8.5 scenario, B) Bidecadal salinity change (2061-2080 average minus 1991-2010 average) for each simulation, and C) inter-model change spread. In panel B), the dots represent the area where the future change is greater than three times the standard deviation calculated over the historical period, and where all three simulations agree on the sign of change (positive or negative).....	56
Figure 29. Gulf of St. Lawrence annual mean water salinity (psu) at three depth intervals (0-50 m, 50-150 m and 150-300 m), along with the trend (dashed lines, psu per decade) calculated from 1980 to 2099 for the simulations forced with MPI-ESM-LR, HadGEM2-ES, and CanESM2 under the RCP 8.5 scenario. The gray areas cover the historical and future time periods represented in the maps and in the annual cycle (Figures 28, 30 and 31).	57
Figure 30. Mean salinity annual cycle inside the zones defined in Figure 23 at the 0-50 m depth interval, for the simulations forced with MPI-ESM-LR, HadGEM2-ES, and CanESM2 under the RCP 8.5 scenario. The annual cycle is defined as the average of each step (25 per year) for the 20 years of the historical (solid lines) and the future periods (dashed lines).....	58
Figure 31. Mean salinity annual cycle inside the zones defined in Figure 23 at the 50-150 m depth interval, for the simulations forced with MPI-ESM-LR, HadGEM2-ES, and CanESM2 under the RCP 8.5 scenario. The annual cycle is defined as the average of each step (25 per year) for the 20 years of the historical (solid lines) and the future periods (dashed lines).....	59
Figure 32. A) Ensemble mean stratification (kg m^{-3}) over the 1991-2010 period at the 0-50 m depth interval for the simulations forced with MPI-ESM-LR, HadGEM2-ES and CanESM2 under the RCP 8.5 scenario, B) Bidecadal stratification change (2061-2080 average minus 1991-2010 average) for each simulation, and C) inter-model change spread. In panel B), the dots represent the area where the future change is greater than three times the standard deviation calculated over the historical period, and where all three simulations agree on the sign of change (positive or negative).....	60

Figure 33. Annual mean stratification in the Gulf of St. Lawrence at the 0-50 m depth interval, along with the trend (dashed lines, kg m^{-3} per decade), calculated from 1980-2099 for the simulations forced with MPI-ESM-LR, HadGEM2-ES, and CanESM2 under the RCP 8.5 scenario. The gray areas cover the historical and future time periods represented in the maps and in the annual cycle (Figures 32 and 34).	61
Figure 34. Mean stratification ($\sigma_{50\text{m}} - \sigma_{0\text{m}}$) annual cycle inside the zones defined in Figure 23 at the 0-50 m depth interval, for the simulations forced with MPI-ESM-LR, HadGEM2-ES, and CanESM2 under the RCP 8.5 scenario. The annual cycle is defined as the average of each step (25 per year) for the 20 years of the historical (solid lines) and the future periods (dashed lines).	62
Figure 35. A) Ensemble mean nitrate concentration (mmol N m^{-3}) over the 1991-2010 period at four depth intervals (0-50 m, 50-150 m, 150-300 m, and bottom) for the simulations forced with MPI-ESM-LR, HadGEM2-ES, and CanESM2 under the RCP 8.5 scenario, B) Bidecadal nitrate concentration change (2061-2080 average minus 1991-2010 average) for each simulation, and C) inter-model change spread. Note that the color scale is sometimes different for the different depth layers. In panel B), the dots represent the area where the future change is greater than three times the standard deviation calculated over the historical period, and where all three simulations agree on the sign of change (positive or negative).	63
Figure 36. Gulf of St. Lawrence annual mean nitrate concentration at three depth intervals (0-50 m, 50-150 m and 150-300 m), along with the trend (dashed lines, mmol N m^{-3} per decade) calculated from 1980-2099 for simulations forced with MPI-ESM-LR, HadGEM2-ES, and CanESM2 under the RCP 8.5 scenario. The gray areas cover the historical and future time periods represented in the maps and in the annual cycle (Figures 35 and 37).	64
Figure 37. Mean nitrate concentration annual cycle inside the zones defined in Figure 23 at the 0-50 m depth interval, for the simulations forced with MPI-ESM-LR, HadGEM2-ES and CanESM2 under the RCP 8.5 scenario. The annual cycle is defined as the average of each step (25 per year) for the 20 years of the historical (solid lines) and the future periods (dashed lines).	65
Figure 38. A) Ensemble mean ammonium concentration (mmol N m^{-3}) over the 1991-2010 period at four depth intervals (0-50 m, 50-150 m, 150-300 m, and bottom) for the simulations forced with MPI-ESM-LR, HadGEM2-ES, and CanESM2 under the RCP 8.5 scenario, B) Bidecadal ammonium concentration change (2061-2080 average minus 1991-2010 average) for each simulation, and C) inter-model change spread. Note that the color scale is sometimes different for the different depth layers. In panel B), the dots represent the area where the future change is greater than three times the standard deviation calculated over the historical period, and where all three simulations agree on the sign of change (positive or negative).	66
Figure 39. Gulf of St. Lawrence annual mean ammonium concentration at three depth intervals (0-50 m, 50-150 m and 150-300 m), along with the trend (dashed lines, mmol N m^{-3} per decade) calculated from 1980-2099 for the simulations forced with MPI-ESM-LR, HadGEM2-ES, and CanESM2 under the RCP 8.5 scenario. The gray areas cover the historical and future time periods represented in the maps and in the annual cycle (Figures 38 and 40).	67
Figure 40. Mean ammonium concentration annual cycle inside the zones defined in Figure 23 at the 0-50 depth interval, for the simulations forced with MPI-ESM-LR, HadGEM2-ES, and CanESM2 under the RCP 8.5 scenario. The annual cycle is defined as the average of each step (25 per year) for the 20 years of the historical (solid lines) and the future periods (dashed lines).	68
Figure 41. A) Ensemble mean annual diatom-N concentration (mmol N m^{-3}) over the 1991-2010 period at the 0-50 m depth interval, for the simulations forced with MPI-ESM-LR, HadGEM2-ES, and CanESM2 under the RCP 8.5 scenario, B) Bidecadal diatom-N concentration change (2061-2080 average minus 1991-2010 average) for each simulation, and C) inter-model change spread. In panel B) the dots represent the area where the change is greater than three times the historical standard deviation over the historical period and where all three simulations agree on the direction of change (increase or decrease).	69
Figure 42. Gulf of St. Lawrence annual mean diatom-N concentration at the 0-50 m depth interval, along with the trend (dashed lines, mmol N m^{-3} per decade) calculated from 1980-2099 for the simulations forced with MPI-ESM-LR, HadGEM2-ES, and CanESM2 under the RCP 8.5 scenario. The gray areas cover the historical and future time periods represented in the maps (Figure 41).	70
Figure 43. A) Ensemble mean annual flagellate-N concentration (mmol N m^{-3}) over the 1991-2010 period at the 0-50 m depth interval for the simulations forced with MPI-ESM-LR, HadGEM2-ES, and CanESM2 under the RCP 8.5 scenario, B) Bidecadal flagellate concentration change (2061-2080 average minus 1991-2010 average) for each simulation, and C) inter-model change spread. In panel B) the dots represent the area where the change is greater than three times the historical standard deviation over the historical period and where all three simulations agree on the direction of change (increase or decrease).	71

Figure 44. Gulf of St. Lawrence annual mean flagellate-N concentration at the 0-50 m depth interval, along with the trend (dashed lines, mmol N m^{-3} per decade) calculated from 1980-2099 for the simulations forced with MPI-ESM-LR, HadGEM2-ES, and CanESM2) under the RCP 8.5 scenario. The gray areas cover the historical and future time periods represented in the maps (Figure 43).	72
Figure 45. A) Ensemble mean annual chlorophyll <i>a</i> biomass ($\text{mg chl } a \text{ m}^{-2}$) over the 1991-2010 period at the 0-50 m depth interval for the simulations forced with MPI-ESM-LR, HadGEM2-ES, and CanESM2 under the RCP 8.5 scenario, B) Bidecadal chlorophyll <i>a</i> biomass change (2061-2080 average minus 1991-2010 average) for each simulation, and C) inter-model change spread. In panel B) the dots represent the area where the change is greater than three times the historical standard deviation over the historical period and where all three simulations agree on the direction of change (increase or decrease).	73
Figure 46. Mean chlorophyll <i>a</i> biomass annual cycle inside the zones defined in Figure 23 at the 0-50 m depth interval, for the simulations forced with MPI-ESM-LR, HadGEM2-ES, and CanESM2 under the RCP 8.5 scenario. The annual cycle is defined as the average of each step (25 per year) for the 20 years of the historical (solid lines) and the future periods (dashed lines).	74
Figure 47. A) Ensemble mean diatom to flagellate ratio (mol N:mol N) over the 1991-2010 period at the 0-50 m depth interval for the simulations forced with MPI-ESM-LR, HadGEM2-ES, and CanESM2 under the RCP 8.5 scenario, B) Bidecadal diatom/flagellate ratio change (2061-2080 average minus 1991-2010 average) for each simulation, and C) inter-model change spread. In panel B) the dots represent the area where the change is greater than three times the historical standard deviation over the historical period and where all three simulations agree on the direction of change (increase or decrease).	75
Figure 48. Gulf of St. Lawrence annual mean diatom to flagellate ratio (mol N:mol N) at the 0-50 m depth interval, along with the trend (dashed lines) calculated from 1980-2099 for the simulations forced with MPI-ESM-LR, HadGEM2-ES, and CanESM2 under the RCP 8.5 scenario. The gray areas cover the historical and future time periods represented in the maps and in the annual cycle (Figures 47 and 49).	76
Figure 49. Mean diatom to flagellate ratio (mol N:mol N) annual cycle inside the zones defined in Figure 23 at the 0-50 m depth interval, for the simulations forced with MPI-ESM-LR, HadGEM2-ES, and CanESM2 under the RCP 8.5 scenario. The annual cycle is defined as the average of each step (25 per year) for the 20 years of the historical (solid lines) and the future periods (dashed lines).	77
Figure 50. A) Ensemble mean mesozooplankton-N concentration (mmol N m^{-3}) over the 1991-2010 period for the 0-50 m depth interval for the simulations forced with MPI-ESM-LR, HadGEM2-ES, and CanESM2 under the RCP 8.5 scenario, B) Bidecadal mesozooplankton-N concentration change (2061-2080 average minus 1991-2010 average) for each simulation, and C) inter-model change spread. In panel B), the dots represent the area where the future change is greater than three times the standard deviation calculated over the historical period, and where all three simulations agree on the sign of change (positive or negative).	78
Figure 51. Gulf of St. Lawrence annual mean mesozooplankton-N concentration at the 0-50 m depth interval, along with the trend (dashed lines, mmol N m^{-3} per decade) calculated from 1980-2099 for the simulations forced with MPI-ESM-LR, HadGEM2-ES, and CanESM2 under the RCP 8.5 scenario. The gray areas cover the historical and future time periods represented in the maps and in the annual cycle (Figures 50 and 52).	79
Figure 52. Mean mesozooplankton-N concentration annual cycle inside the zones defined in Figure 23 at the 0-50 m depth interval, for the simulations forced with MPI-ESM-LR, HadGEM2-ES, and CanESM2 under the RCP 8.5 scenario. The annual cycle is defined as the average of each step (25 per year) for the 20 years of the historical (solid lines) and the future periods (dashed lines).	80
Figure 53. A) Ensemble mean microzooplankton-N concentration (mmol N m^{-3}) over the 1991-2010 period for the 0-50 m depth interval for the simulations forced with MPI-ESM-LR, HadGEM2-ES, and CanESM2 under the RCP 8.5 scenario, B) Bidecadal microzooplankton-N concentration change (2061-2080 average minus 1991-2010 average) for each simulation, and C) inter-model change spread. In panel B), the dots represent the area where the future change is greater than three times the standard deviation calculated over the historical period, and where all three simulations agree on the sign of change (positive or negative).	81
Figure 54. Gulf of St. Lawrence annual mean microzooplankton-N concentration at the 0-50 m depth interval, along with the trend (dashed lines, mmol N m^{-3} per decade) calculated from 1980-2099 for the simulations forced with MPI-ESM-LR, HadGEM2-ES, and CanESM2 under the RCP 8.5 scenario. The gray areas cover the historical and future time periods represented in the maps and in the annual cycle (Figures 53 and 55).	82
Figure 55. Mean microzooplankton-N concentration annual cycle inside the zones defined in Figure 23 at the 0-50 m depth interval, for the simulations forced with MPI-ESM-LR, HadGEM2-ES, and CanESM2 under the RCP 8.5 scenario. The annual cycle is defined as the average of each step (25 per year) for the 20 years of the historical (solid lines) and the future periods (dashed lines).	83

Figure 56. A) Ensemble mean detrital particulate organic nitrogen (PON) concentration (mmol N m^{-3}) over the 1991-2010 period at four depth intervals (0-50 m, 50-150 m, 150-300 m, and bottom) for the simulations forced with MPI-ESM-LR, HadGEM2-ES, and CanESM2 under the RCP 8.5 scenario, B) Bidecadal particulate organic nitrogen concentration change (2061-2080 average minus 1991-2010 average) for each simulation, and C) inter-model change spread. Note that the color scale is sometimes different for the different depth layers. In panel B), the dots represent the area where the future change is greater than three times the standard deviation calculated over the historical period, and where all three simulations agree on the sign of change (positive or negative).	84
Figure 57. Gulf of St. Lawrence annual mean detrital particulate organic nitrogen (PON) concentration at three depth intervals (0-50 m, 50-150 m and 150-300 m), along with the trend (dashed lines, mmol N m^{-3} per decade) calculated from 1980-2099 for the simulations forced with MPI-ESM-LR, HadGEM2-ES, and CanESM2 under the RCP 8.5 scenario. The gray areas cover the historical and future time periods represented in the maps (Figure 56).	85
Figure 58. Mean detrital particulate organic matter (PON) concentration annual cycle inside the zones defined in Figure 23 at the 0-50 m depth interval, for the simulations forced with MPI-ESM-LR, HadGEM2-ES, and CanESM2 under the RCP 8.5 scenario. The annual cycle is defined as the average of each step (25 per year) for the 20 years of the historical (solid lines) and the future periods (dashed lines).	86
Figure 59. A) Ensemble mean dissolved organic nitrogen (DON) concentration (mmol N m^{-3}) over the 1991-2010 period at four depth intervals (0-50 m, 50-150 m, 150-300 m, and bottom) for the simulations forced with MPI-ESM-LR, HadGEM2-ES, and CanESM2 under the RCP 8.5 scenario, B) Bidecadal dissolved organic nitrogen concentration change (2061-2080 average minus 1991-2010 average) for each simulation, and C) inter-model change spread. Note that the color scale is sometimes different for the different depth layers. In panel B), the dots represent the area where the future change is greater than three times the standard deviation calculated over the historical period, and where all three simulations agree on the sign of change (positive or negative).	87
Figure 60. Gulf of St. Lawrence annual mean dissolved organic nitrogen (DON) concentration at three depth intervals (0-50 m, 50-150 m and 150-300 m), along with the trend (dashed lines, mmol N m^{-3} per decade) calculated from 1980-2099 for the simulations forced with MPI-ESM-LR, HadGEM2-ES, and CanESM2 under the RCP 8.5 scenario. The gray areas cover the historical and future time periods represented in the maps (Figure 59).	88
Figure 61. Mean dissolved organic matter (DON) concentration annual cycle inside the zones defined in Figure 23 at the 0-50 m depth interval, for the simulations forced with MPI-ESM-LR, HadGEM2-ES, and CanESM2 under the RCP 8.5 scenario. The annual cycle is defined as the average of each step (25 per year) for the 20 years of the historical (solid lines) and the future periods (dashed lines).	89
Figure 62. A) Ensemble mean dissolved inorganic carbon (DIC) concentration (mmol C m^{-3}) over the 1991-2010 period at four depth intervals (0-50 m, 50-150 m, 150-300 m, and bottom) for the simulations forced with MPI-ESM-LR, HadGEM2-ES, and CanESM2 under the RCP 8.5 scenario, B) Bidecadal dissolved inorganic carbon concentration change (2061-2080 average minus 1991-2010 average) for each simulation, and C) inter-model change spread. Note that the color scale is sometimes different for the different depth layers. In panel B), the dots represent the area where the future change is greater than three times the standard deviation calculated over the historical period, and where all three simulations agree on the sign of change (positive or negative).	90
Figure 63. Gulf of St. Lawrence annual mean dissolved inorganic carbon (DIC) concentration at three depth intervals (0-50 m, 50-150 m and 150-300 m), along with the trend (dashed lines, mmol C m^{-3} per decade) calculated from 1980-2099 for the simulations forced with MPI-ESM-LR, HadGEM2-ES, and CanESM2 under the RCP 8.5 scenario. The gray areas cover the historical and future time periods represented in the maps (Figure 62).	91
Figure 64. A) Ensemble mean alkalinity (mmol C m^{-3}) over the 1991-2010 period at four depth intervals (0-50 m, 50-150 m, 150-300 m, and bottom) for the simulations forced with MPI-ESM-LR, HadGEM2-ES, and CanESM2 under the RCP 8.5 scenario, B) Bidecadal alkalinity change (2061-2080 average minus 1991-2010 average) for each simulation, and C) inter-model change spread. Note that the color scale is sometimes different for the different depth layers. In panel B), the dots represent the area where the future change is greater than three times the standard deviation calculated over the historical period, and where all three simulations agree on the sign of change (positive or negative).	92
Figure 65. Gulf of St. Lawrence annual mean alkalinity at three depth intervals (0-50 m, 50-150 m and 150-300 m), along with the trend (dashed lines, mmol C m^{-3} per decade) calculated from 1980-2099 for the simulations	

forced MPI-ESM-LR, HadGEM2-ES, and CanESM2 under the RCP 8.5 scenario. The gray areas cover the historical and future time periods represented in the maps (Figure 64).	93
Figure 66. A) Ensemble mean pH_{total} over the 1991-2010 period at four depth intervals (0-50 m, 50-150 m, 150-300 m, and bottom) for the simulations forced with MPI-ESM-LR, HadGEM2-ES, and CanESM2 under the RCP 8.5 scenario, B) Bidecadal pH_{total} change (2061-2080 average minus 1991-2010 average) for each simulation, and C) inter-model change spread. Note that the color scale is sometimes different for the different depth layers. In panel B), the dots represent the area where the future change is greater than three times the standard deviation calculated over the historical period, and where all three simulations agree on the sign of change (positive or negative).	94
Figure 67. Annual mean pH_{total} in the Gulf of St. Lawrence at three depth intervals (0-50 m, 50-150 m and 150-300 m), along with the trend (dashed lines) calculated from 1980-2099 for the simulations forced MPI-ESM-LR, HadGEM2-ES, and CanESM2 under the RCP 8.5 scenario. The gray areas cover the historical and future time periods represented in the maps (Figure 66).	95
Figure 68. A) Ensemble mean aragonite saturation state (Ω_{arag}) over the 1991-2010 period at four depth intervals (0-50 m, 50-150 m, 150-300 m, and bottom) for the simulations forced with MPI-ESM-LR, HadGEM2-ES, and CanESM2 under the RCP 8.5 scenario. The white line represent the $\Omega_{arag}=1$ threshold and the area bathing in water with $\Omega_{arag}<1$ is indicated at the bottom of the graph. B) Bidecadal aragonite saturation state change (2061-2080 average minus 1991-2010 average) for each simulation, and C) inter-model change spread. In panel B), the dots represent the area where the future change is greater than three times the standard deviation calculated over the historical period, and where all three simulations agree on the sign of change (positive or negative).	96
Figure 69. Annual mean aragonite saturation state (Ω_{arag}) in the Gulf of St. Lawrence at three depth intervals (0-50 m, 50-150 m and 150-300 m), along with the trend (dashed lines) calculated from 1980-2099 for the simulations forced MPI-ESM-LR, HadGEM2-ES, and CanESM2 under the RCP 8.5 scenario. The gray areas cover the historical and future time periods represented in the maps (Figure 68).	97
Figure 70. A) Ensemble mean calcite saturation state (Ω_{cal}) over the 1991-2010 period at four depth intervals (0-50 m, 50-150 m, 150-300 m, and bottom) for the simulations forced with MPI-ESM-LR, HadGEM2-ES, and CanESM2 under the RCP 8.5 scenario. The white line represent the $\Omega_{cal}=1$ threshold and the area bathing in water with $\Omega_{cal}<1$ is indicated at the bottom of the graph. B) Bidecadal calcite saturation state change (2061-2080 average minus 1991-2010 average) for each simulation, and C) inter-model change spread. In panel B), the dots represent the area where the future change is greater than three times the standard deviation calculated over the historical period, and where all three simulations agree on the sign of change (positive or negative).	98
Figure 71. Annual mean calcite saturation state (Ω_{cal}) in the Gulf of St. Lawrence at three depth intervals (0-50 m, 50-150 m and 150-300 m), along with the trend (dashed lines) calculated from 1980-2099 for the simulations forced MPI-ESM-LR, HadGEM2-ES, and CanESM2 under the RCP 8.5 scenario. The gray areas cover the historical and future time periods represented in the maps and in the annual cycle (previous and next figures).	99
Figure 72. Year at which the surface and bottom aragonite saturation state (Ω_{arag}) reach a value of 1.0 (A) and a value of 1.5 (B). White areas mean that saturation states do not reach these critical values during the study period. Right panels show the inter-model change spread in the calculated year.	100
Figure 73. Year at which the surface and bottom calcite saturation states (Ω_{cal}) reach a value of 1.0 (A) and a value of 1.5 (B). White areas mean that saturation states do not reach these critical values during the study period. Right panels show the inter-model change spread in the calculated year.	101
Figure 74. Number of variables in each grid cell that show a change (2061-2080 average minus 1991-2010 average) greater than three times the standard deviation calculated over the historical period. The 12 variables considered are temperature, salinity, nitrate, ammonium, diatoms, flagellates, mesozooplankton, microzooplankton, detrital particulate organic nitrogen, dissolved organic nitrogen, pH, and aragonite saturation. The reader can refer to the bi-decadal change figures for each variable to determine which ones are included here.	102

ABSTRACT

Lavoie, D., Lambert, N., Rousseau, S., Dumas, J., Chassé, J., Long, Z., Perrie, W., Starr, M., Brickman, D., and Azetsu-Scott, K. 2020. Projections of future physical and biochemical conditions in the Gulf of St. Lawrence, on the Scotian Shelf and in the Gulf of Maine using a regional climate model. *Can. Tech. Rep. Hydrogr. Ocean Sci.* 334: xiii + 102 p.

A regional climate model is used to make projections of future physical and biogeochemical conditions in the Gulf of St. Lawrence (GSL), Scotian Shelf, and Gulf of Maine. The regional climate model is forced with downscaled atmosphere from three Earth System Models (CanESM2, MPI-ESM-LR, and HadGEM-ES) using the Representative Concentration Pathway 8.5. We use the Earth System Model outputs made available in 2013 through the Coupled Model Intercomparison Project Phase 5 (CMIP5) archive. The regional model was run from 1970 to 2100. Results are presented for sea ice, water temperature, salinity, stratification, nitrate, ammonium, diatoms, flagellates, mesozooplankton, microzooplankton, detrital particulate organic matter, dissolved organic matter, dissolved inorganic carbon, alkalinity, and calcium carbonate (aragonite and calcite) saturation states. We mapped the changes that occurred between the 2061-2080 period and the 1991-2010 period, provided linear trends of the different environmental variables for specific regions, computed model ensemble statistics, calculated the year when calcium carbonate saturation will reach some critical threshold over the model domain, and identified areas where multiple important changes will occur. The results show a decrease in sea ice, a general warming, a decrease in salinity in the upper layers and an increase at depth, as well as an increase in stratification. Projected future changes in nitrogenous nutrients are variable and generally not significant when considering the three simulations together. The chlorophyll *a* biomass decreases in the GSL and on the eastern Scotian Shelf but increases elsewhere. All the simulations show acidification over the model domain with a decrease in pH and carbonate saturations at all depths. By 2090 the aragonite saturation level of 1 is reached over most of the domain on the bottom and at the surface of the GSL and Scotian Shelf. Calcite saturations also reach this critical level on the bottom of the Magdalen Shallows and eastern Scotian Shelf.

RÉSUMÉ

Lavoie, D., Lambert, N., Rousseau, S., Dumas, J., Chassé, J., Long, Z., Perrie, W., Starr, M., Brickman, D., and Azetsu-Scott, K. 2020. Projections of future physical and biochemical conditions in the Gulf of St. Lawrence, on the Scotian Shelf and in the Gulf of Maine using a regional climate model. *Can. Tech. Rep. Hydrogr. Ocean Sci.* 334: xiii + 102 p.

Un modèle climatique régional est utilisé pour projeter les conditions physiques et biogéochimiques futures dans le Golfe du Saint-Laurent (GSL), le plateau Néo-Écossais et le Golfe du Maine. Le modèle climatique régional est forcé par une réduction d'échelle des conditions atmosphériques produites par trois modèles du système terrestre (CanESM2, MPI-ESM-LR, and HadGEM-ES) utilisant le scénario d'émission « Profil représentatif d'évolution de concentration 8.5 ». Nous utilisons les résultats des modèles du système terrestre qui étaient disponibles sur le site du 5^e Projet d'Inter-Comparaison de Modèles Couplés (CMIP5) en 2013. La simulation effectuée avec le modèle régional à réduction d'échelle s'étend de 1970 à 2100. Les résultats des simulations sont présentés pour la glace de mer, la température et la salinité de l'eau, la stratification, les concentrations de nitrate, d'ammonium, de diatomées, de flagellées, de mesozooplankton, de microzooplankton, de matière organique particulaire (détritique) et dissoute, de carbone inorganique dissous, et pour l'alkalinité, le pH et les conditions de saturation en carbonate de calcium (aragonite et calcite). Nous avons cartographié les changements entre les conditions moyennes de la période 1991-2010 avec celles de 2061-2080 et certaines statistiques d'ensemble (moyenne et étendue de l'ensemble des simulations). Les tendances linéaires des différentes variables environnementales ont aussi été calculées sur certaines régions spécifiques entre 1980 et 2100. Nous avons calculé les années où les états de saturation de l'aragonite et de la calcite vont atteindre des seuils critiques, et ce sur l'ensemble du domaine. Finalement, nous identifions les régions où des changements importants vont se produire avec plusieurs des variables analysées. Les résultats indiquent une diminution du couvert de glace, un réchauffement généralisé de l'eau, une diminution de la salinité dans les couches supérieures et inversement, une augmentation de la salinité en profondeur, qui mènent à une augmentation de la stratification. En ce qui concerne les nutriments azotés, les changements futurs sont variables et généralement non significatifs si on considère l'ensemble des simulations. La biomasse de chlorophylle *a* diminue dans le GSL et sur la partie est du Plateau Néo-Écossais mais augmente dans les autres régions. Les simulations montrent une acidification sur tout le domaine du modèle avec une diminution du pH et des saturations en carbonates à toutes les profondeurs. D'ici 2090, les niveaux de saturation en aragonite auront atteint la valeur critique de 1 sur presque tout le fond du domaine du modèle, ainsi qu'à la surface dans le GSL et sur le plateau Néo-Écossais. Les saturations en calcite quant à elles atteignent cette valeur critique sur le plateau Madelinien et dans la partie est du Plateau Néo-Écossais.

LIST OF ACRONYMS

AC	Anticosti Channel
CanESM2	second generation Earth System Model of the Canadian Centre for Climate Modelling and Analysis
CS	Cabot Strait
CGSL	Central Gulf of St. Lawrence
CMIP5	Coupled Model Intercomparison Project Phase 5
CRCM	Canadian Regional Climate Model
CSI	Cumulative Stressor Index
DIC	Dissolved Inorganic Carbon
DON	Dissolved Organic Nitrogen
ESM	Earth System Model
ESS	Eastern Scotian Shelf
GoM	Gulf of Maine
GSL	Gulf of St. Lawrence
HadGEM2-ES	Global Environmental Model, version 2, with an Earth System component, of the Met Office Hadley Centre
LP	Large Phytoplankton
LSLE	Lower St. Lawrence Estuary
MEZ	Mesozooplankton
MIZ	Microzooplankton
MS	Magdalen Shallows
NWGS	Northwestern Gulf of St. Lawrence
PON	Detrital Particulate Organic Matter
MPI-ESM-LR	Low Resolution Earth System Model of the Max Planck Institute for Meteorology
NH ₄	Ammonium
NO ₃	Nitrate
SP	Small Phytoplankton
SS	Scotian Shelf
TA	Total Alkalinity
WSS	Western Scotian Shelf

1 INTRODUCTION

The Earth's climate is changing. The oceans are affected in many ways with important warming of surface waters (Rhein et al., 2013), deoxygenation (Schmidtko et al., 2017), acidification (Doney et al., 2009), reduced nutrient supply to the surface layer and potential reduction in primary production (e.g., Boyce et al., 2010). These changes are impacting the well-being and the distribution of many fish species (Cheung et al., 2013; MacKenzie et al., 2014), and lead to altered food web dynamics (Doney et al., 2012). Such changes have also been observed in the northwest Atlantic. Decreasing dissolved oxygen trends have been observed in the slope-derived deep waters in the Gulf of St. Lawrence (GSL) and on the Scotian Shelf (Claret et al., 2018; Gilbert et al., 2005; Petrie and Yeats, 2000; Yeats et al., 2010). There has also been an increase in the concentration of dissolved inorganic carbon and a concurrent decrease of 0.2 to 0.3 pH units at depth in the St. Lawrence Estuary since the 1930s (Mucci et al., 2011). This decrease is four to six times faster than the decrease in pH at the surface in the open ocean. A decrease in pH has also been observed on the Scotian Shelf (Curran and Azetsu-Scott, 2012). These changes modify the essential or preferred habitat of pelagic and benthic species in these regions (Bianucci et al., 2016; Brennan et al., 2016; Stortini et al., 2017) and detailed projections are thus required to manage the different stocks.

Earth System Models (ESM) are an essential tool to predict future climate changes, but they suffer from a coarse resolution and are ineffective at representing the complex dynamics of the northwest Atlantic (Lavoie et al., 2013; 2019; Loder et al., 2015). Thus, to anticipate and adapt to changes occurring in our regions, the development of a coupled regional climate model was initiated a few years ago for the Gulf of St. Lawrence, Scotian Shelf and Gulf of Maine. The method for the downscaling of atmospheric conditions and projections of oceanographic conditions is described in Guo et al. (2013), Perrie et al. (2015), and Long et al. (2016). A careful analysis of the projections from the different ESMs was also done near the boundaries of the regional climate model to assess their robustness and applicability to force the regional climate model (Lavoie et al., 2019).

In this report, we present the results from three simulations performed with the regional climate model forced with downscaled conditions from CanESM2, MPI-ESM-LR, and HadGEM2-ES using the Representative Concentration Pathway (RCP) 8.5 climate scenario (Moss et al., 2010). The model output for these three ESMs was made available in 2013 for the fifth assessment report (AR5) of the Intergovernmental Panel on Climate Change (IPCC) through the Coupled Model Intercomparison Project Phase 5 (CMIP5) archive. The regional model simulations are analyzed to estimate future changes in environmental conditions and the extent of ocean acidification in the GSL, Scotian Shelf, and Gulf of Maine (GoM). Maps of changes for the different variables are included to help managers in decision making, by providing information such as years when calcium carbonate saturation states (Omega values for calcite and aragonite) will reach critical values. Omega values smaller than 1 correspond to undersaturated water in which calcium carbonate starts to dissolve, affecting the organisms that build carbonate shells or skeletons. However, in fact, dissolution can occur at higher Omega values that are species dependent (e.g., Bednarsek et al., 2020). Here we present information for Omega values of 1.0 and 1.5. Cumulative changes can also be particularly challenging to adapt to for many marine species and we present a map of areas where large changes in the physical and biogeochemical variables co-occur. Analysis of the significance of the changes, of the agreement between models on the sign of the change, as well as the spread of values of the model ensemble will allow us to evaluate the likelihood of the projected trends.

2 MATERIAL AND METHODS

2.1 OCEAN MODEL

The ocean circulation model used in this study is based on the code from NEMO (Nucleus for European Modelling of the Ocean) modelling framework. The physical module of NEMO, OPA (Océan PARallélisé) version 3.2, was first implemented by Brickman and Drozdowski (2012) in the GSL, the Scotian Shelf, and the GoM (Figure 1). The resulting regional ocean circulation model, nicknamed CANOPA, has a horizontal resolution of $1/12^\circ$ (~6.5 km). The model has 46 vertical layers with a thickness from 6 m at the surface to 250 m at 5000 meters. Monthly temperature and salinity are implemented at the ocean borders

for the entire water column. CANOPA uses the runoff of 78 rivers to account for the monthly freshwater input into the domain (see section 2.4).

2.2 BIOGEOCHEMICAL MODEL

A detailed validation and description of the biogeochemical model (GSBM, Figure 2) is given in Lavoie et al. (2020). It includes an NPZD (Nutrient-Phytoplankton-Zooplankton-Detritus) module, composed of eight tracers: nitrate (NO_3), ammonium (NH_4), large phytoplankton (LP), small phytoplankton (SP), mesozooplankton (MEZ), microzooplankton (MIZ), detrital particulate organic nitrogen (PON), and dissolved organic nitrogen (DON). The biogeochemical model also includes a dissolved oxygen module (one tracer), and an inorganic carbon module. The latter includes 2 tracers, dissolved inorganic carbon (DIC) and total alkalinity (TA), from which pH, partial pressure of carbon dioxide (pCO_2), carbon dioxide (CO_2), bicarbonate (HCO_3^-), carbonate (CO_3^{2-}) and calcium carbonate (CaCO_3) saturation states can be derived (Dickson et al., 2007).

2.3 ATMOSPHERIC CONDITIONS

Atmospheric forcing for the regional model is obtained from the dynamical downscaling of the ESMs atmospheric conditions using the Canadian Regional Climate Model (CRCM, Guo et al., 2013; Long et al., 2016). The domain of CRCM covers the east coast of North America and part of the Northwest Atlantic Ocean. Daily forcing of air temperature, wind speed, specific humidity, precipitation, downward longwave radiation and downward shortwave radiation are available for the 1970 to 2100 period. A diurnal cycle was added to the daily shortwave radiation to improve the representation of phytoplankton growth. Air-sea CO_2 fluxes are calculated using the atmospheric CO_2 concentrations prescribed in the RCP 8.5 scenario (Figure 3).

2.4 RIVERS

The monthly average runoff of the 78 rivers included in the model (Figure 4) was obtained with a simple hydrological model (Lambert et al., 2013) that uses precipitation and air temperature outputs from the CRCM downscaling of the ESMs atmospheric conditions to

determine the form of precipitation (solid or liquid) and evaporation. River salinity is always zero (freshwater) and its temperature depends on seawater temperature near the river mouth. Monthly climatologies of the riverine chemical components from Lavoie et al. (2020) are used over the whole period of the simulations (1970 to 2100). Changes in the riverine flux of the different chemical constituents are thus solely caused by the changes in freshwater runoff (Figure 4).

2.5 OCEANIC BOUNDARY CONDITIONS

The results from the three ESMs were used to calculate monthly boundary conditions of physical and biochemical variables (temperature, salinity, nitrate, oxygen, DIC, and TA) for all the years from 1970 to 2100. We used the years 1991 to 2010 as the reference period to calculate monthly anomalies for the ESMs over the 1970 to 2100 period. Those anomalies were then added to the observed 1981 to 2010 climatology used in Lavoie et al. (2020) to get the boundary conditions from 1970 to 2100 for the three ESMs with common average conditions over the reference period.

Monthly means of nitrate, dissolved oxygen, DIC, and TA from the ESMs in the CMIP5 archive were only available for the surface layer as 2D fields, while only annual means were available for the 3D fields (for each cell of the ESMs). Monthly anomalies required to build the boundary conditions for the biogeochemical variables could thus not be calculated directly. For waters below the mixed layer (calculated by the ESMs), which we assume exhibit low seasonal variability, we calculated the annual anomaly (each year between 1970 and 2100 compared to the 1991-2010 average), which was applied to each month of that particular year. For waters in the upper mixed layer, which follow a seasonal cycle, we first calculated a mean normalized seasonal cycle, using the 2D field from the ESMs. This normalized seasonal cycle was then adjusted to the annual anomaly calculated from the 3D field to obtain the monthly anomalies of a particular year (i.e., the anomaly differs from one month to the next but the annual mean is the same, see Figure 5).

With these two different steps, for the mixed layer and below, we were able to calculate the monthly anomaly for nitrate, dissolved oxygen, DIC, and TA for all years from 1970 to

2100 and for the entire water column. Monthly means of temperature, salinity and current velocities from the ESMs were available for the whole water column and thus the monthly anomalies could be calculated directly.

Figures 6 to 19 show the climatology of the physical and chemical variables and their trends at the open boundaries calculated with three ESMs. Three zones, some corresponding to those analyzed in Lavoie et al. (2019), are highlighted at the boundaries (BI, SB, and GS in Figure 1).

2.6 EXPERIMENTAL DESIGN

The experimental design used in this study was developed by Long et al. (2016) to simulate the evolution of the ocean conditions (see above sections). Three simulations were run separately with the forcing that was derived from the three ESMs for the atmospheric, riverine, and oceanic conditions under the RCP 8.5 scenario. However, as the dissolved oxygen was not simulated by CanESM2, we could not derive future boundary conditions using the output of this model. We thus used the average dissolved oxygen trends from the 7 ESMs that were available at the time this study was initiated (see Lavoie et al., 2019).

Our simulations start in January 1970 using climatological values of temperature, salinity, nitrate, oxygen, DIC, and alkalinity as initial conditions. The other biochemical tracers (LP, SP, MEZ, MIZ, PON, and DON) were initially given an arbitrary value. The simulations ran from year 1970 up to 2100 using daily atmospheric forcing with 25 outputs per year, representing the average conditions every 14.6 days.

3 RESULTS

3.1 HISTORICAL PERIOD

A qualitative comparison of the ESMs output (bi-weekly average) was performed with observations as well as with the output of Lavoie et al. (2020). A validation of hindcast simulations produced by the regional model is made for the physics in Lavoie et al. (2016) and for the biogeochemistry in Lavoie et al. (2020). The simulations obtained here use forcings derived from ESMs that are not meant to accurately represent regional conditions

but rather global scale patterns and trends, and the output is at a much lower frequency (about two weeks compared to one or two days for the hindcast simulations). Nevertheless, we present some comparisons with observations over the historical period (two week averages with in situ data collected during that two week period time frame) in the form of Taylor and Target diagrams (Jolliff et al., 2009) to have a general idea of the model output representativeness (Figures 20, 21, and 22). A linear interpolation is made to obtain a point to point comparison in time with the observations. In the Target diagram, the variables found inside the circle with a radius of one have a centered root mean squared difference (RMSD) that is lower than one standard deviation and are thus more reliable than those found outside the circle. The historical conditions in the GSL compare well to what is expected (Figure 20). In the Scotian Shelf and GoM (Figures 21 and 22), an offset is present for pH and calcium carbonate saturation values (a little higher than expected in some areas). However, it should be reminded that there are few data available for these variables, and a seasonal bias is sometimes present.

In this report, we focus on the changes between present times and the future period. The changes in atmospheric forcing, as well as in river runoff and boundary conditions, are driving these changes and those were constrained as best as we could. The analysis of Lavoie et al. (2019) also shows that the projections obtained on the Scotian Shelf and GoM have a greater uncertainty than those obtained in the GSL due to differences in projections robustness obtained from the ESMs along the open boundaries.

At the time of writing this report, we found an error in the equation computing the oxygen utilization during nitrification of ammonium. We present the boundary conditions for dissolved oxygen computed from the ESMs but we decided not to present the projections for dissolved oxygen obtained with the regional model at this time. The other results are not affected by this error. The results for oxygen will be presented in a different document following computation of the new simulations.

3.2 PROJECTIONS

To evaluate future changes, we compare two bi-decadal means, 1991-2010 and 2061-2080, representing the change over 70 years. We present these results for four layers: 0-50 m, 50-150 m, 150-300 m, and the bottom layer (last grid cell at every point). These layers were chosen as they characterize the water masses throughout most of the GSL (Mucci et al., 2011). In the GoM and Scotian Shelf, the depth of the intermediate layer, corresponding approximately to the winter mixing depth, is a little shallower (about 100 m), so that the 50-150 m layer extends slightly in the deeper water mass (Smith et al., 1978; Townsend et al., 2015). The results produced by the regional model using the three downscaled forcings, i.e. CanESM2, MPI-ESM-LR, and HadGEM2-ES, over the historical period are very similar, so we present these results as an ensemble mean. The future changes predicted by each simulation are displayed as the difference between two bi-decades (2061-2080 minus 1991-2010). The bi-decadal change is considered significant when it is higher than three times the standard deviation calculated over the historical period. We also present the inter-model change spread, calculated as the difference between the maximum and the minimum 2061-2080 average obtained at every grid cell with the three simulations. The annual cycle of some variables over the regions presented in Figure 23 for the 0-50 m and 50-150 m layers, which are the depths most affected by local atmospheric forcing, is also presented. The variables for which the change is relatively uniform over the year are not shown (temperature, DIC, TA, pH and calcium carbonate saturation states).

3.2.1 Sea-ice thickness and concentration

Sea-ice thickness and concentration are both expected to decrease in the future (Figure 24 and 25). The mean sea-ice thickness is greatly reduced in the 2061-2080 period (Figure 24B). There is markedly more sea ice in the simulation forced with MPI-ESM-LR than with the two other simulations. In the simulations forced with HadGEM2-ES and CanESM2, there is hardly any sea ice present except in February. There is no sea ice in April in all simulations. These changes are significant around the Magdalen Islands and along the north shore of the GSL, and in the Lower St. Lawrence Estuary (LSLE), northwest GSL (NWGSL), and western part of the southern GSL in January and February with HadGEM2-

ES and CanESM2. The changes in mean sea-ice fraction follow a similar pattern (Figure 25), even though the significance of the changes is reduced (only the changes in the southern GSL in February are significant with all three simulations). The inter-model change spread is quite large for both variables.

3.2.2 Temperature

Future projections show a general warming over the whole domain and in all four layers presented for all three simulations (Figure 26B). These changes are mostly significant, except on the western and central Scotian Shelf with MPI-ESM-LR. The smallest change is obtained with the simulation forced with MPI-ESM-LR (up to about 2°C in the surface layer), while the simulation forced with HadGEM2-ES presents the most important warming (up to 4°C in the surface layer in the GSL, and up to 5°C in the deep layer in the Laurentian Channel). The inter-model change spread (Figure 26C) is ~ 2°C in the surface layer. It reaches up to 4°C in the northeast GSL at 50-150 m, and is as low as 1°C at depth in the Laurentian Channel. The increase in temperature is relatively constant over the annual cycle in the surface layer except in February and March in regions where a sea-ice cover is present in winter (Figures 24 and 25). During these months, the difference between future and historical periods is reduced by half compared to the rest of the year. Figure 27 shows the temperature trend averaged over different depths (0-50 m, 50-150-m, and 150-300 m) in the GSL region (see Figure 23). The trends for the Scotian Shelf and GoM are also presented in Table 1. The three simulations show an increasing trend of annual mean temperature. The simulation forced with MPI-ESM-LR generally shows weaker trends. Simulations forced with HadGEM2-ES and CanESM2 present trends that are very similar in the GSL but not so in the two other regions.

3.2.3 Salinity

Future projections show freshening in the two upper layers (0-50 m and 50-150 m), while salinity below 150 m increases (Figures 28B and 29, and Table 2). However, these changes are not significant everywhere or with the three forcings. Significant changes are simulated with the three simulations in the upper layer of the GSL, at intermediate depths along the north shore of the GSL and on the Magdalen Shallows, as well as at depth in the Laurentian

Channel. The freshening obtained with the simulation forced by HadGEM2-ES (decrease in salinity of 2 psu) is greater than with the two remaining simulations (decrease in salinity of 1 psu). The inter-model change spread (Figure 28C) shows high values in the surface layer (around 1.5 psu) and low values in the deepest layer (around 0.2). In most regions, the change in salinity is greater in spring and summer (Figures 30 and 31).

3.2.4 Stratification

The stratification was calculated as the sea water density difference between the first layer of the model, centered at 3.05 m, and the density in the 7th vertical layer, centered at 51.95 m. We assume that this value is representative of the difference over the upper 50 m. The results are shown in Figures 32 and 33. There is a high horizontal variability in the GSL, with a weaker stratification in the northeast GSL and stronger stratification in the LSLE and near the coast of the Gaspé Peninsula, where freshwater outflow is more important. Conditions on the Scotian Shelf and in the GoM are mostly homogeneous with a small increasing gradient from west to east. Future conditions (Figure 32B) show an increase in stratification over the entire model domain. This is consistent with the projected warming and freshening, which is more important in the upper layer than below. These changes are not significant everywhere and with all simulations but they are more consistent in the central Scotian Shelf and part of the GoM. The increase in stratification is generally higher (almost double) in the simulation forced with HadGEM2-ES compared to the other two simulations. The time series of the annual mean stratification in the GSL (Figure 33) show that this difference results from a particularly strong increase between 2070 and 2080. The inter-model change spread (Figure 32C) is greater in the LSLE and NWGSL compared to other regions.

Figure 34 shows the mean annual cycles for the historical and future periods. Stratification is stronger in summer and in regions under the influence of the St. Lawrence river runoff (LSLE, NWGSL, MS, and CGSL). Future conditions show a large increase in stratification in summer and a small or inexistent increase during winter.

3.2.5 Nitrate concentration

Future mean annual nitrate concentrations decrease in the upper layer (0-50 m) in all three simulations, except in Chaleur Bay, the Magdalen Shallows, and the GoM, where the direction of change is more variable (Figures 35B and 36). The simulation forced with HadGEM2-ES shows an increase in the GoM (up to $0.9 \text{ mmol N m}^{-3}$ in the surface layer), while the simulation forced with CanESM2 shows the strongest decrease in the LSLE (-2 mmol N m^{-3}). In some regions, the decrease is more important at the end of winter (March, regions within the GSL and ESS, Figure 37), while an increase is observed either in the summer (MS and WSS) or at the end of fall (LSLE and NWGSL with HadGEM2-ES). These changes result in a dampening of the surface nitrate concentration annual cycle compared to historical values. In the intermediate layer (50-150 m), the trends vary from one simulation to the other (Figures 35B and 36). Consistent with this high variability, the inter-model change spread is greater in that layer (Figure 35C, up to 4 mmol N m^{-3} in the LSLE, northeast GSL and GoM). In the deeper layer (150-300 m), all three simulations show an increase in nitrate concentration in the northeast GSL, and a decrease in the Laurentian Channel, east of Cabot Strait, consistent with the trends at the model open boundaries (Figures 12 and 13, section 4.2). This decrease is more important when forced with CanESM2 ($\sim -4.5 \text{ mmol N m}^{-3}$). In other areas, the sign of change varies. It is to note, however, that only the decrease simulated in the deeper reaches on the Laurentian Channel is significant with all three simulations (Figure 35B, bottom panels).

3.2.6 Ammonium concentration

Annual mean ammonium concentrations display a decrease in the future in the first two layers in all regions except in the GoM, where there is either no change or a small increase (Figures 38B and 39). In the deeper layer, changes are small (Figures 38B and 39), except in the GoM where a small increase is simulated. The most noticeable change occurs on the Magdalen Shallows (up to -0.4 and $-1.0 \text{ mmol N m}^{-3}$ in the surface and intermediate layers, respectively), the region that displays the highest ammonium concentration (Figure 38A). When considering the three simulations, the reported changes are not significant. However, two of the simulations show a significant increase in parts of the GoM (Figure 38B).

The changes vary over the seasonal cycle, with an increase in spring compared to the historical period, and a decrease afterward, especially in summer in the NWGSL, MS, CGSL, and AC regions (Figure 40). Elsewhere, the changes over the seasonal cycle are more uniform.

3.2.7 Diatoms

Diatoms are represented by the large phytoplankton (LP) box in Figure 2. Future projections show an increase in surface layer diatom-N concentration in the GoM, on the Scotian Shelf and in the northeast GSL, and a decrease in the NWGSL and on the Magdalen Shallows (Figure 41B). However, the changes are significant only on the Scotian Shelf and in part of the GoM. The inter-model change spread tends to be higher in regions of high diatom concentration (NWGSL, LSLE, and GoM, Figure 41C).

The time series of diatom-N concentration in the GSL does not show a consistent trend in the surface layer when considering the 1980 to 2100 period (Figure 42), although it does when looking at the bi-decades in Figure 41B. The diatom spring bloom in the GSL occurs earlier in the projections, although its amplitude is lower compared to historical values.

3.2.8 Flagellates

Flagellates are represented by the small phytoplankton (SP) box in Figure 2. Contrary to diatoms, future projections show a decrease in flagellate-N concentration over the whole model domain (43B and 44). These changes are significant with the three simulations on the Scotian Shelf. The simulation forced with HadGEM2-ES shows the highest decrease in that region ($\sim -0.05 \text{ mmol N m}^{-3}$ in the surface layer). The inter-model change spread is also highest on the Scotian Shelf and in the northeast GSL (Figure 43C). As for the pool of diatom-N, projections suggest an earlier flagellate spring bloom in certain regions (NWGSL, MS, not shown).

3.2.9 Chlorophyll *a* concentration

Chlorophyll *a* (chl *a*) biomass is displayed as the sum of the diatoms and flagellates, converted from mmol N m^{-3} to $\text{mg chl } a \text{ m}^{-3}$ using a factor of 1.5, and integrated vertically over the top 50 meters (Figure 45A). Future projections of chl *a* biomass (Figure 45B) follow the same pattern as for diatom-N pools with a significant increase only in parts of the GoM. The inter-model change spread is greater for the projections in the Lower Estuary, the NWGSL, and the northeast GSL (Figure 45C).

The annual cycle of chl *a* biomass (Figure 46. Mean chlorophyll *a* biomass annual cycle inside the zones defined in Figure 23 at the 0-50 m depth interval, for the simulations forced with MPI-ESM-LR, HadGEM2-ES, and CanESM2 under the RCP 8.5 scenario. The annual cycle is defined as the average of each step (25 per year) for the 20 years of the historical (solid lines) and the future periods (dashed lines). Figure 46) shows that in many regions (NWGSL, MS, CGSL, AC), the bloom occurs somewhat earlier (3 to 4 days) for the projected 2061-2080 period compared to the historical mean while its amplitude is smaller (slight decrease of -0.13 to -0.16 $\text{mg chl } a \text{ m}^{-3}$ for the surface layer and -2.0 to -3.2 $\text{mg chl } a \text{ m}^{-2}$ for the vertically integrated biomass). On the Scotian Shelf, the timing of the bloom is about the same (Figure 46).

3.2.10 Diatom to flagellate ratio

The diatom to flagellate ratio ($\text{mol N}:\text{mol N}$) is greater in the LSLE, the NWGSL, the Magdalen Shallows, and the GoM (Figure 47A). Future projections suggest an increase in the diatom-N to flagellate-N pool ratio over the whole domain except in the NWGSL (small decrease), on the Magdalen Shallows and in the upper reaches of the northeast GSL (Figure 47B). However, changes are only significant in parts of the northeast GSL, on the Scotian Shelf, and in parts of the GoM. These areas also display high inter-model change spread in the results (Figure 47C).

All three simulations show an increasing temporal trend of the diatom-N to flagellate-N ratio in the GSL starting around 2040 (Figure 48). Over the seasonal cycle, future

projections show that the diatom to flagellate ratio (mol N:mol N) generally increases in the fall, except in the LSLE, where we observe an increase of the summer values (Figure 49).

3.2.11 Mesozooplankton

Zooplankton diel and seasonal vertical distributions are not represented in the model, and thus, zooplankton growth tracks phytoplankton growth and distribution near the surface. We thus present the results for the 0-50 m layer as for phytoplankton (Figures 50 and 51). Future projections (Figures 50B and 51) show a decrease in mesozooplankton-N concentration throughout the domain. The simulation forced with HadGEM2-ES shows the greatest decrease with significant changes over a large part of the domain. However, only the Scotian Shelf region presents a significant decrease with all three simulations. This decline most likely results from the temperature increase (Figure 26) that leads to a greater mortality rate. Following diatoms, mesozooplankton growth occurs earlier in spring in the future and there is a decrease in the maximum concentration attained in almost all regions (Figure 52). This trend is less pronounced in the GoM and on the Scotian Shelf.

3.2.12 Microzooplankton

As for mesozooplankton, the future projections of microzooplankton show a general decrease over the whole domain, except for an open boundary artefact at the entrance of the Laurentian Channel (Figures 53B and 54). Also similar to mesozooplankton, the decrease is more important when the simulation is forced with HadGEM2-ES, and the changes are significant with the three simulations over the Scotian Shelf only. The inter-model change spread is higher on the Scotian Shelf and in the northeast GSL (Figure 53C).

Following flagellates (not shown), the microzooplankton peak simulated during spring in many regions of the GSL is flattened in future projections (i.e. decrease in the maximum concentration attained, Figure 55). An exception is seen in the LSLE region, where the future microzooplankton concentration remains more or less the same.

3.2.13 Detrital particulate organic nitrogen

As shown in Figure 2, PON consists mostly of dead mesozooplankton and dead diatoms. Future projections show an increase in detrital PON in the GoM and a decrease on the Magdalen Shallows with all three simulations (Figure 56B). In the other regions, the results are more variable and the sign of the trend depends on the simulation, although on average the trend is negative in the GSL (Figure 57). These changes are significant only in parts of the GoM. Changes in the annual cycle are similar in the 0-50 m and the 50-150 m layers. For regions that undergo a decrease in detrital PON (NWGSL, MS, CGSL, and AC), it occurs mainly due to the reduction in the amplitude of the spring maximum (or summer maximum in the LSLE, Figure 58).

3.2.14 Dissolved organic nitrogen

Dissolved organic matter is supplied by rivers, and produced through microzooplankton and small phytoplankton mortality, and through the fragmentation of detrital PON. A fraction (50%) of the detrital PON and diatoms that gets deposited in the sediment is also redistributed instantaneously in the bottom layer as DON, generating relatively high values near the bottom in shallow productive regions (Figure 59A). Future changes in DON follow the same pattern as that of detrital PON (section above). The projections show an increase in the GoM and a decrease on the Magdalen Shallows with all three simulations (Figure 59B). In the other regions, the results are more variable and the sign of the trend depends on the simulation, although on average the trend is negative in the GSL (Figure 60). These changes are significant only in parts of the GoM when considering the three simulations. The inter-model change spread (Figure 59C) is greater in the shallower areas of the southern GSL and Scotian Shelf. As for PON, the DON annual cycle shows a decline mainly in spring in the GSL regions, as well as a slight increase in the GoM (Figure 61).

3.2.15 Dissolved inorganic carbon

Lower values of DIC are found in the surface layer and near freshwater sources, while higher values are found in the deeper layers (Figure 62A). Future changes (Figures 62B and

63, and Table 3) are positive almost everywhere for all simulations, except with the simulation forced with HadGEM2-ES, where a decrease is observed in the upper layer in the GSL and in the central and eastern Scotian Shelf. This difference is related in part to the declining DIC concentration at the Strait of Belle Isle with this forcing (Figures 16 and 17). In the upper layer, the changes are significant in the GoM only (Figure 62B). Below 50 m, the changes are significant everywhere and with the three simulations except on the Magdalen Shallows. In the GSL, the rate of increase is highest in the deep layer (about $12 \text{ mmol m}^{-3} \text{ dec}^{-1}$), and the agreement between simulations is very high in this layer. The most pronounced increase is observed in the GoM in all layers (Figure 62B, Table 3). In certain regions, in particular in the NWGSL and MS, the increase is more important during spring in the surface layer, except under HadGEM2-ES forcing where we observe a decrease instead (not shown). On the western Scotian Shelf, we find a smaller change in spring.

In the surface layer, the inter-model change spread (Figure 62C) is similar among regions, although slightly lower in the GoM. In the intermediate layer, it is slightly higher on the Magdalen Shallows.

3.2.16 Alkalinity

Alkalinity follows the horizontal distribution of salinity (Figure 28A) with lower values in the LSLE and Magdalen Shallows, and higher values in the GoM (Figure 64A). Future projections also follow the salinity trends (Figure 28B) with a decrease in the surface and intermediate layers (except in the GoM under MPI-ESM-LR and CanESM2 forcing), and an increase in the deeper layers (Figures 64B and 65, and Table 4). The simulation forced with HadGEM2-ES presents the greatest changes. The changes are mostly significant but somewhat less on the Scotian Shelf and in the GoM. The inter-model change spread is similar to DIC with higher values in the surface layer, but somewhat lower in the GoM, and lower values in the deep channels of the GSL (Figure 64C). In the intermediate layer, a greater inter-model change spread is simulated on the Magdalen Shallows.

3.2.17 pH

pH can be measured on different scales (seawater scale, total scale, free scale). Here we use the carbonic acid dissociation constants of Lueker et al. (2000) and the total scale (Dickson et al., 2007) to calculate pH. We thereafter use the term pH_{total} instead of pH to highlight the calculation method. Future projections (Figures 66B and 67, and Table 5) suggest a widespread decline in pH_{total} in all layers and simulations, as well as over the seasonal cycle (not shown). Trends over the 1980 to 2099 period vary between -0.031 and -0.047 units per decade depending on the region and depth (Table 5). The decrease is generally higher in the intermediate layer (50-150 m) and smaller in the deep layer (150-300 m), except in the GoM where trends in the 150-300 m layer are either similar or higher than those of the surface layer. As for DIC, the pH_{total} changes are significant everywhere and with all three simulations (Figure 66B). In the intermediate layer, the inter-model change spread (Figure 66C) is greater in the GoM, on the Scotian Shelf, and on the Magdalen Shallows. In the deep layer, the spread is more important near the GSL channel heads (Laurentian, Anticosti, and Esquiman channels).

3.2.18 Aragonite and calcite saturation states

The historical ensemble mean for aragonite and calcite saturation states vary regionally following freshwater distribution in the upper layer (smaller values in fresher water). In the deeper layers, smaller values are found in regions of high organic matter recycling (Figures 68A and 70A, respectively). Future changes show a general decrease in aragonite and calcite saturation throughout the domain (Figures 68B, 69, 70B and 71, and Table 6). The decreasing trend is higher in the upper layer (varying between -0.073 and -0.097 per decade for aragonite and between -0.117 and -0.154 per decade for calcite) and gets smaller with depth (between -0.030 and -0.076 per decade in the 150-300 m layer for aragonite and between -0.049 and -0.122 per decade for calcite). The trends are smaller in the GSL, where saturation values are already low, and more pronounced on the central and western Scotian Shelf and in the GoM. As for pH_{total} , these changes are significant over the whole domain, for all depths and with the three simulations. The surface layer inter-model change spread (Figures 68C and 70C) is lowest in the GoM and highest in the LSLE, NWGSL, and

Mecatina Trough. In the intermediate layer, the inter-model change spread is higher on the Magdalen Shallows, the Scotian Shelf, and in the Mecatina Trough.

3.2.19 Time to reach critical aragonite and calcite saturation thresholds

A saturation state of 1.0 is the level below which carbonated structures are considered to start dissolving. However, a number of studies on different taxa (e.g. see Table 1 in Gledhill et al., 2015) show that an Omega value of 1.5 in larvae of many bivalve species (Baumann et al., 2012; Talmage and Gobler, 2009; 2010), as well as higher values for some crustaceans and adult corals, can be detrimental. Aragonite is more soluble than calcite at a given temperature, salinity and pressure (Zeebe and Wolf-Gladrow, 2001), and thus it becomes under-saturated sooner than calcite. Here we present results for the 1.0 and 1.5 thresholds. Figures 72 and 73 illustrate the year in which annual means of calcite and aragonite saturation states reach the thresholds of 1.0 (upper panels) and 1.5 (lower panels) at the ocean's surface (0-6 m layer) and on the bottom.

At the surface, aragonite undersaturation is already present in the Upper St. Lawrence Estuary and part of the LSLE (Figure 72A). About half of the GSL's surface layer becomes undersaturated with respect to aragonite by 2060, and the entire GSL is undersaturated by 2090 or a little earlier depending on the simulation (Figure 72A). The Scotian Shelf reaches the 1.0 threshold between 2070 and 2090, with variable spatial extent depending on the simulation. Surface aragonite undersaturation is not reached in the GoM by the end of the simulation except for a very small area with the HadGEM2-ES forcing. Calcite does not reach undersaturation in the surface layer except in the upper estuary (Figure 73A).

On the bottom, aragonite is already undersaturated over a large portion of the GSL (LSLE, NWGSL, Magdalen Shallows, head of the deep channels in the eastern part), as well as part of the eastern Scotian Shelf (Figure 73A). Aragonite undersaturation spreads over most of the Scotian Shelf by 2060, and even before that with HadGEM2-ES. In the deeper part of the GoM, aragonite undersaturation is reached around 2050 and extends to most of the GoM between 2080 and 2090. The eastern part of the deep Laurentian Channel also reaches

aragonite undersaturation between 2050 and 2080, except with CanESM2, with which the annual mean aragonite saturation values remain above 1.0.

The time when calcite saturation reaches the 1.5 threshold (Figure 73B) mostly follows a pattern similar to the aragonite saturation for the 1.0 threshold (Figure 72A). The 1.0 threshold for calcite is already reached on the Magdalen Shallows with the simulations forced with MPI-ESM-LR and CanESM2 (Figure 73A). It then spreads to the shallower areas of the GSL (mostly covered by 2080) and to the LSLE portion of the deep Laurentian Channel by 2060 (MPI-ESM-LR), 2080 (HadGEM2-ES), or not at all (CanESM2). By 2090 it covers a large part of the Scotian Shelf but the 1.0 threshold is never reached in the GoM for calcite, except for a very small area when forced with CanESM2.

3.2.20 Cumulative stressors index

The Cumulative Stressor Index (CSI) was built to assess the number of significant changes experienced by the ecosystems at each grid point (Figure 74). We built a matrix for each of the 12 selected variables (temperature, salinity, nitrate, ammonium, diatoms, flagellates, mesozooplankton, microzooplankton, detrital particulate organic nitrogen, dissolved organic nitrogen, pH_{total} , and aragonite saturation) to which we attributed a value of one if the change between the two bi-decades (1991-2010 and 2061-2080) was larger than three times the historical standard deviation, and zero otherwise (i.e. if the change is smaller than three standard deviations). This calculation was repeated at each grid point. We then summed up the twelve matrices to obtain the number of variables for which a significant change was simulated at each grid point. Since certain variables are interrelated (such as DIC, TA, pH, aragonite and calcite saturation) we did not use all the variables in an attempt to not over-represent a certain group of variables. Figure 74 shows the CSI in all four layers (surface, intermediate, deep, bottom) for all three simulations (forced with MPI-ESM-LR, HadGEM2-ES, and CanESM2). However, it should be noted that the planktonic variables contribute more strongly to the upper layer, leading to higher CSI values in that layer. The CSI has a value of two or higher throughout most of the domain. In all layers, the simulation forced with HadGEM2-ES shows a higher CSI than the other simulations on the Scotian Shelf, in the Laurentian Channel and in the northeast part of the GSL. All three simulations

present a higher CSI in the coastal regions of the GoM, the Bay of Fundy and the deeper part of the Laurentian Channel, suggesting that species in these regions will be subject to a larger number of stressors. When looking at the model ensemble average (Figure 74, last column), we see that the cumulative changes are more important in the eastern GSL and on the Scotian Shelf in the upper layer, while, on the bottom, they are more important in the deep Laurentian Channel and in parts of the GoM.

4 SUMMARY AND DISCUSSION

4.1 PHYSICAL ENVIRONMENT

Future projections show a generalized significant warming over the whole domain (between 2 and 5°C depending on the region and depth, Figure 26), a freshening of the upper layers, accompanied with an increase in salinity below 150 m (except in the GoM where increased salinity is simulated at shallower depths). The changes in salinity are significant for the most part in the GSL but not on the Scotian Shelf or GoM (Figure 28). These trends in temperature and salinity lead to an increase in stratification (Figure 32), especially in summer (Figure 34), and a reduction in sea ice cover in the GSL (Figures 24 and 25). The changes in stratification, contrary to salinity, are significant on the Scotian Shelf and GoM, indicating the greater role of the temperature increase on stratification changes in these areas. The simulation forced with HadGEM2-ES generally displays the most pronounced changes (either an increase or a decrease), while the simulation forced with MPI-ESM-LR often leads to the least pronounced changes. The warming and increase in salinity in the deeper layer most likely results from a gradual increase in the proportion of Gulf Stream water entering the deep channels in the GSL, Scotian Shelf, and GoM (Claret et al., 2018; Lavoie et al., 2019).

4.2 BIOLOGICAL VARIABLES

Projected future changes in nutrients are variable and generally not significant when considering the three simulations together (i.e. a change at a certain location can be significant with one or two simulations only), except for the decline in nitrate on the bottom of the deep Laurentian Channel (Figure 35), that results from a decrease in nitrate

concentration in the upper 900 m or so at the open boundaries of the model (Figures 12 and 13). All three simulations show an increase in ammonium concentration in the GoM that is significant when forced with HadGEM2-ES and CanESM2 but not with MPI-ESM-LR (Figure 38).

The chl *a* biomass increases in the LSLE, on the Scotian Shelf, and in the GoM, and decreases in the NWGSL and on the Magdalen Shallows (Figure 45). Flagellates are decreasing over the whole domain (Figure 43), indicating that the increase in chl *a* results from an increase in diatom biomass (Figure 41). The diatom to flagellate ratio increases almost everywhere (Figure 47). The increase in the ratio is particularly important in the fall (Figure 49) due to both an increase in diatom biomass and a decrease in flagellate biomass. The increase in diatom biomass most likely results from the temperature increase that leads to a greater mesozooplankton mortality in our NPZD model (which is a function of temperature, Lavoie et al., 2020). Reduced zooplankton biomass also results in reduced ammonium excretion, detrital PON and DON in the upper layer (Figures 56 and 59), that lead to a reduction of organic material that can be remineralized to ammonium (except in the GoM). This reduction in simulated ammonium concentration leads to a decline in flagellate biomass. The region where historical ammonium concentrations are the highest, the Magdalen Shallows, is predicted to see the most important decrease in ammonium, most likely due to a decline in the advection of organic matter from upstream areas (see Lavoie et al. 2020). The changes mentioned above are however significant with the three simulations in parts of the Scotian Shelf and GoM only. The decrease in flagellates simulated here is however contrary to what has been observed in some oceanic regions affected by warming and increasing stratification (Li et al., 2009) or theoretically expected (Moran et al., 2010). An in-depth analysis of the causes for this difference will be performed in a different document (journal article in prep.).

4.3 ACIDIFICATION

All future simulations show acidification over the domain with a decrease in pH_{total} and carbonate saturations at all depths (Figure 66 to 71). DIC is increasing everywhere in the future, especially in the GoM, except in the upper layer of the GSL and Scotian Shelf in the

simulation forced with HadGEM2-ES. Projected future changes in DIC in the upper layer in these regions (GSL, Scotian Shelf) are however not significant, contrary to the rest of the domain and layers (Figure 62). As for salinity, alkalinity decreases in the upper layers, and increases in the lower layers (Figure 64), consistent with an increased influence of Gulf Stream water in the water mixture entering the deep channels over the domain. These changes are significant in the upper layer, except in the GoM, in the intermediate layer in LSLE, NWGSL, and southern GSL, and in the deep channels of the GSL below 150 m. The greater DIC increase in the GoM results in part from the higher recycling of organic matter occurring in this region, as indicated by the increase in detrital PON, DON, and ammonium (Figures 38, 56, and 59). By 2090, the upper layer of the entire GSL and of the Scotian Shelf is expected to be undersaturated with respect to aragonite as well as most of the bottom layer in all shelf areas of the model domain (Figure 72). Shallower areas of the GSL and central and eastern Scotian Shelf are also expected to be undersaturated with respect to calcite by 2090 (Figure 73). Even if critical calcium carbonate thresholds are to be reached later or not at all in the GoM, it is to note that this region experienced the greatest decline (see section 3.2.19).

5 CONCLUSION

This study predicts widespread warming, freshening of the upper layers with an increase in salinity at depth, as well as a pH and calcium carbonate saturations decline in the coming decades in the GSL, GoM, and Scotian Shelf regions. The northern part of the domain (GSL) already shows critical conditions in term of deoxygenation (not shown) and acidification. The GoM and the western Scotian Shelf are less affected by acidification at this time and the carbonate system might not reach the critical 1.0 and 1.5 thresholds within the next decades, but the simulations suggest that these regions will undergo the greatest changes in terms of acidification, which can also cause an important stress to marine organisms. Changes in nitrogenous nutrients and in the biomass of phytoplankton and zooplankton were more variable from one region to the other, from one vertical layer to the other, and were not always significant. In Figure 74, we presented an index of cumulative stressors (number of variables that displayed a significant change at every grid cell and in different layers) to identify the areas most affected by climate change. The combination of multiple

environmental changes is bound to affect many marine species living in these regions (Brennan et al., 2016; Shackell et al., 2013; Stortini et al., 2017). As a next step, the simulations will be recomputed to include oxygen changes and a more in-depth analysis of the drivers of the different changes will be performed and reported in a scientific paper.

ACKNOWLEDGEMENTS

We acknowledge the World Climate Research Programme's Working Group on Coupled Modelling, which is responsible for CMIP, and we thank the climate modeling groups (listed in Table 1 of this paper) for producing and making available their model output. For CMIP, the U.S. Department of Energy's Program for Climate Model Diagnosis and Intercomparison provided coordinating support and led the development of software infrastructure in partnership with the Global Organization for Earth System Science Portals.

We thank Blair Greenan, Michel Gosselin, and Nathalie Roy for their careful review of the report. We also thank Piero Calosi for a fruitful discussion on the sensitivity of different organisms to Omega values and Olivier Riche for the edition of some figures.

REFERENCES

- Baumann, H., Talmage, S.C., and Gobler, C.J. 2012. Reduced early life growth and survival in a fish in direct response to increased carbon dioxide. *Nat. Clim. Change* 2: 38–41.
- Bednarsek, N., Feely, R.A., Beck, M.W., et al. 2020. Exoskeleton dissolution with mechanoreceptor damage in larval Dungeness crab related to severity of present-day ocean acidification vertical gradients. *Sci. Total Environ.* 716, doi: <https://doi.org/10.1016/j.scitotenv.2020.136610>Get.
- Bianucci, L., Fennel, K., Chabot, D., Shackell, N., and Lavoie, D. 2016. Ocean biogeochemical models as management tools: a case study for Atlantic wolffish and declining oxygen. *ICES J. Mar. Sci.* 73(2): 263-274.
- Boyce, D.G., Lewis, M.R., and Worm, B. 2010. Global phytoplankton decline over the past century. *Nature* 466(7306): 591-596.
- Brennan, C.E., Blanchard, H., and Fennel, K. 2016. Putting temperature and oxygen thresholds of marine animals in context of environmental change: A regional perspective for the Scotian Shelf and Gulf of St. Lawrence. *PLoS One* 11(12): e0167411.
- Brickman, D., and Drozdowski, A. 2012. Development and validation of a regional shelf model for Maritime Canada based on the NEMO-OPA circulation model. *Can. Tech. Rep. Hydrogr. Ocean Sci.* 278: vii+257 pp. <http://waves-vagues.dfo-mpo.gc.ca/Library/347377.pdf>.
- Cheung, W.W.L., Watson, R., and Pauly, D. 2013. Signature of ocean warming in global fisheries catch. *Nature* 497(7449): 365-368.
- Claret, M., Galbraith, E.D., Palter, J.B., Bianchi, D., Fennel, K., Gilbert, D., and Dunne, J.P. 2018. Rapid coastal deoxygenation due to ocean circulation shift in the northwest Atlantic. *Nat. Clim. Change* 8(10): 868-872, doi: 10.1038/s41558-018-0263-1.
- Curran, K., and Azetsu-Scott, K. 2012. Ocean acidification – State of the Scotian Shelf Report 28 pp. <http://coinatlantic.ca/images/documents/soss/ocean-acidification.pdf>.
- Dickson, A.G., Sabine, C.L., and Christian, J.R. 2007. Guide to Best Practices for Ocean CO₂ Measurements. PICES Special Publication 3. 191 pp.
- Doney, S.C., Fabry, V.J., Feely, R.A., and Kleypas, J.A. 2009. Ocean acidification: The other CO₂ problem. *Annu. Rev. Mar. Sci.* 1(1): 169-192.

Doney, S.C., Ruckelshaus, M., Duffy, J.E., et al. 2012. Climate change impacts on marine ecosystems. *Annu. Rev. Mar. Sci.* 4: 11-37.

Gilbert, D., Sundby, B., Gobeil, C., Mucci, A., and Tremblay, G.-H. 2005. A seventy-two-year record of diminishing deep-water oxygen in the St. Lawrence estuary: The northwest Atlantic connection. *Limnol. Oceanogr.* 50(5): 1654-1666.

Gledhill, D.K., White, M.M., Salisbury, J., et al. 2015. Ocean and coastal acidification off New England and Nova Scotia. *Oceanography* 28(2): 182-197.

Guo, L., Perrie, W., Long, Z., Chassé, J., Zhang, Y., and Huang, A. 2013. Dynamical downscaling over the Gulf of St. Lawrence using the Canadian Regional Climate Model. *Atmos.-Ocean* 51(3): 265-283.

Jolliff, J., C. Kindle, J., Shulman, I., Penta, B., Friedrichs, M., Helber, R., and Arnone, R. 2009. - Summary diagrams for coupled hydrodynamic-ecosystem model skill assessment. *Journal of Marine Systems* 76: 64-82.

Lambert, N., Chassé, J., Perrie, W., Long, Z., Guo, L., and Morrison, J. 2013. Projection of future river runoffs in Eastern Atlantic Canada from global and regional climate models. *Can. Tech. Rep. Hydrogr. Ocean Sci.* 288: viii+234 pp.

Lavoie, D., Lambert, N., Ben Mustapha, S., and van der Baaren, A. 2013. Projections of future physical and biogeochemical conditions in the Northwest Atlantic from CMIP5 Global Climate Models. *Can. Tech. Rep. Hydrogr. Ocean. Sci.* 285 xiv + 156 pp pp. <http://waves-vagues.dfo-mpo.gc.ca/Library/349066.pdf>.

Lavoie, D., Lambert, N., and Gilbert, D. 2019. Projections of future trends in biogeochemical conditions in the Northwest Atlantic using CMIP5 Earth System Models. *Atmos.-Ocean* 57(1): 18-40.

Lavoie, D., Lambert, N., Starr, M., et al. 2020. GSBM: a modelling tool for fisheries and ocean management in the Gulf of St. Lawrence. In prep.

Li, W.K.W., McLaughlin, F.A., Lovejoy, C., and Carmack, E.C. 2009. Smallest algae thrive as the Arctic Ocean freshens. *Science* 326(5952): 539.

Loder, J.W., van der Baaren, A., and Yashayaev, I. 2015. Climate comparisons and change projections for the Northwest Atlantic from six CMIP5 models. *Atmos.-Ocean* 53(5): 529-555.

Long, Z.X., Perrie, W., Chassé, J., Brickman, D., Guo, L.L., Drozdowski, A., and Hu, H.B. 2016. Impacts of climate change in the Gulf of St. Lawrence. *Atmos.-Ocean* 54(3): 337-351.

Lueker, T.J., Dickson, A.G., and Keeling, C.D. 2000. Ocean pCO₂ calculated from dissolved inorganic carbon, alkalinity, and equations for K₁ and K₂: validation based on laboratory measurements of CO₂ in gas and seawater at equilibrium. *Mar. Chem.* 70(1-3): 105-119.

MacKenzie, B.R., Payne, M.R., Boje, J., Hoyer, J.L., and Siegstad, H. 2014. A cascade of warming impacts brings bluefin tuna to Greenland waters. *Global Change Biology* 20(8): 2484-2491.

Moran, X.A.G., Lopez-Urrutia, A., Calvo-Diaz, A., and Li, W.K.W. 2010. Increasing importance of small phytoplankton in a warmer ocean. *Global Change Biology* 16(3): 1137-1144.

Moss, R.H., Edmonds, J.A., Hibbard, K.A., et al. 2010. The next generation of scenarios for climate change research and assessment. *Nature* 463(7282): 747-756.

Mucci, A., Starr, M., Gilbert, D., and Sundby, B. 2011. Acidification of Lower St. Lawrence Estuary bottom waters. *Atmos.-Ocean* 49(3): 206-218.

Perrie, W., Long, Z.X., Chassé, J., Blokhina, M., Guo, L.L., and Hu, H.B. 2015. Projected changes in surface air temperature and surface wind in the Gulf of St. Lawrence. *Atmos.-Ocean* 53(5): 571-581.

Petrie, B., and Yeats, P. 2000. Annual and interannual variability of nutrients and their estimated fluxes in the Scotian Shelf, Gulf of Maine region. *Can. J. Fish. Aquat. Sci.* 57(12): 2536-2546.

Rhein, M., Rintoul, S.R., Aoki, S., et al. 2013. Observations: Ocean. *In* *Climate Change 2013: The Physical Science Basis. Contribution of Working Group I to the Fifth Assessment Report of the Intergovernmental Panel on Climate Change*. Edited by T. F. Stocker, et al. Cambridge University Press, Cambridge, United Kingdom and New York, NY, USA. pp. 255-315.

Schmidtko, S., Stramma, L., and Visbeck, M. 2017. Decline in global oceanic oxygen content during the past five decades. *Nature* 542(7641): 335-339.

Shackell, N.L., Greenan, B.W., Pepin, P., Chabot, D., and Warburton, A. 2013. Climate change impacts, vulnerabilities and opportunities (IVO) analysis of the Marine Atlantic Basin. *Can. Manuscr. Rep. Fish. Aquat. Sci.* xvi + 366 pp.

Smith, P.C., Petri, B., and Mann, C.R. 1978. Circulation, variability, and dynamics of the Scotian Shelf and Slope. *J. Fish. Res. Board Can.* 35(8): 1067-1083.

Stortini, C.H., Chabot, D., and Shackell, N.L. 2017. Marine species in ambient low-oxygen regions subject to double jeopardy impacts of climate change. *Global Change Biology* 23(6): 2284-2296.

Talmage, S.C., and Gobler, C.J. 2009. The effects of elevated carbon dioxide concentrations on the metamorphosis, size, and survival of larval hard clams (*Mercenaria mercenaria*), bay scallops (*Argopecten irradians*), and Eastern oysters (*Crassostrea virginica*). *Limnol. Oceanogr.* 54: 2072–2080.

Talmage, S.C., and Gobler, C.J. 2010. Effects of past, present, and future ocean carbon dioxide contrations on the growth and survival of larval shellfish *Proc. Natl. Acad. Sci. USA.* 107: 17246–17251.

Townsend, D.W., Pettigrew, N.R., Thomas, M.A., Neary, M.G., McGillicuddy, D.J., and O'Donnell, J. 2015. Water masses and nutrient sources to the Gulf of Maine. *J. Mar. Res.* 73(3-4): 93-122.

Yeats, P., Ryan, S., and Harrison, G. 2010. Temporal trends in nutrient and oxygen concentrations in the Labrador Sea and on the Scotian Shelf. *AZMP Bulletin PMZA* 9 23-27 pp. <http://waves-vagues.dfo-mpo.gc.ca/Library/365688.pdf>.

Zeebe, R.E., and Wolf-Gladrow, D. 2001. *CO₂ in Seawater: Equilibrium, Kinetics, Isotopes*, Edited by D. Halpern, 360 pp., Elsevier Science.

TABLES

Table 1. Water temperature trends ($^{\circ}\text{C dec}^{-1}$) over the 1980 to 2099 period in three different depth layers, for the Gulf of St. Lawrence (GSL), Scotian Shelf (SS) and Gulf of Maine (GoM) for the simulations forced with MPI-ESM-LR, HadGEM2-ES, and CanESM2 under the RCP 8.5 scenario.

GSL	MPI-ESM-LR	HadGEM2-ES	CanESM2
0-50	+0.296	+0.527	+0.512
50-150	+0.363	+0.632	+0.567
150-300	+0.690	+0.713	+0.703
SS	MPI-ESM-LR	HadGEM2-ES	CanESM2
0-50	+0.384	+0.605	+0.493
50-150	+0.423	+0.609	+0.385
150-300	+0.519	+0.587	+0.422
GoM	MPI-ESM-LR	HadGEM2-ES	CanESM2
0-50	+0.384	+0.572	+0.467
50-150	+0.412	+0.621	+0.529
150-300	+0.498	+0.681	+0.818

Table 2. Water salinity trends (PSU dec^{-1}) over the 1980 to 2099 period in three different depth layers, for the Gulf of St. Lawrence (GSL), Scotian Shelf (SS) and Gulf of Maine (GoM) for the simulations forced with MPI-ESM-LR, HadGEM2-ES, and CanESM2 under the RCP 8.5 scenario.

GSL	MPI-ESM-LR	HadGEM2-ES	CanESM2
0-50	-0.120	-0.234	-0.138
50-150	-0.064	-0.082	-0.065
150-300	+0.078	+0.082	+0.084
SS	MPI-ESM-LR	HadGEM2-ES	CanESM2
0-50	-0.082	-0.200	-0.117
50-150	-0.014	-0.049	-0.056
150-300	+0.062	+0.071	+0.034
GoM	MPI-ESM-LR	HadGEM2-ES	CanESM2
0-50	-0.043	-0.137	-0.091
50-150	+0.004	-0.020	-0.026
150-300	+0.066	+0.105	+0.119

Table 3. Dissolved inorganic carbon trends ($\text{mmol C m}^{-3} \text{ dec}^{-1}$) over the 1980 to 2099 period in three different depth layers, for the Gulf of St. Lawrence (GSL), Scotian Shelf (SS) and Gulf of Maine (GoM) for the simulations forced with MPI-ESM-LR, HadGEM2-ES, and CanESM2 under the RCP 8.5 scenario.

GSL	MPI-ESM-LR	HadGEM2-ES	CanESM2
0-50	+2.974	-2.638	+1.457
50-150	+5.300	+5.147	+5.475
150-300	+12.637	+12.195	+12.270
SS	MPI-ESM-LR	HadGEM2-ES	CanESM2
0-50	+5.517	-0.304	+4.064
50-150	+8.172	+7.061	+8.023
150-300	+12.422	+13.418	+13.420
GoM	MPI-ESM-LR	HadGEM2-ES	CanESM2
0-50	+10.126	+5.697	+8.703
50-150	+11.319	+9.643	+10.724
150-300	+12.921	+14.006	+14.249

Table 4. Total alkalinity trends ($\text{mmol C m}^{-3} \text{ dec}^{-1}$) over the 1980 to 2099 period in three different depth layers, for the Gulf of St. Lawrence (GSL), Scotian Shelf (SS) and Gulf of Maine (GoM) for the simulations forced with MPI-ESM-LR, HadGEM2-ES, and CanESM2 under the RCP 8.5 scenario.

GSL	MPI-ESM-LR	HadGEM2-ES	CanESM2
0-50	-8.119	-13.878	-8.751
50-150	-5.223	-6.001	-4.636
150-300	+5.334	+4.908	+6.292
SS	MPI-ESM-LR	HadGEM2-ES	CanESM2
0-50	-5.519	-11.267	-6.958
50-150	-2.311	-3.918	-3.849
150-300	+2.903	+3.802	+1.284
GoM	MPI-ESM-LR	HadGEM2-ES	CanESM2
0-50	-1.519	-5.756	-3.280
50-150	-0.152	-2.338	-1.862
150-300	+2.483	+4.328	+2.781

Table 5. pH_{total} trends (units per decade) over the 1980 to 2099 period in three different depth layers, for the Gulf of St. Lawrence (GSL), Scotian Shelf (SS) and Gulf of Maine (GoM) for the simulations forced with MPI-ESM-LR, HadGEM2-ES, and CanESM2 under the RCP 8.5 scenario.

GSL	MPI-ESM-LR	HadGEM2-ES	CanESM2
0-50	-0.039	-0.042	-0.039
50-150	-0.041	-0.047	-0.043
150-300	-0.035	-0.035	-0.031
SS	MPI-ESM-LR	HadGEM2-ES	CanESM2
0-50	-0.038	-0.040	-0.038
50-150	-0.040	-0.044	-0.042
150-300	-0.036	-0.036	-0.042
GoM	MPI-ESM-LR	HadGEM2-ES	CanESM2
0-50	-0.037	-0.038	-0.037
50-150	-0.039	-0.043	-0.043
150-300	-0.038	-0.038	-0.046

Table 6. Aragonite saturation trends (units per decade) over the 1980 to 2099 period in three different depth layers, for the Gulf of St. Lawrence (GSL), Scotian Shelf (SS) and Gulf of Maine (GoM) for the simulations forced with MPI-ESM-LR, HadGEM2-ES, and CanESM2 under the RCP 8.5 scenario.

GSL	MPI-ESM-LR	HadGEM2-ES	CanESM2
0-50	-0.082	-0.082	-0.073
50-150	-0.063	-0.066	-0.059
150-300	-0.036	-0.037	-0.030
SS	MPI-ESM-LR	HadGEM2-ES	CanESM2
0-50	-0.085	-0.084	-0.086
50-150	-0.068	-0.072	-0.081
150-300	-0.067	-0.069	-0.087
GoM	MPI-ESM-LR	HadGEM2-ES	CanESM2
0-50	-0.094	-0.091	-0.097
50-150	-0.086	-0.087	-0.093
150-300	-0.073	-0.066	-0.076

FIGURES

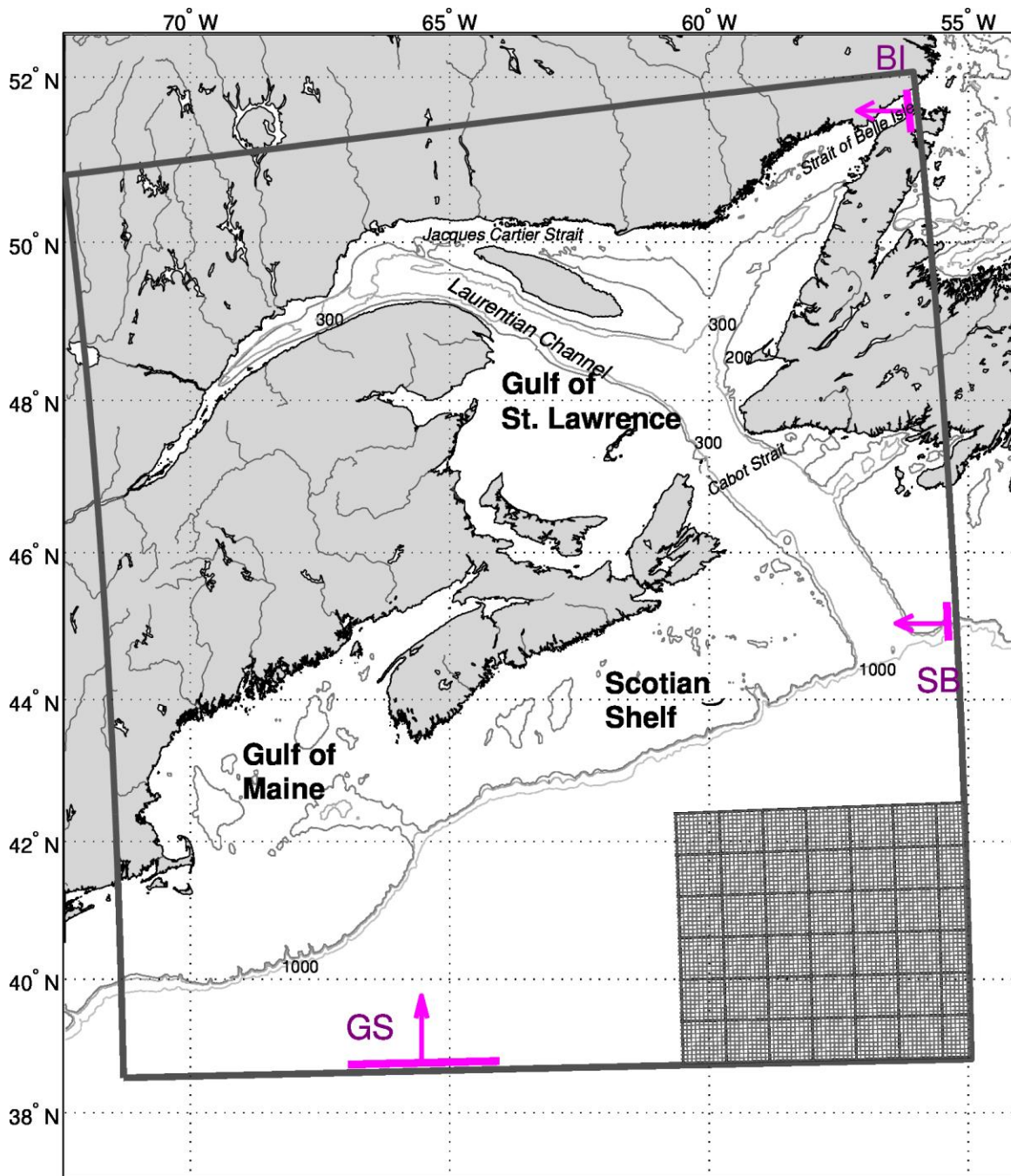


Figure 1. Map of the study area showing the model domain, with a small sub-area of the grid in the lower right corner. The 200, 300 and 1000 m depth contours are shown. The transects used in Figures 6 to 19 are depicted in pink (Strait of Belle Isle (BI), Shelf Break (SB) and Gulf Stream (GS)). The arrows indicate the positive direction for the currents in Figure 10.

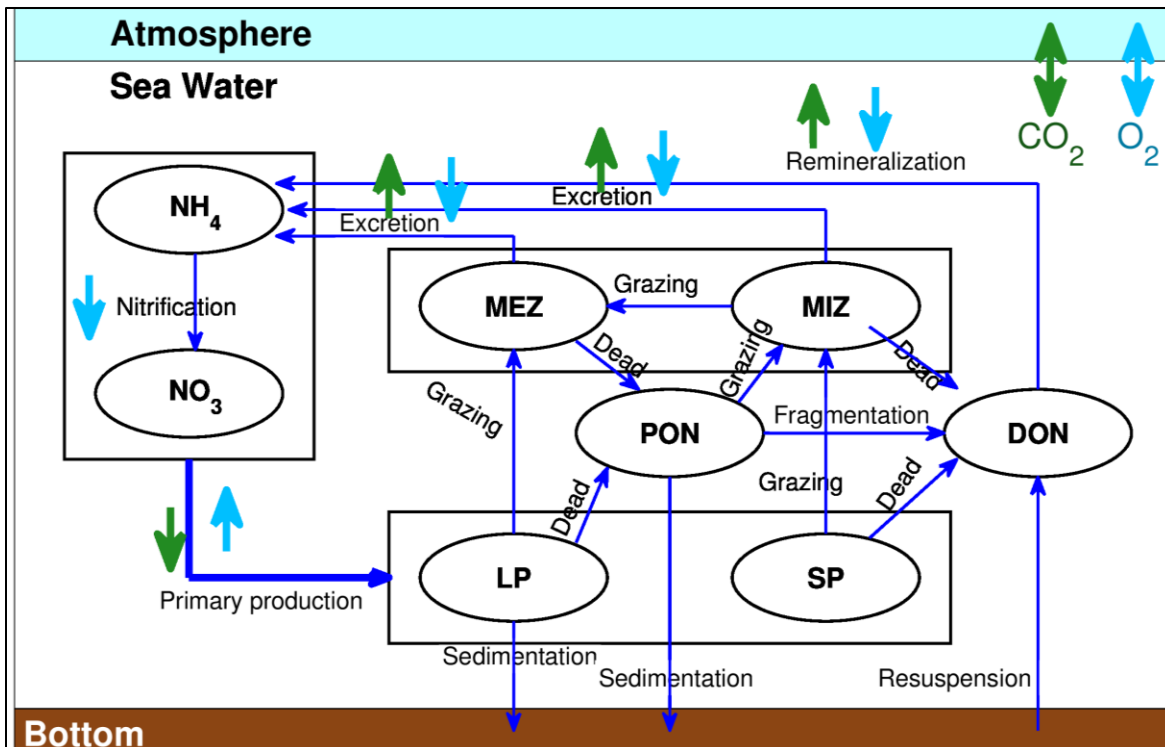


Figure 2. Conceptual planktonic ecosystem model including nitrate (NO_3), ammonium (NH_4), large phytoplankton (LP), small phytoplankton (SP), mesozooplankton (MEZ), microzooplankton (MIZ), detrital particulate organic nitrogen (PON), and dissolved organic nitrogen (DON). The dark blue arrows represent nitrogen fluxes between the biological components. The pale blue arrow represents the oxygen (O_2) fluxes (production, consumption and air-sea exchange) and the green arrow represents the air-sea carbon dioxide (CO_2) fluxes and the dissolved inorganic carbon production and consumption.

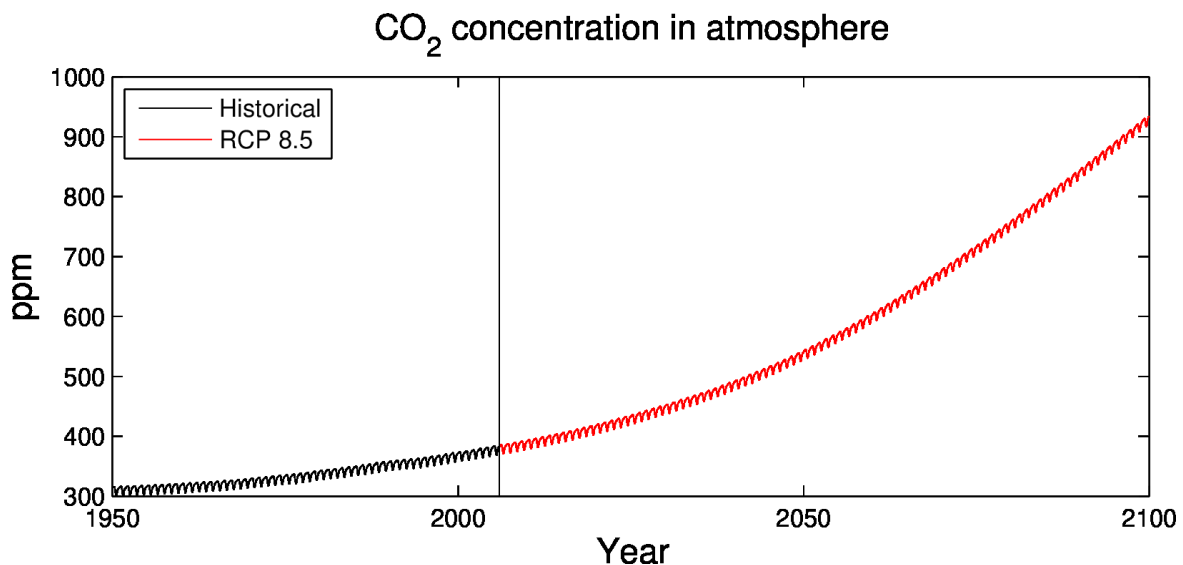


Figure 3. Concentration of carbon dioxide (CO_2) in the atmosphere (ppm) for the Representative Concentration Pathway RCP 8.5.

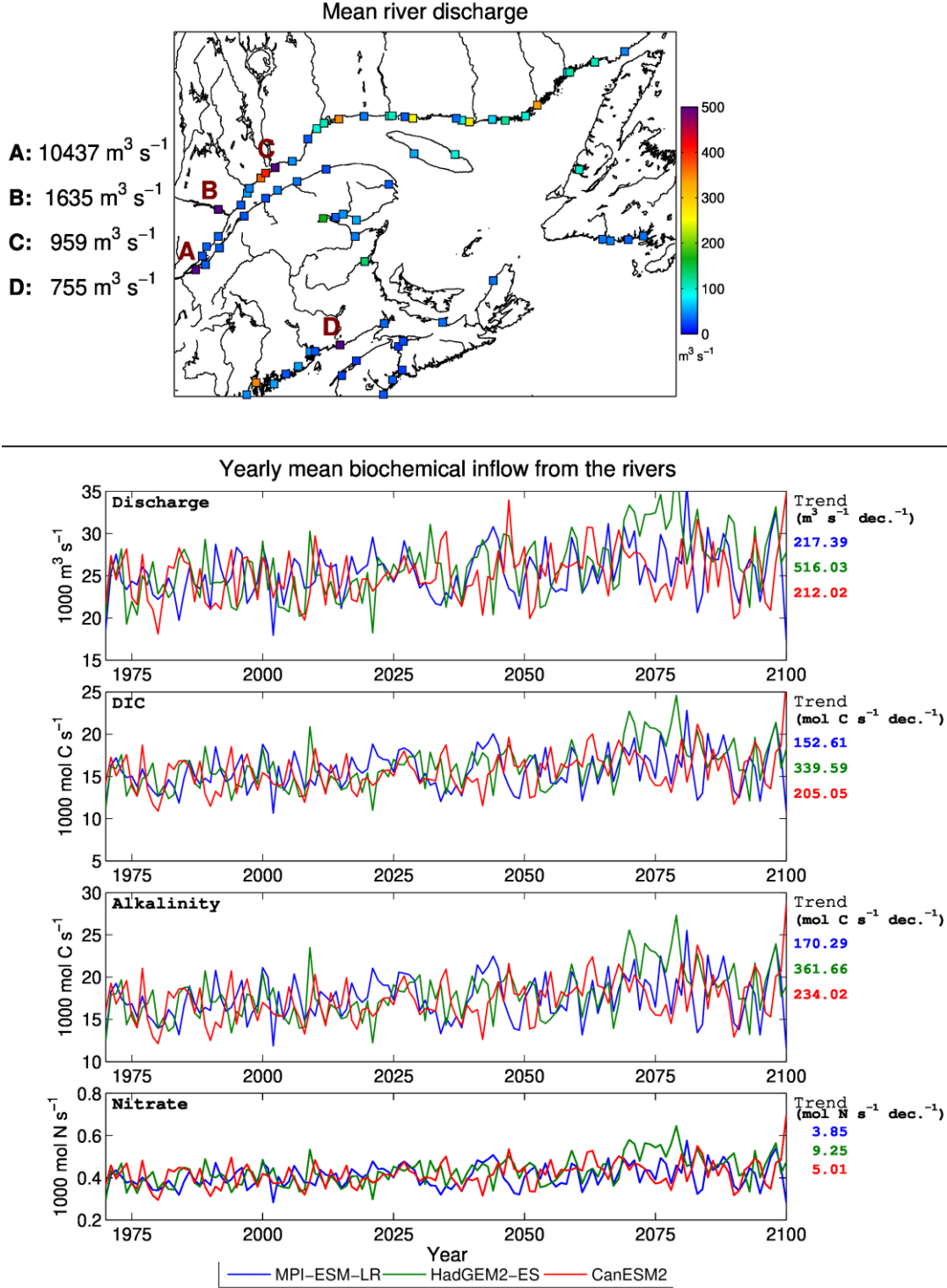


Figure 4. Upper panel (map): Mean discharge of the 78 rivers flowing into the model domain calculated with the hydrological model (Lambert et al., 2013) using precipitation and evaporation from the three Earth System Models averaged over the 1970-2099 period. The mean discharge of 4 majors rivers (A. St. Lawrence, B. Saguenay, C. Manicouagan, D. St. John) is displayed on the left-hand side of the panel. Four lower panels: Annual runoff calculated with each model, and corresponding total river flux of dissolved inorganic carbon (mol C s^{-1}), alkalinity (mol C s^{-1}), and nitrate (mol N s^{-1}).

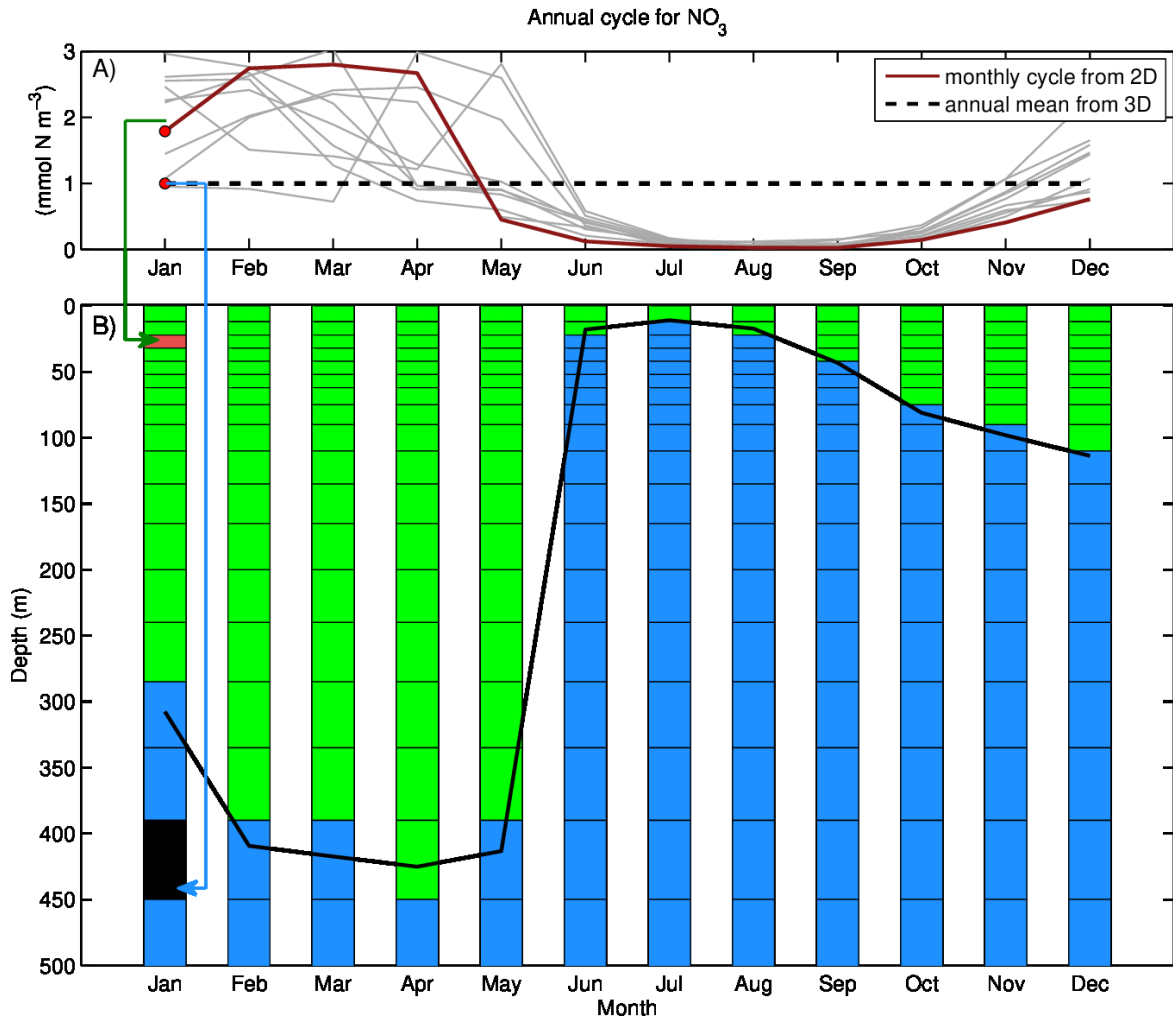


Figure 5. A) Normalized annual cycle of surface nitrate (NO₃) concentration (mmol N m⁻³) calculated from the surface 2D fields of MPI-ESM-LR at a randomly selected location at the southwest end of the domain. One out of four years (between 2061 and 2070) are shown in gray and the red line shows year 2061. The corresponding annual anomaly calculated from the 3D field is displayed as a dashed line. (B) Schematic of how the anomalies for the biogeochemical variables are applied at the open boundary for every month of each year. The monthly nitrate concentration at the boundary is obtained by adding/removing the monthly anomaly to/from the climatological value. For grid cells above the mixed layer (in green), depicted by the black line, the monthly anomaly estimated in (A) is used. For grid cells below the mixed layer (in blue), the annual anomaly calculated from the 3D fields is used.

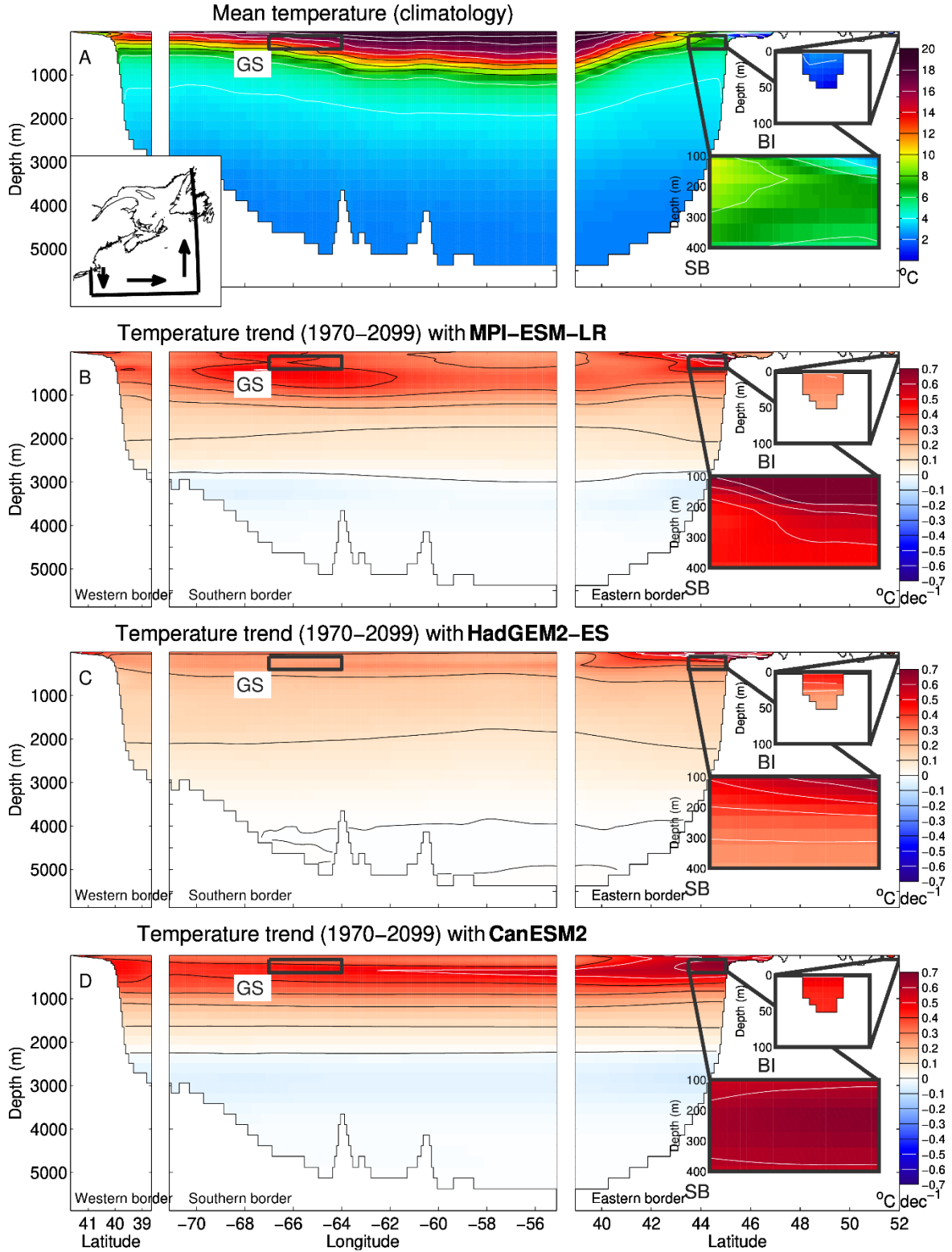


Figure 6. Mean observed temperature ($^{\circ}\text{C}$) from 1991 to 2010 (climatology) and 1970 to 2099 trends ($^{\circ}\text{C dec}^{-1}$) from the three Earth System Models (MPI-ESM-LR, HadGEM2-ES, and CanESM2), under the RCP 8.5 scenario, that are applied to the climatological values to obtain past and future conditions at the open boundaries. The open boundaries are displayed in the upper panel inset.

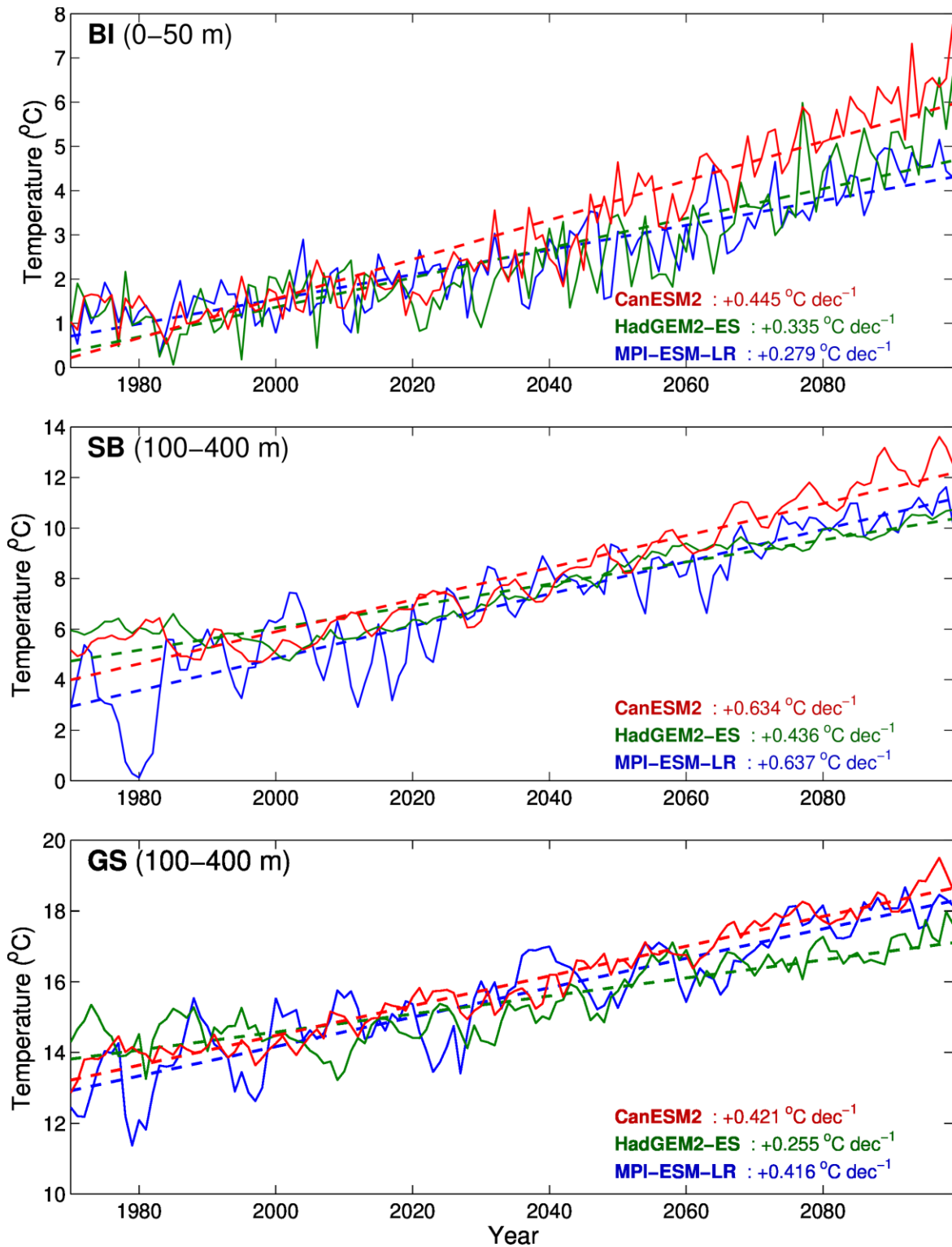


Figure 7. Yearly mean temperature and decadal trends for the 0-50 m or 100-400 m depth intervals across three open boundary zones (BI, SB, GS) defined in Figure 1, with the three Earth System Models (MPI-ESM-LR, HadGEM2-ES, and CanESM2) under the RCP 8.5 scenario.

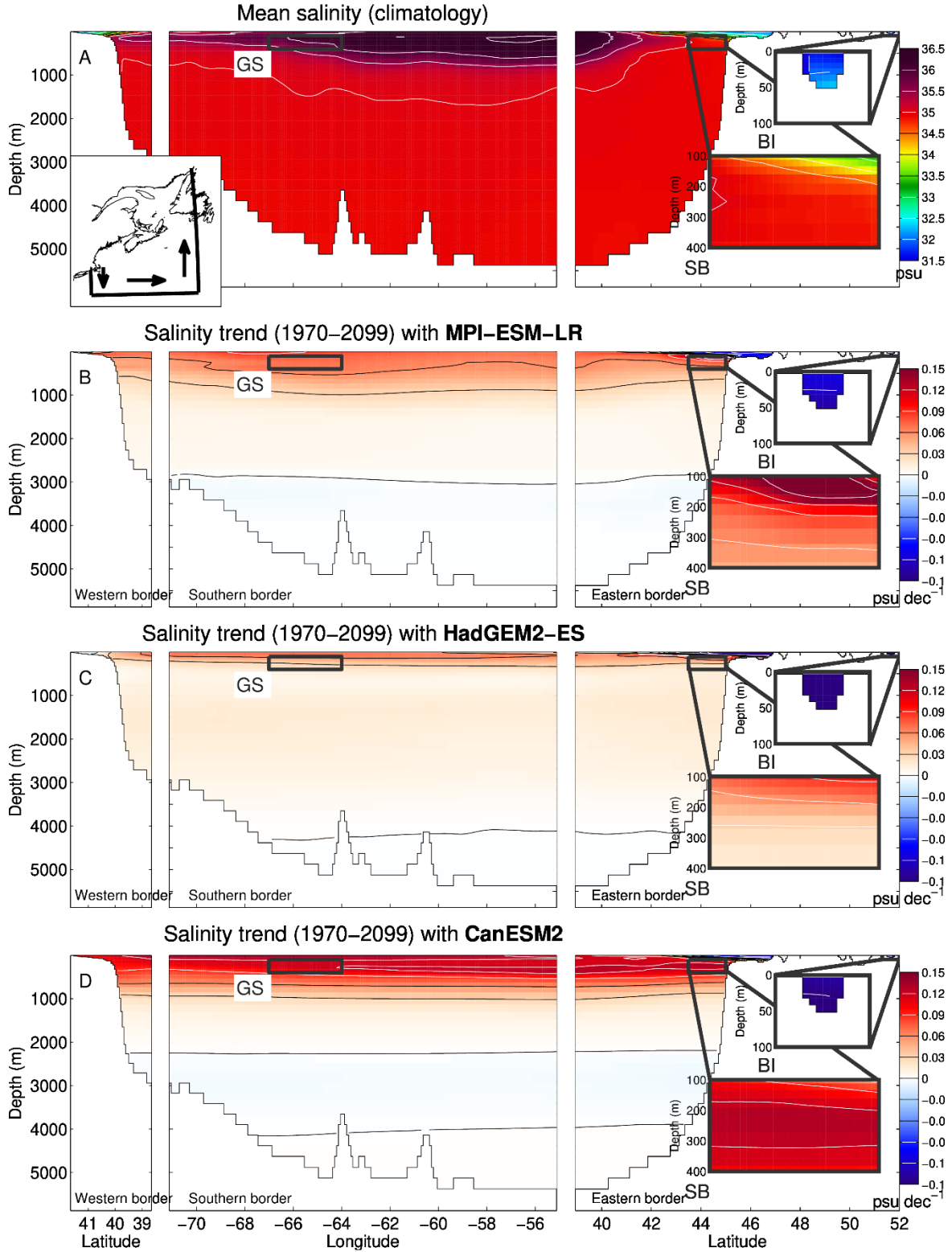


Figure 8. Mean observed salinity (psu) from 1991 to 2010 (climatology) and 1970 to 2099 trends (psu dec⁻¹) from the three Earth System Models (MPI-ESM-LR, HadGEM2-ES, and CanESM2), under the RCP 8.5 scenario, that are applied to the climatological values to obtain past and future conditions at the open boundaries. The open boundaries are displayed in the upper panel inset.

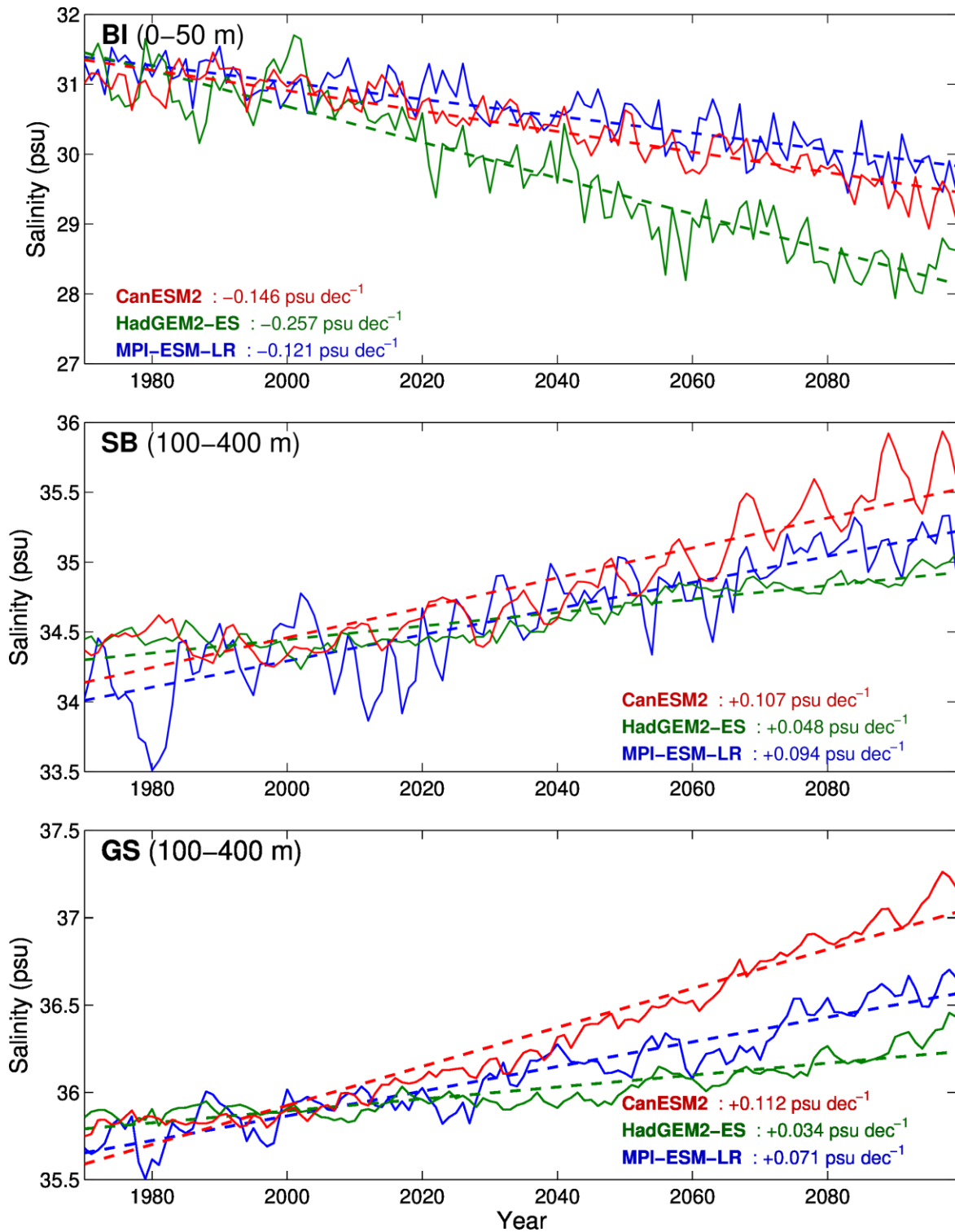


Figure 9. Yearly mean salinity and decadal trends for the 0-50 m or 100-400 m depth intervals across three open boundary zones (BI, SB, GS) defined in Figure 1, with the three Earth System Models (MPI-ESM-LR, HadGEM2-ES, and CanESM2) under the RCP 8.5 scenario.

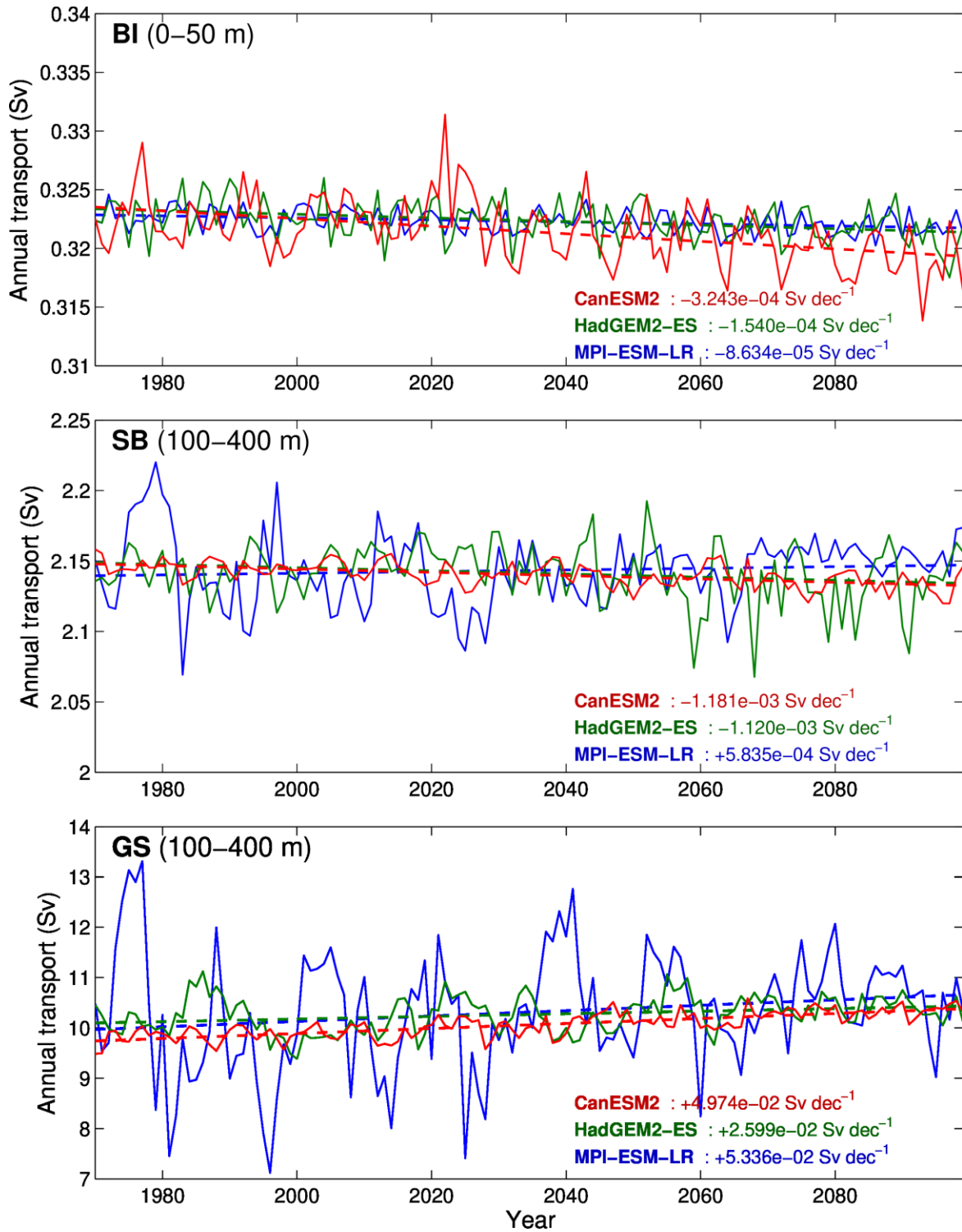


Figure 11. Yearly mean transport (Sv, $1 \text{ Sv} = 10^6 \text{ m}^3 \text{ s}^{-1}$) and decadal trends (Sv per decade) for the 0–50 m or 100–400 m depth intervals across three open boundary zones (BI, SB, GS) defined in Figure 1, with the three Earth System Models (MPI-ESM-LR, HadGEM2-ES, and CanESM2) under the RCP 8.5 scenario.

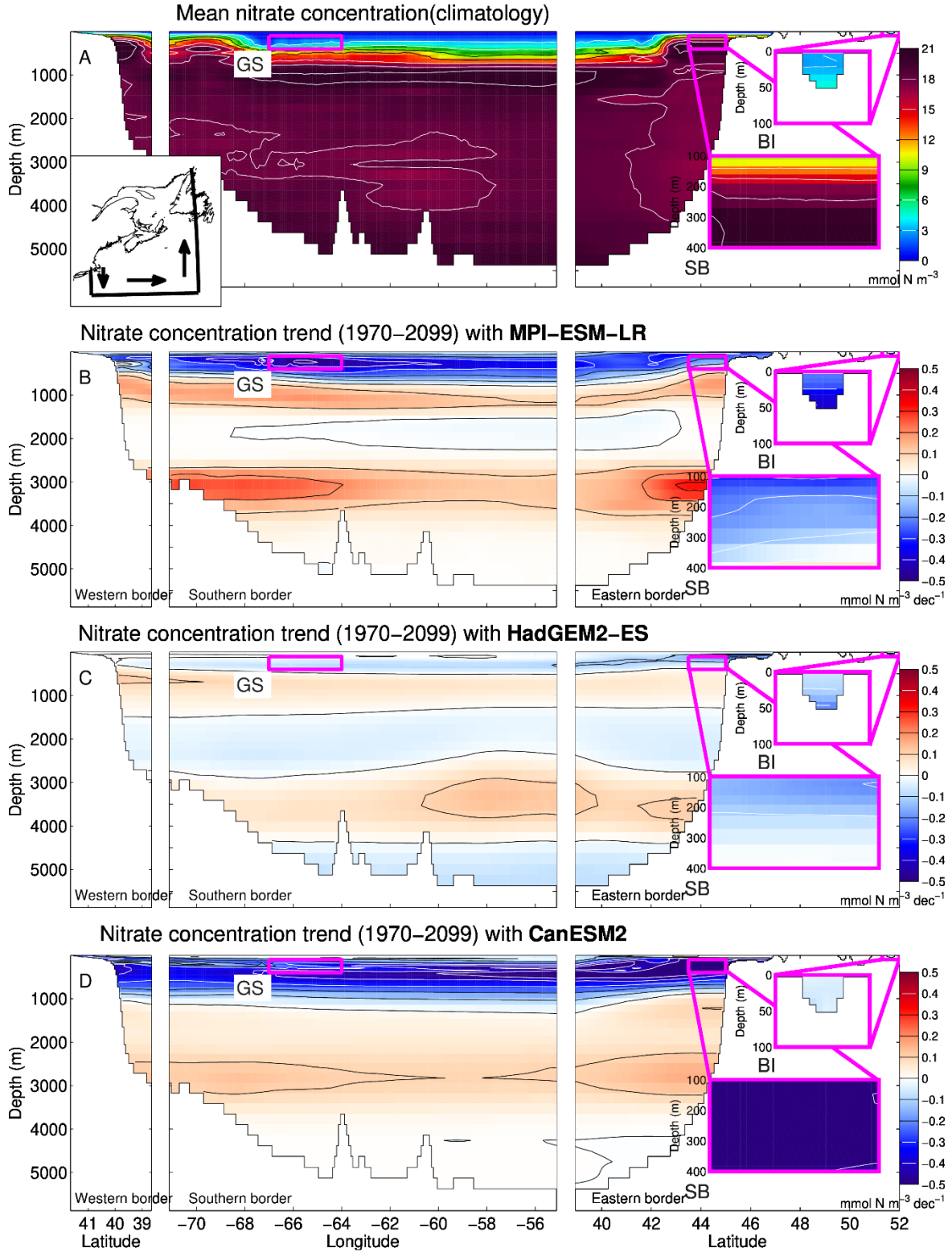


Figure 12. Mean nitrate concentration over 1991 to 2010 (climatology) and 1970 to 2099 trends at the open boundaries from the three Earth System Models (MPI-ESM-LR, HadGEM2-ES, and CanESM2), under the RCP 8.5 scenario, that are applied to the climatological values to obtain past and future boundary conditions. The open boundaries are displayed in the upper panel inset.

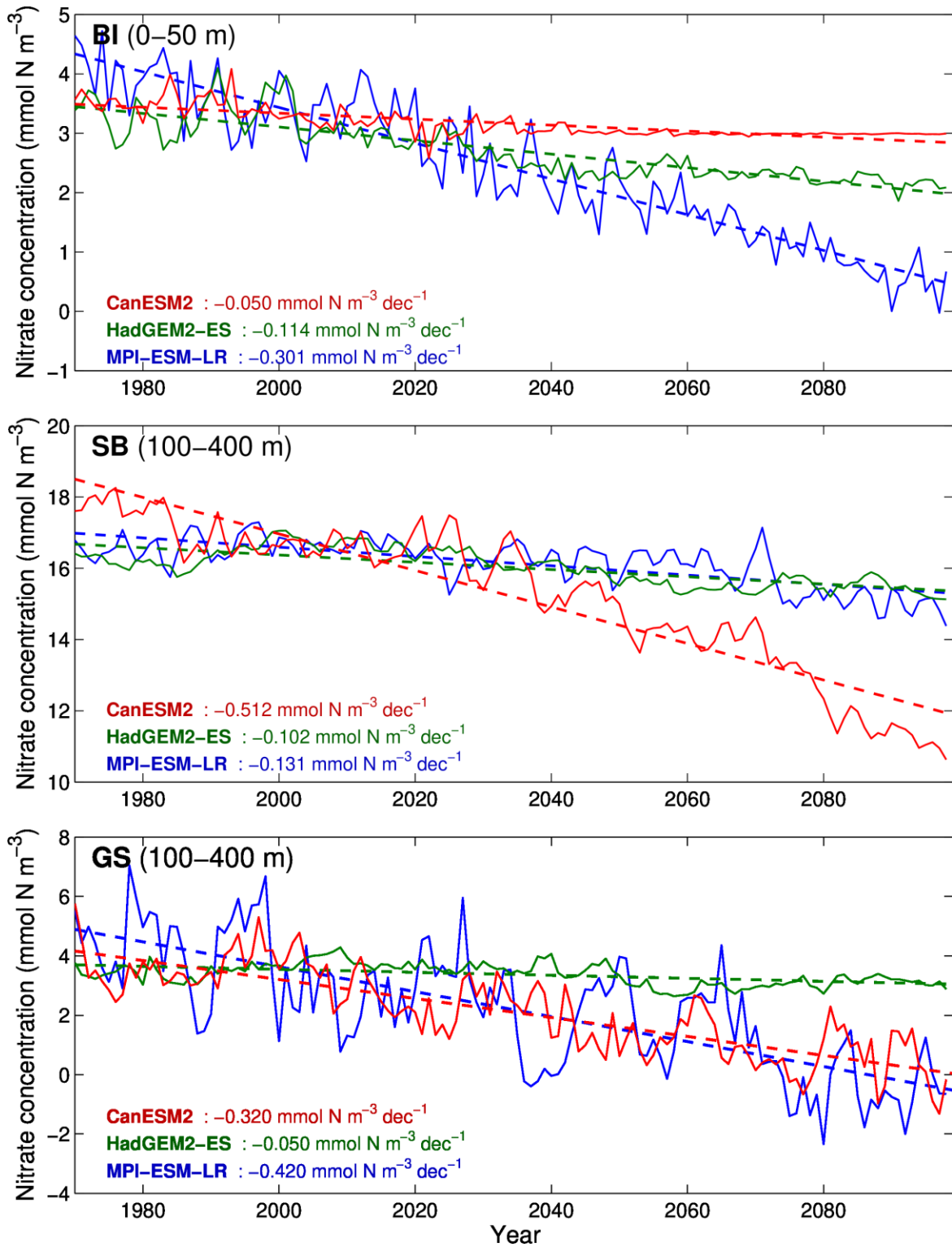


Figure 13. Yearly mean nitrate concentration and decadal trends for the 0–50 m or 100–400 m depth intervals across three open boundary zones (BI, SB, and GS) defined in Figure 1, with the three Earth System Models (MPI-ESM-LR, HadGEM2-ES, and CanESM2) under the RCP 8.5 scenario.

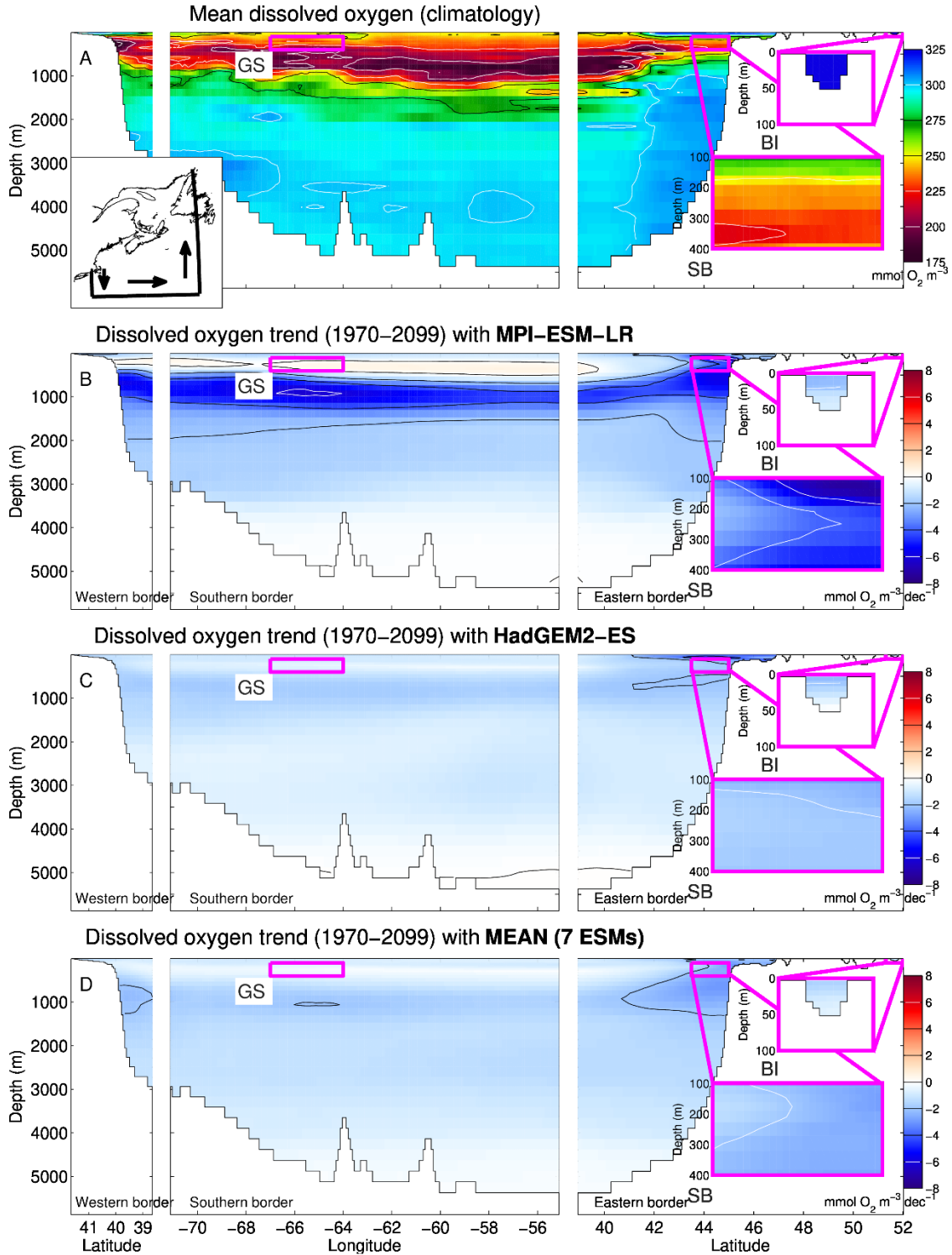


Figure 14. Mean dissolved oxygen concentration ($\text{mmol O}_2 \text{ m}^{-3}$) over 1991 to 2010 (climatology) and 1970 to 2009 trends ($\text{mmol O}_2 \text{ m}^{-3} \text{ dec}^{-1}$) at the open boundaries from the two Earth System Models (MPI-ESM-LR and HadGEM2-ES), and CanESM2 under the RCP 8.5 scenario. CanESM2 did not calculate oxygen concentration so we used the mean of the 7 ESMs available (Lavoie et al., 2019). These trends are applied to the climatological values to obtain future boundary conditions. The open boundaries are displayed in the upper panel inset.

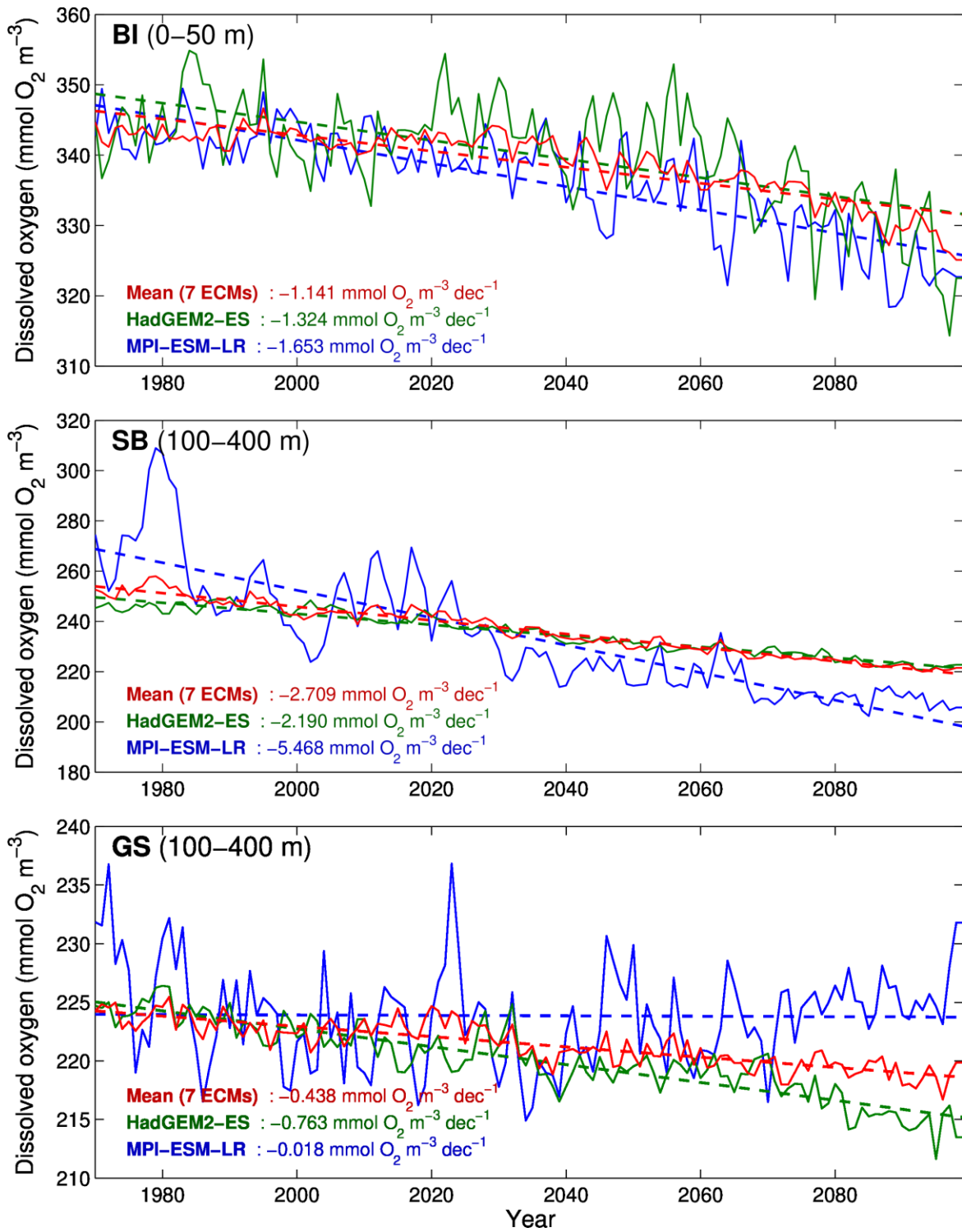


Figure 15. Yearly mean dissolved oxygen concentration and decadal trends for the 0–50 m or 100–400 m depth intervals across three open boundary zones (BI, SB, GS) defined in Figure 1, with two Earth System Models (MPI-ESM-LR and HadGEM2-ES) under the RCP 8.5 scenario. CanESM2 did not calculate oxygen concentration so we used the mean of the 7 ESMs available (Lavoie et al., 2019).

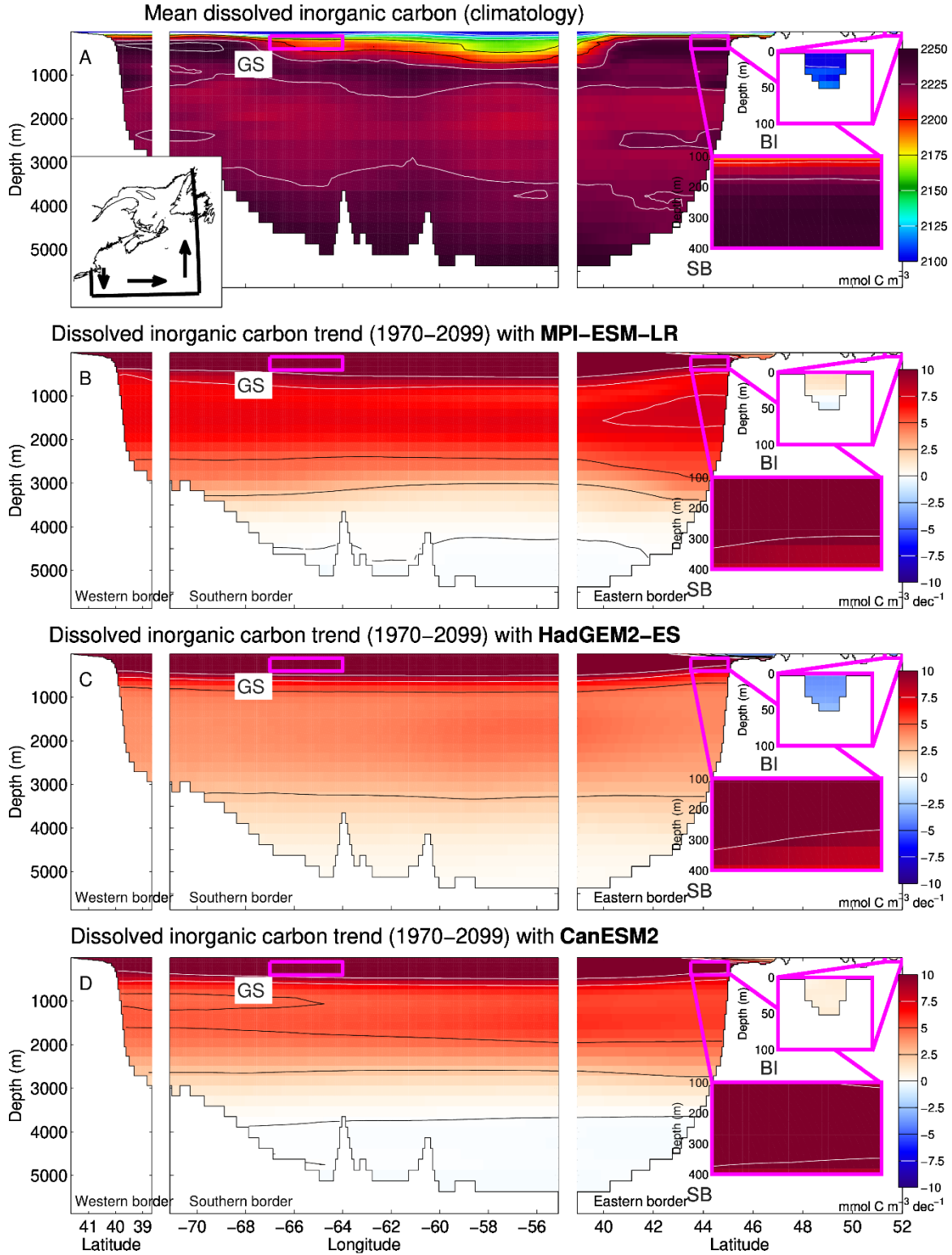


Figure 16. Mean dissolved inorganic carbon concentration over 1991 to 2010 (climatology) and 1970 to 2099 trends at the open boundaries from the three Earth System Models (MPI-ESM-LR, HadGEM2-ES, and CanESM2), under the RCP 8.5 scenario, that are applied to the climatological values to obtain past and future boundary conditions. The open boundaries are displayed in the upper panel inset.

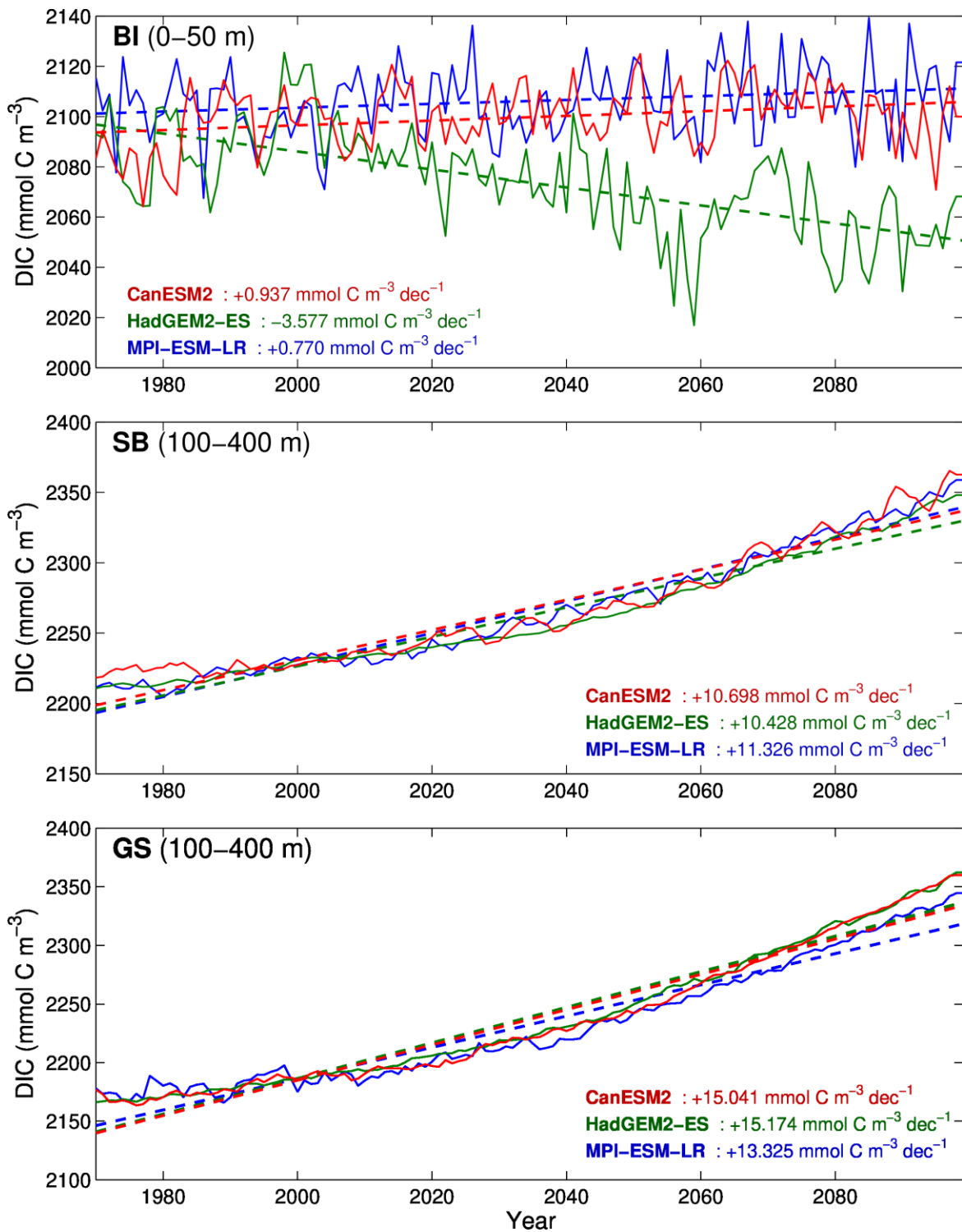


Figure 17. Yearly mean dissolved inorganic carbon (DIC) and decadal trends for the 0-50 m or 100-400 m depth intervals across three open boundary zones (BI, SB, GS) defined in Figure 1, with the three Earth System Models (MPI-ESM-LR, HadGEM2-ES, and CanESM2) under the RCP 8.5 scenario.

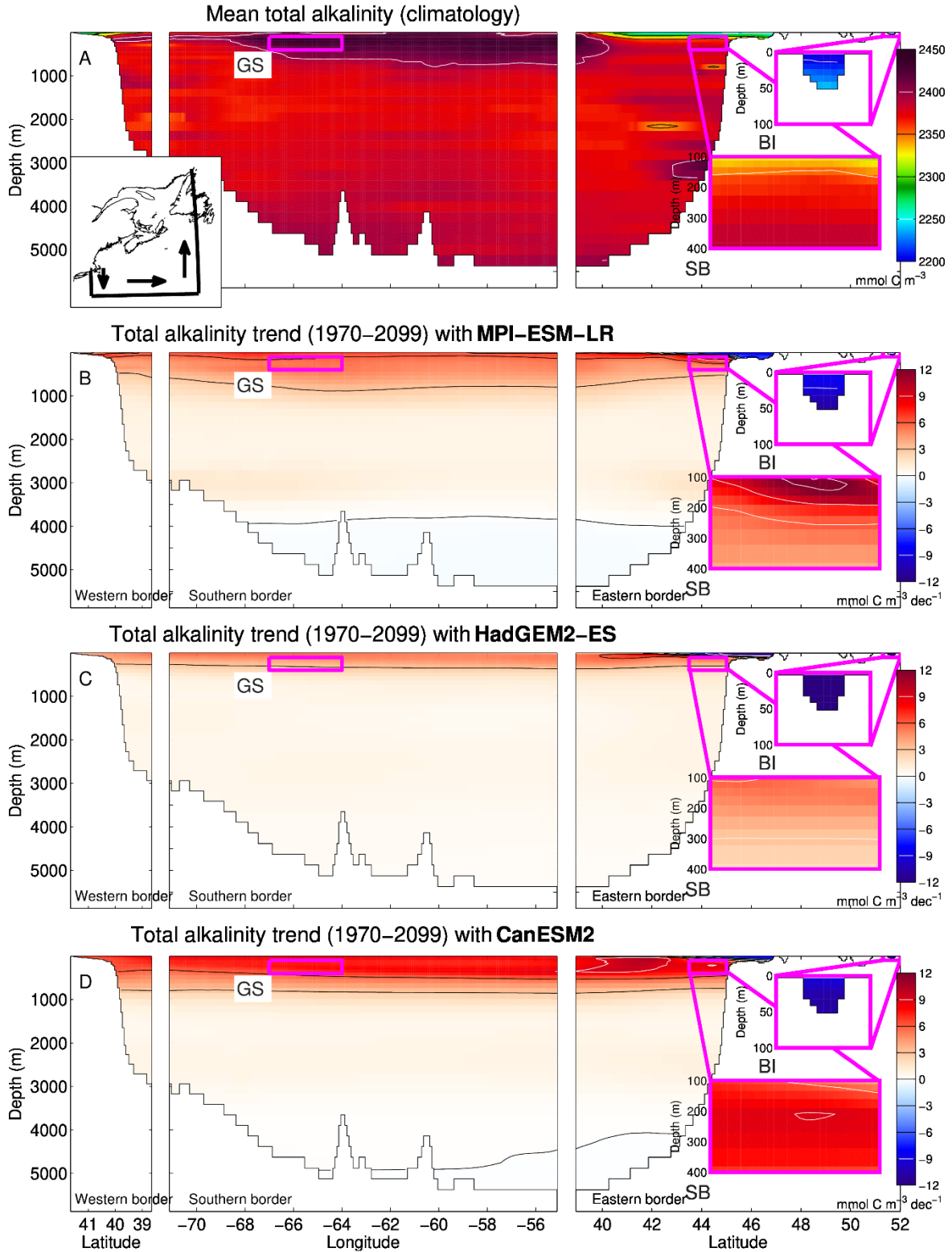


Figure 18. Mean total alkalinity over 1991 to 2010 (climatology) and 1970 to 2009 trends at the open boundaries from the three Earth System Models (MPI-ESM-LR, HadGEM2-ES, and CanESM2) under the RCP 8.5 scenario, that are applied to the climatological values to obtain past and future boundary conditions. The open boundaries are displayed in the upper panel inset.

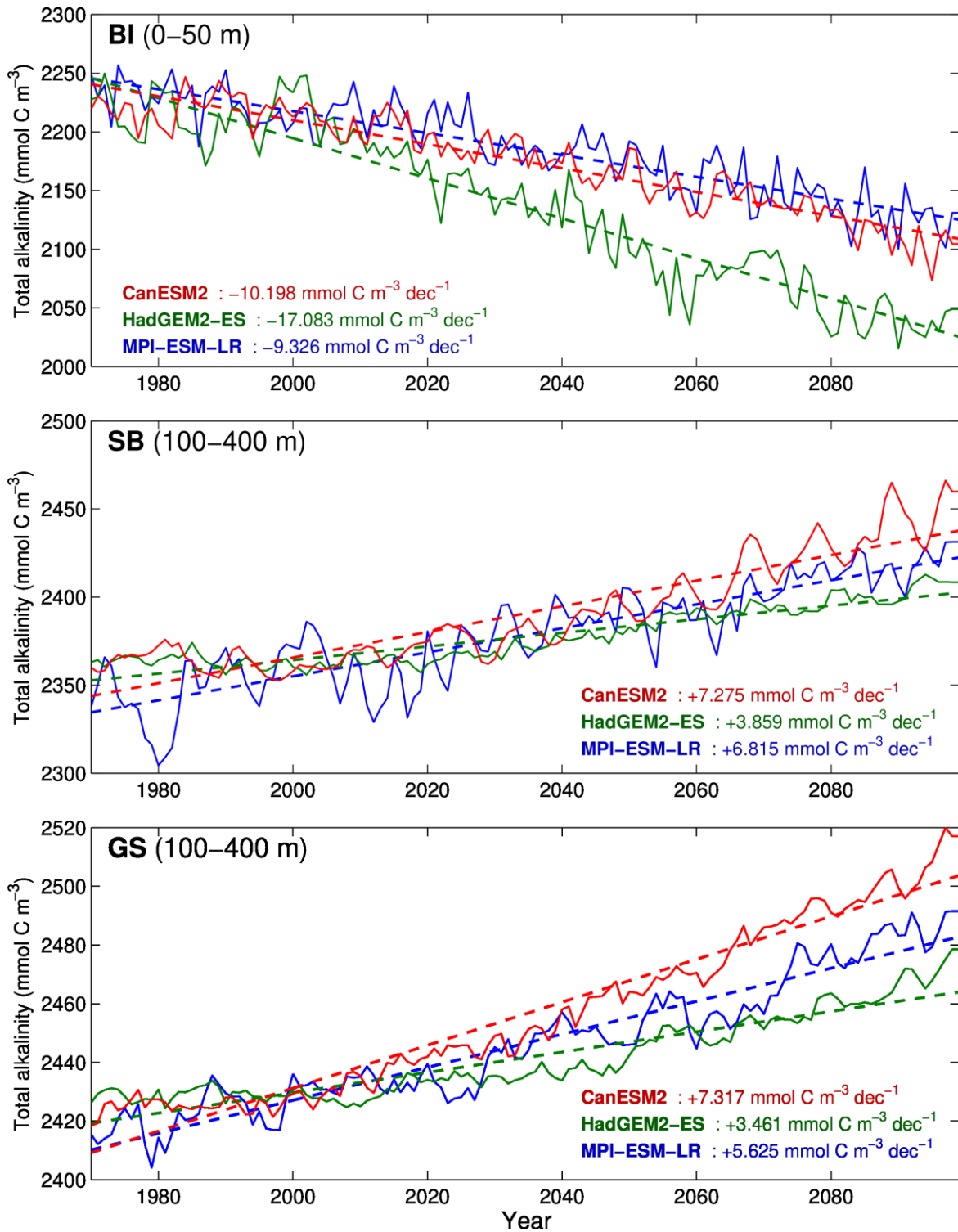


Figure 19. Yearly mean total alkalinity and 1970 to 2099 decadal trends for the 0–50 m or 100–400 m depth intervals across three open boundary zones (BI, SB, GS) defined in Figure 1, with the three Earth System Models (MPI-ESM-LR, HadGEM2-ES, and CanESM2) under the RCP 8.5 scenario.

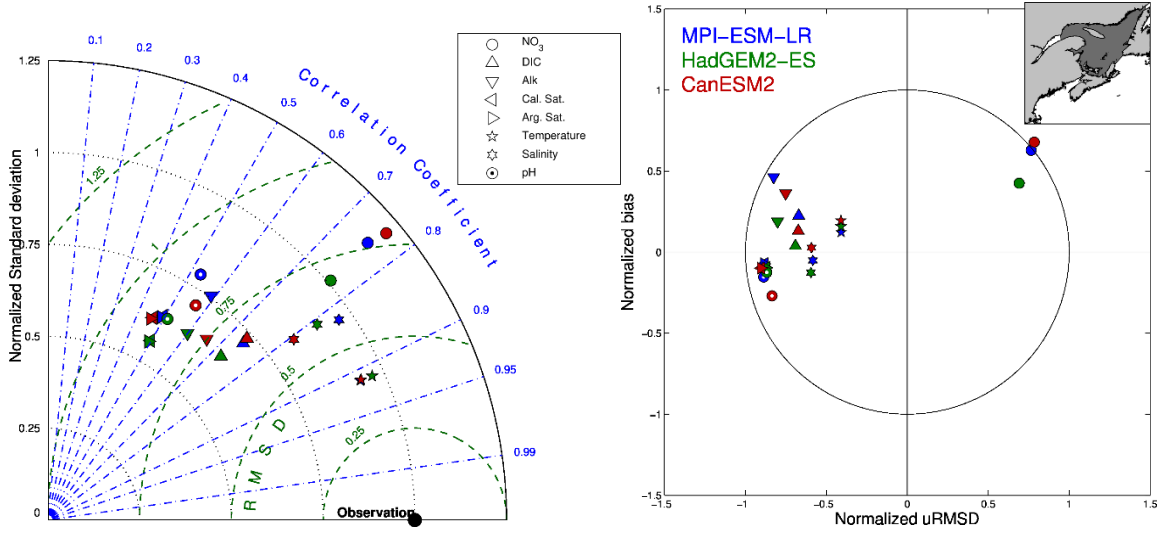


Figure 20. Taylor (left) and Target (right) diagrams for eight variables (see symbols in the box) for the three simulations (forced with MPI-ESM-LR in blue, with HadGEM2-ES in green, and with CANESM2 in red) for the Gulf of St. Lawrence (see inset in the top right corner). Model output averaged over 14.6 days is compared with in situ data.

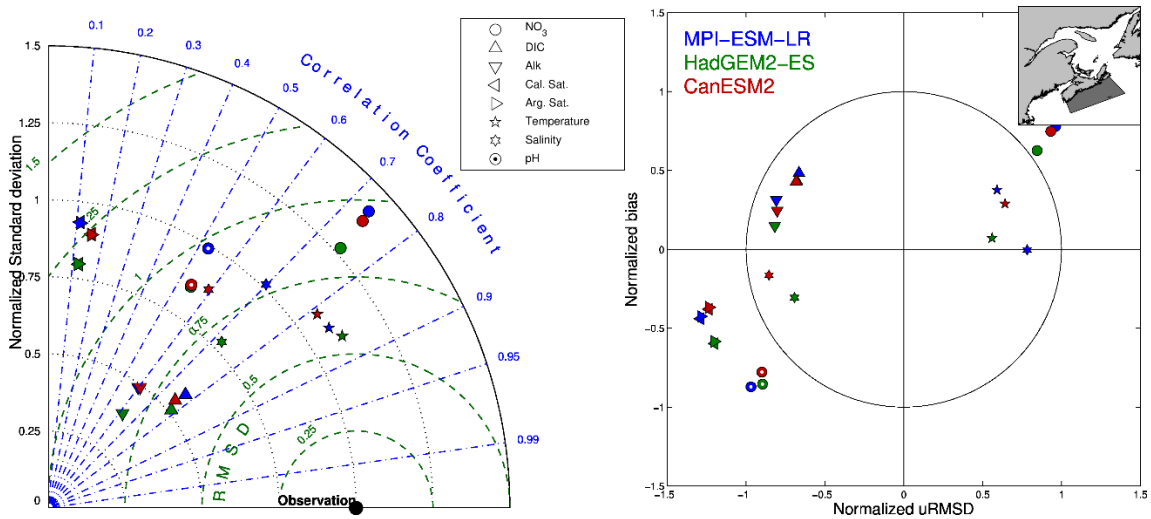


Figure 21. Taylor (left) and Target (right) diagrams for eight variables (see symbols in the box) for the three simulations (forced with MPI-ESM-LR in blue, with HadGEM2-ES in green, and with CANESM2 in red) for the Scotian Shelf (see inset in the top right corner). Model output averaged over 14.6 days is compared with in situ data.

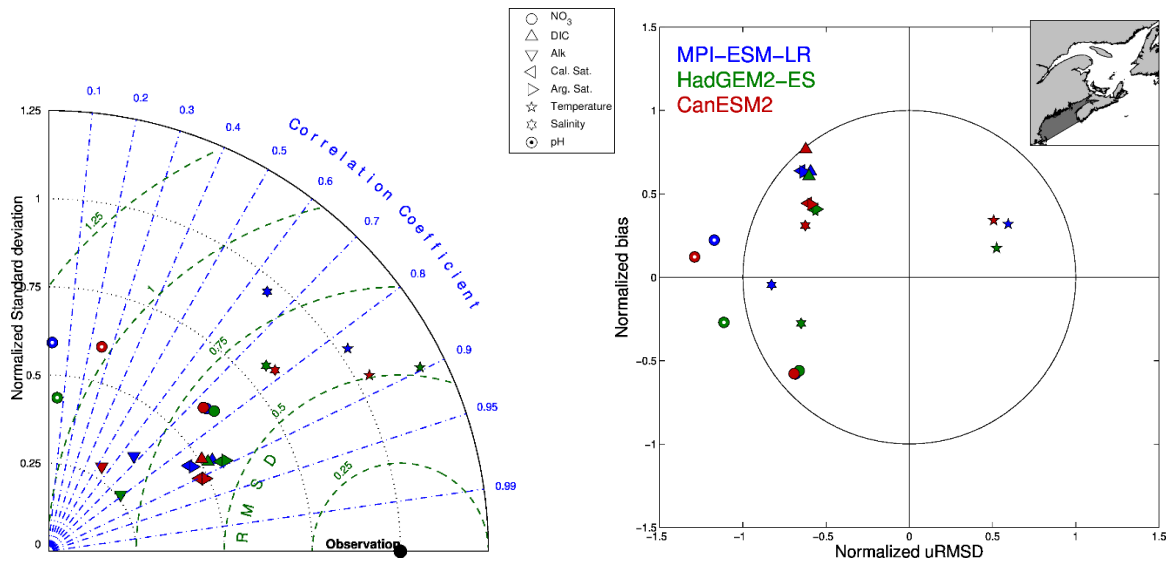


Figure 22. Taylor (left) and Target (right) diagrams for eight variables (see symbols in the box) for the three simulations (forced with MPI-ESM-LR in blue, with HadGEM2-ES in green, and with CANESM2 in red) for the Gulf of Maine (see inset in the top right corner). Model output averaged over 14.6 days is compared with in situ data.

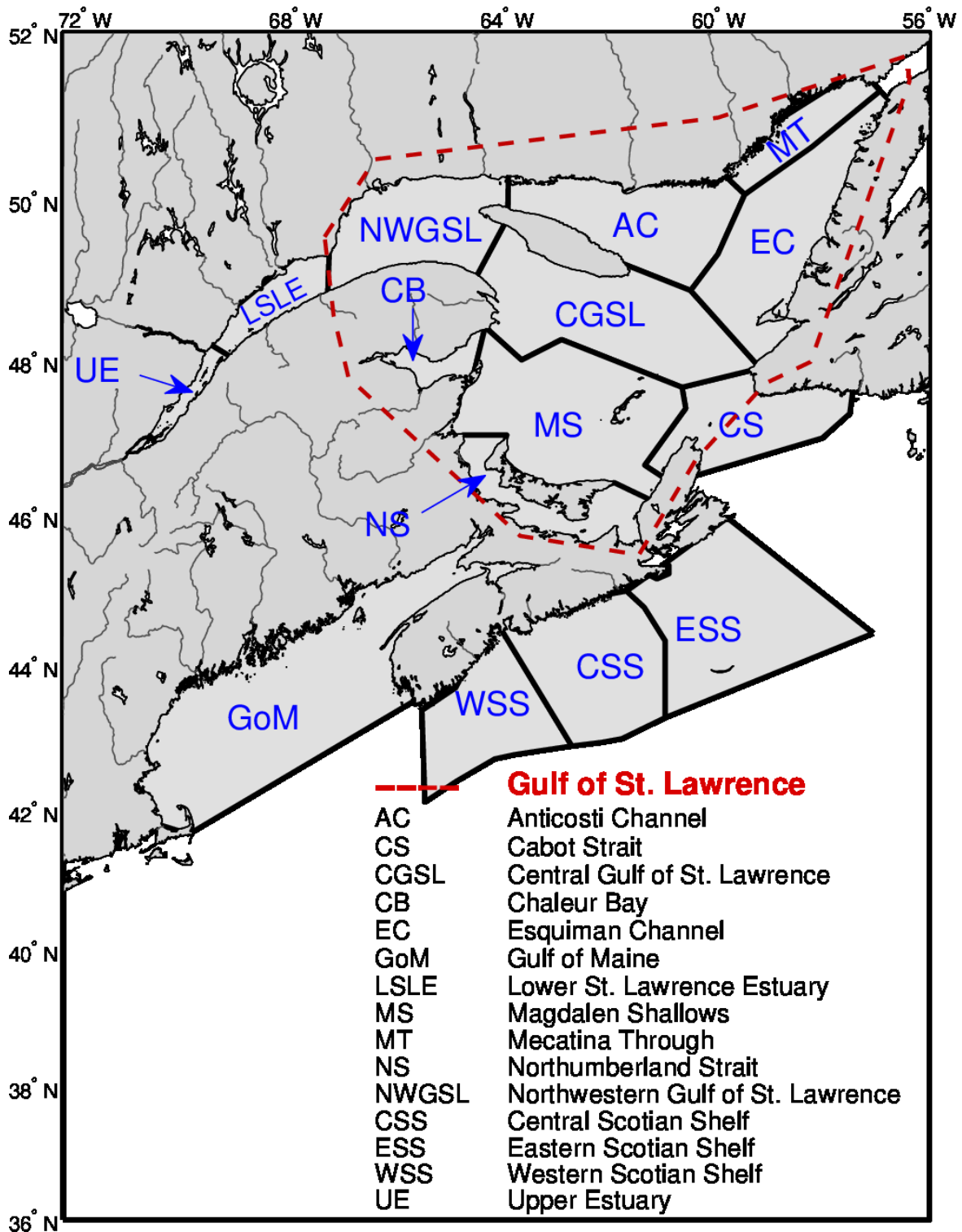


Figure 23. Regions used for the trend analysis in the Gulf of St. Lawrence (red box) and seasonal changes.

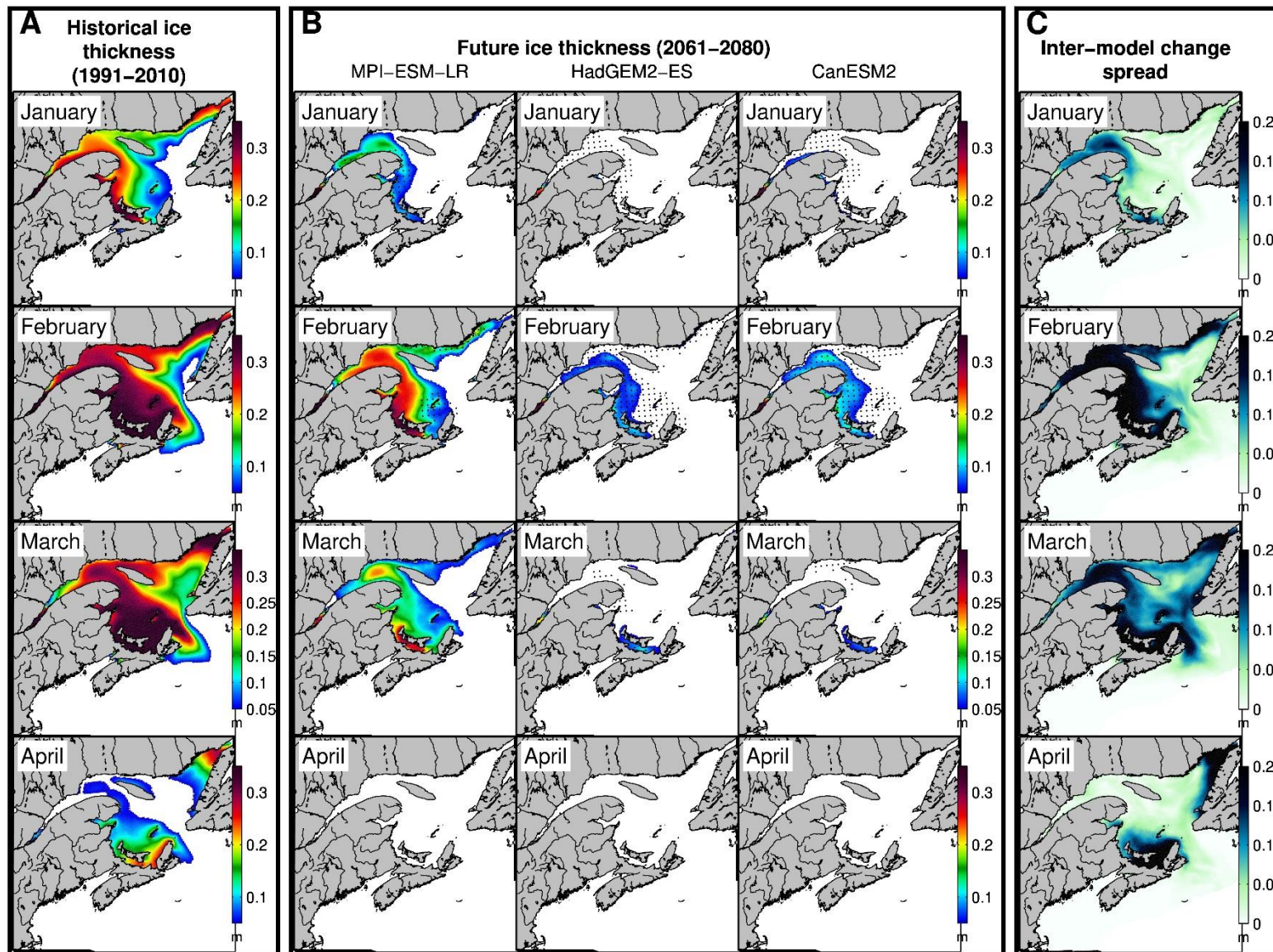


Figure 24. A) Ensemble mean sea-ice thickness (m) over the 1991-2010 period for the simulations forced with MPI-ESM-LR, HadGEM2-ES, and CanESM2 under the RCP 8.5 scenario, B) Mean sea-ice thickness over the 2061-2080 period for each simulation, and C) inter-model change spread in mean sea-ice thickness. In panel B), the dots represent the area where the future change is greater than three times the standard deviation calculated over the historical period, and where all three simulations agree on the sign of change (positive or negative).

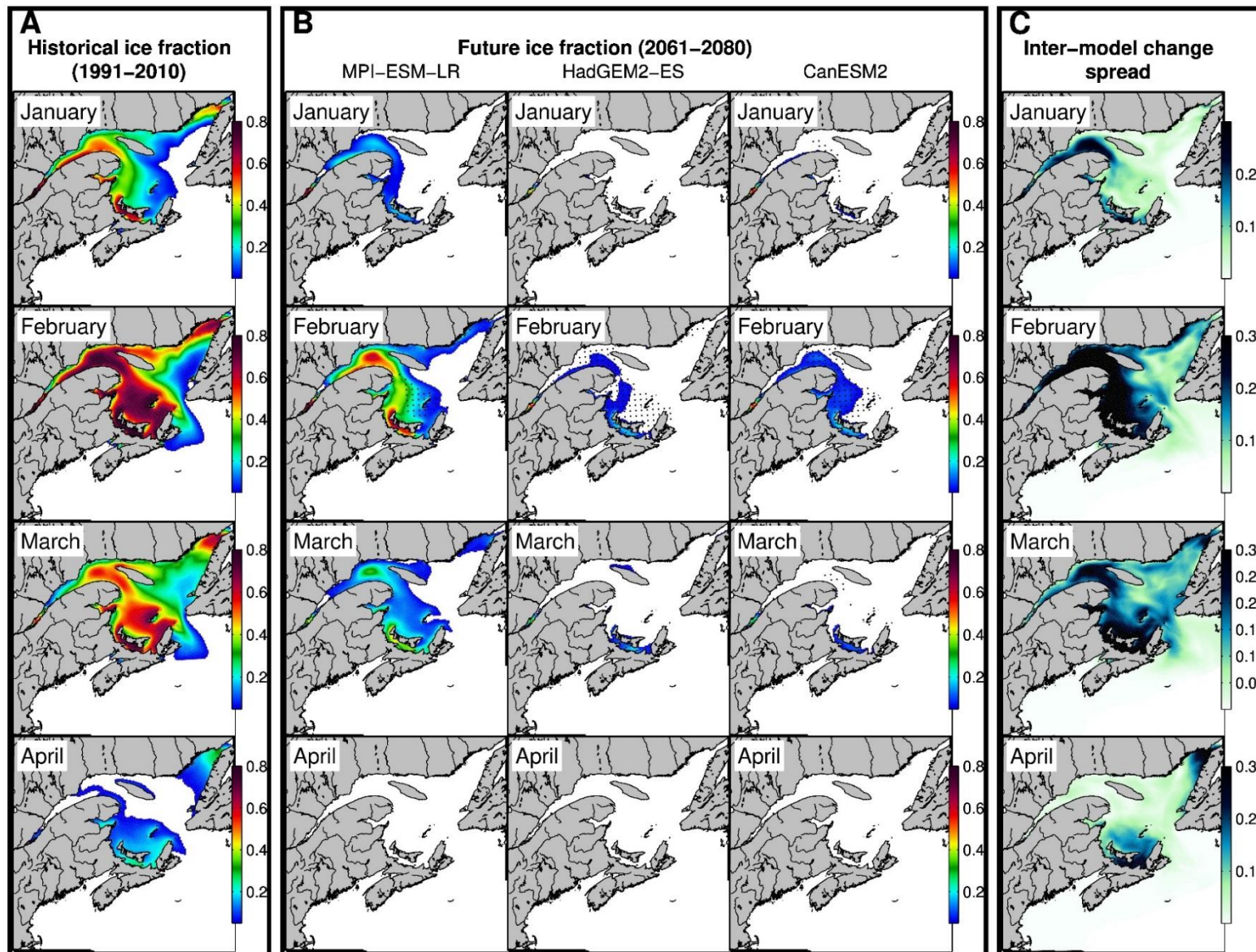


Figure 25. A) Ensemble mean sea-ice fraction over the 1991–2010 period for the simulations forced with MPI-ESM-LR, HadGEM2-ES, and CanESM2 under the RCP 8.5 scenario, B) Mean sea-ice fraction over the 2061–2080 period for each simulation, and C) inter-model change spread. In panel B), the dots represent the area where the future change is greater than three times the standard deviation calculated over the historical period, and where all three simulations agree on the sign of change (positive or negative).

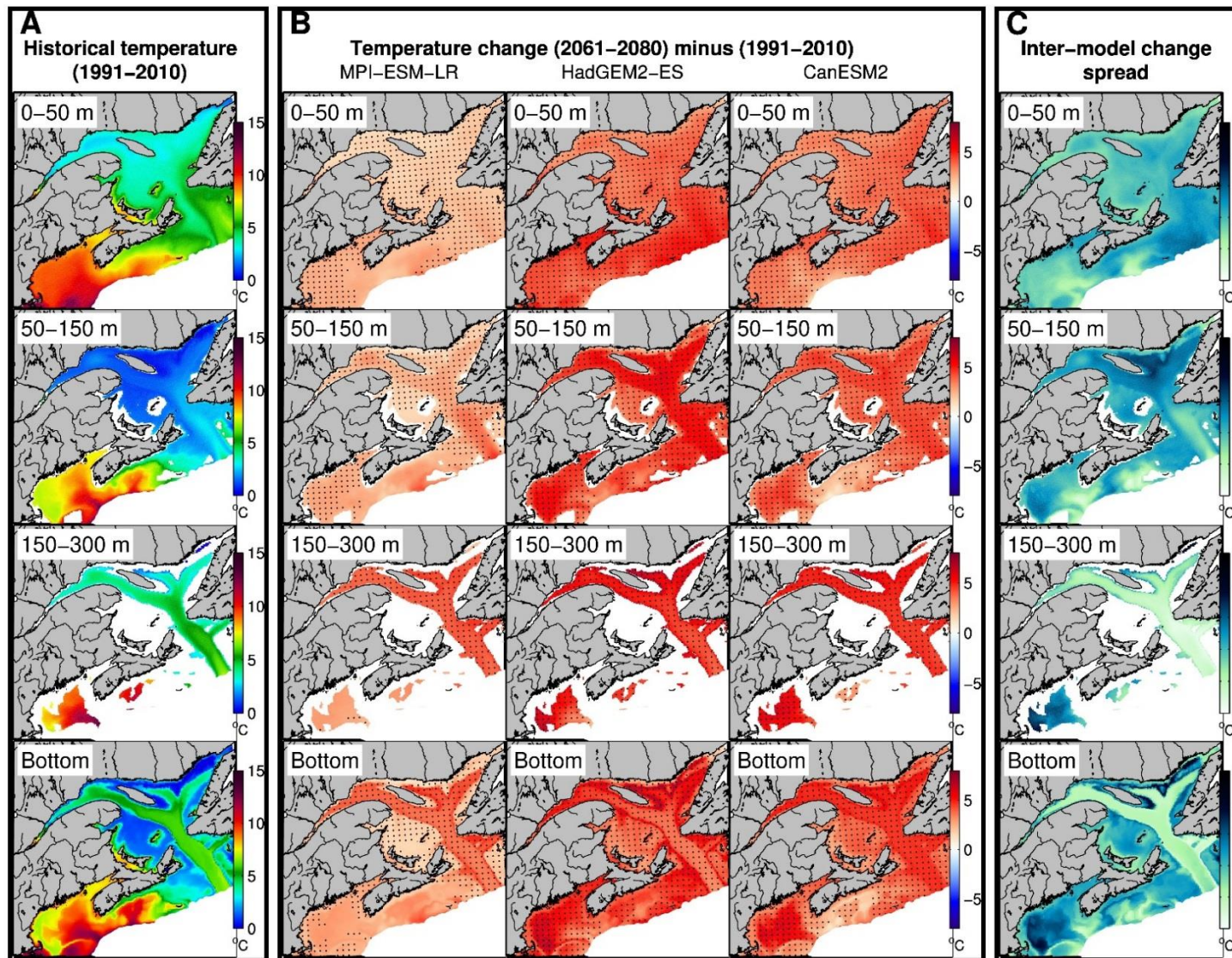


Figure 26. A) Ensemble mean water temperature ($^{\circ}\text{C}$) over the 1991–2010 period at four depth intervals (0–50 m, 50–150 m, 150–300 m, and bottom) for the simulations forced with MPI-ESM-LR, HadGEM2-ES, and CanESM2 under the RCP 8.5 scenario, B) Bidecadal temperature change (2061–2080 average minus 1991–2010 average) for each simulation, and C) inter-model change spread. In panel B), the dots represent the area where the future change is greater than three times the standard deviation calculated over the historical period, and where all three simulations agree on the sign of change (positive or negative).

Mean temperature in the Gulf of St. Lawrence

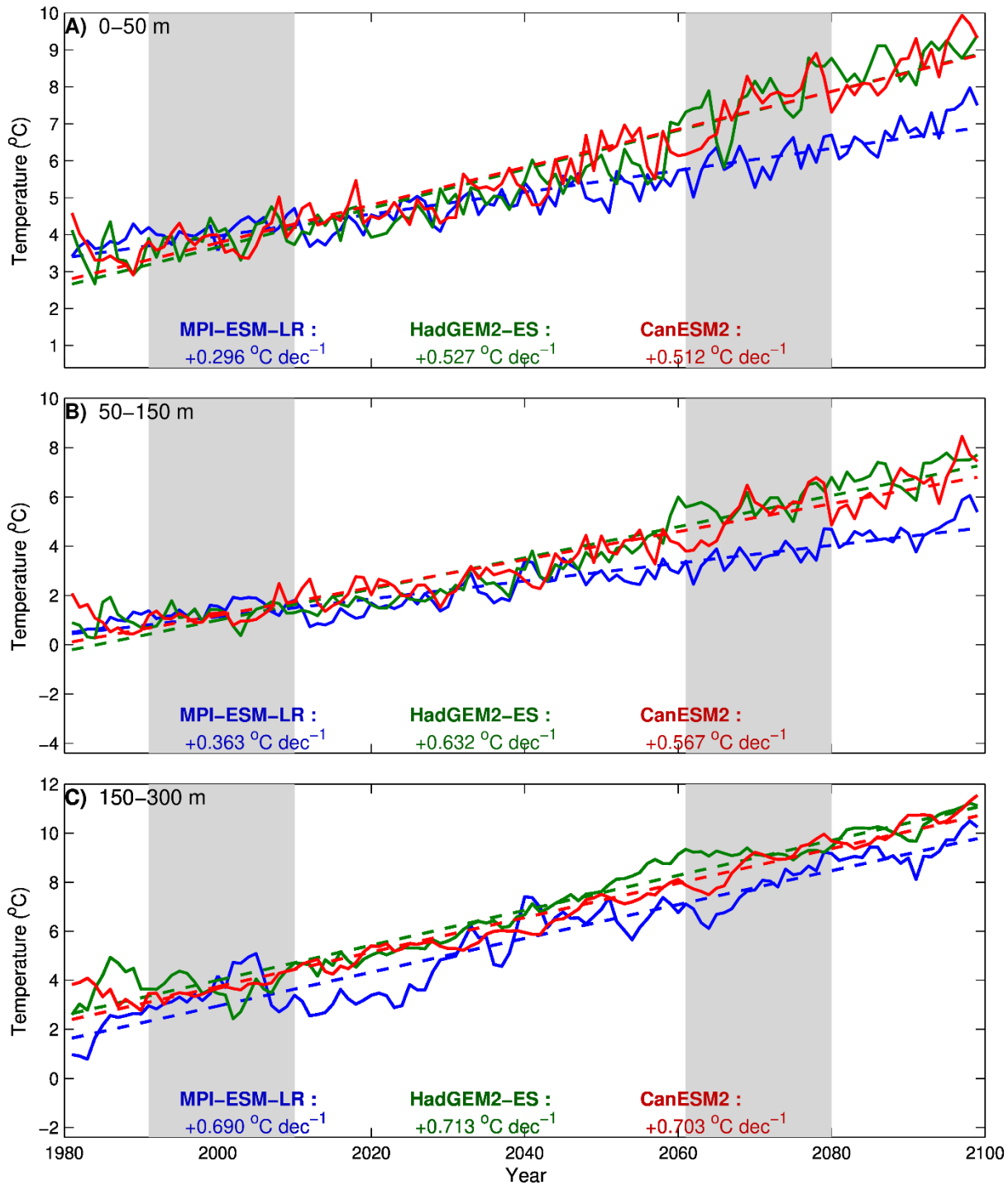


Figure 27. Gulf of St. Lawrence annual mean water temperature ($^{\circ}\text{C}$) at three depth intervals (0–50 m, 50–150 m and 150–300 m), along with the trend (dashed lines, $^{\circ}\text{C}$ per decade) calculated from 1980 to 2099 for the simulations forced with MPI-ESM-LR, HadGEM2-ES, and CanESM2 under the RCP 8.5 scenario. The gray areas cover the historical and future time periods represented in the maps (Figure 26).

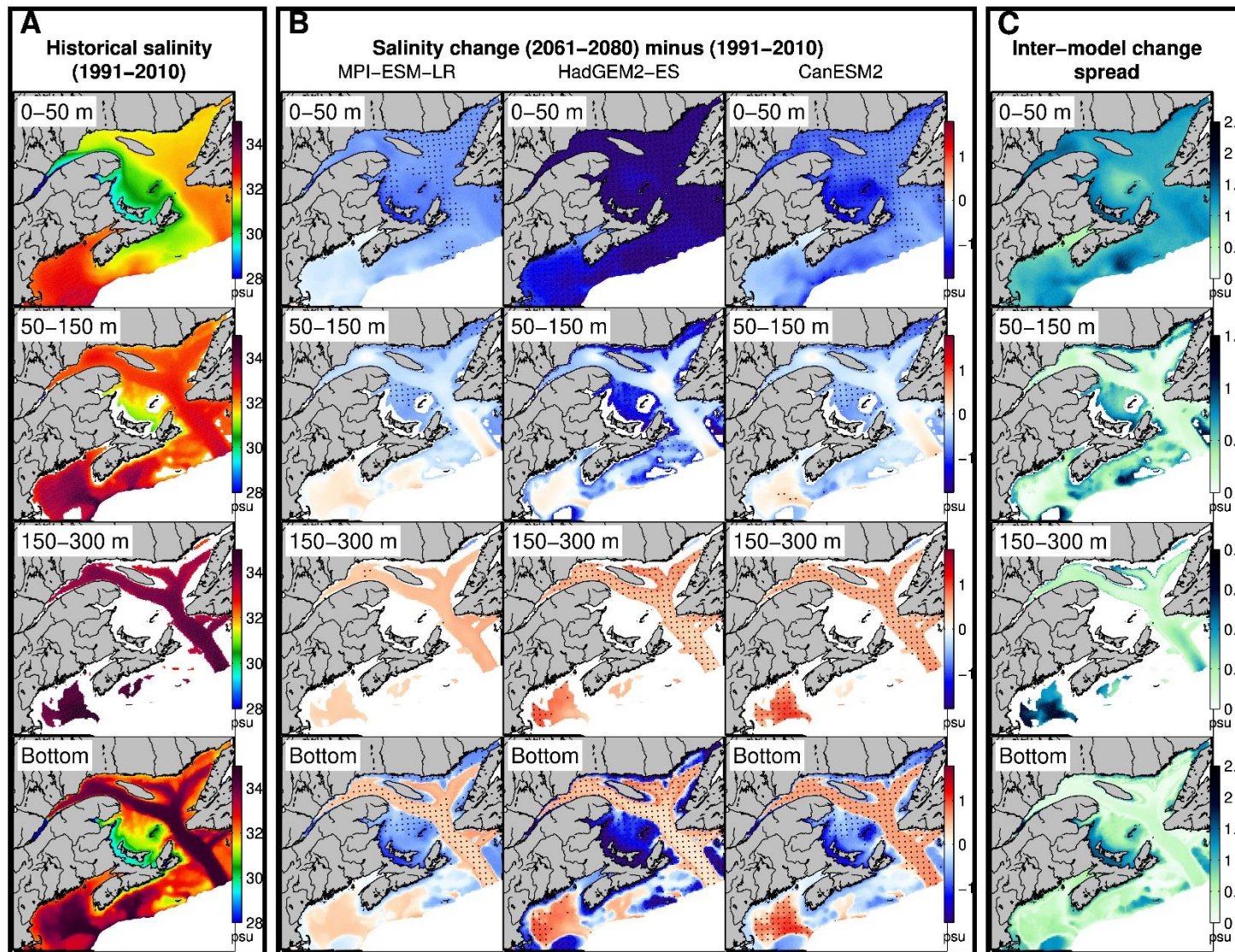


Figure 28. A) Ensemble mean water salinity (psu) over the 1991–2010 period at four depth intervals (0–50 m, 50–150 m, 150–300 m, and bottom) for the simulations forced with MPI-ESM-LR, HadGEM2-ES, and CanESM2 under the RCP 8.5 scenario, B) Bidecadal salinity change (2061–2080 average minus 1991–2010 average) for each simulation, and C) inter-model change spread. In panel B), the dots represent the area where the future change is greater than three times the standard deviation calculated over the historical period, and where all three simulations agree on the sign of change (positive or negative).

Mean salinity in the Gulf of St. Lawrence

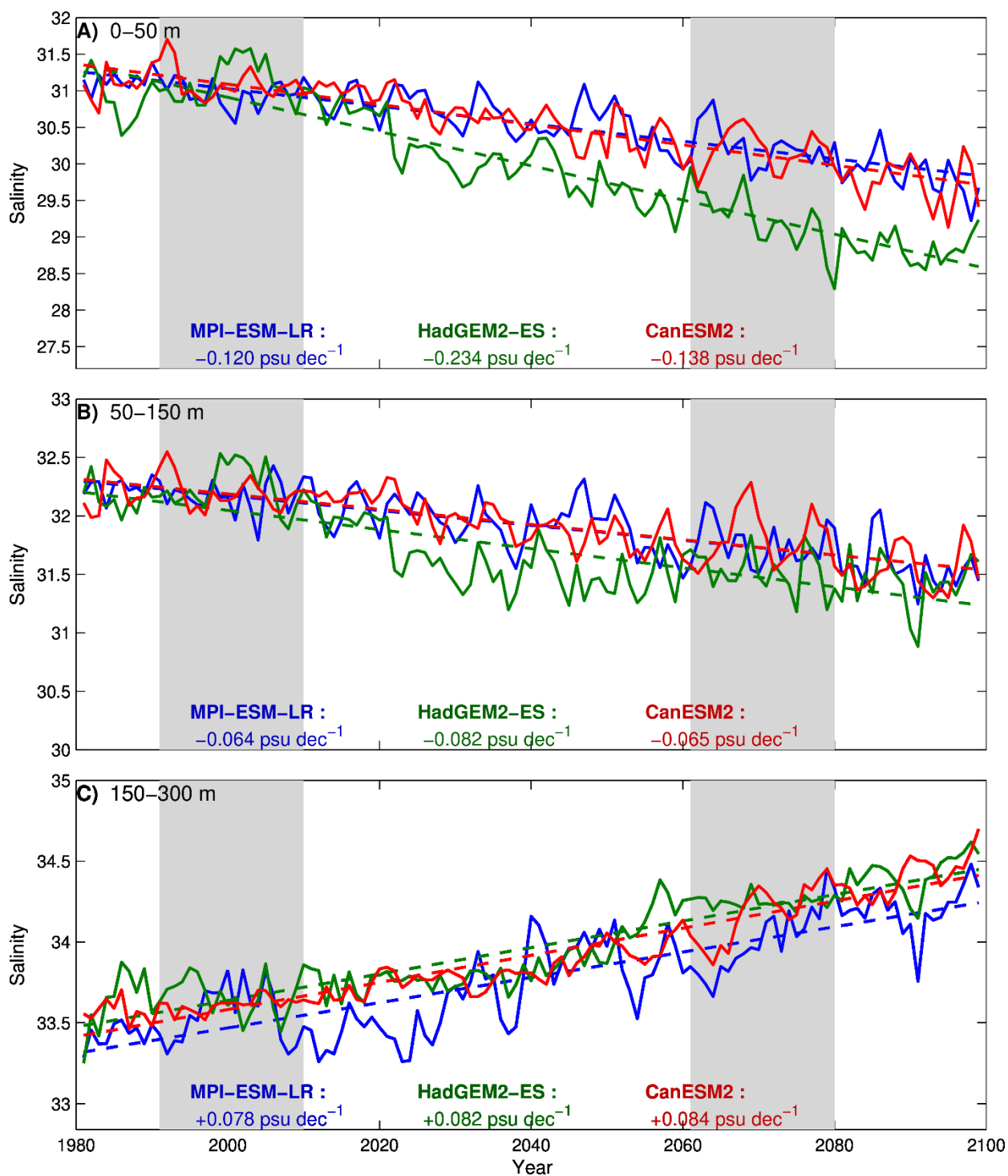


Figure 29. Gulf of St. Lawrence annual mean water salinity (psu) at three depth intervals (0–50 m, 50–150 m and 150–300 m), along with the trend (dashed lines, psu per decade) calculated from 1980 to 2099 for the simulations forced with MPI-ESM-LR, HadGEM2-ES, and CanESM2 under the RCP 8.5 scenario. The gray areas cover the historical and future time periods represented in the maps and in the annual cycle (Figures 28, 30 and 31).

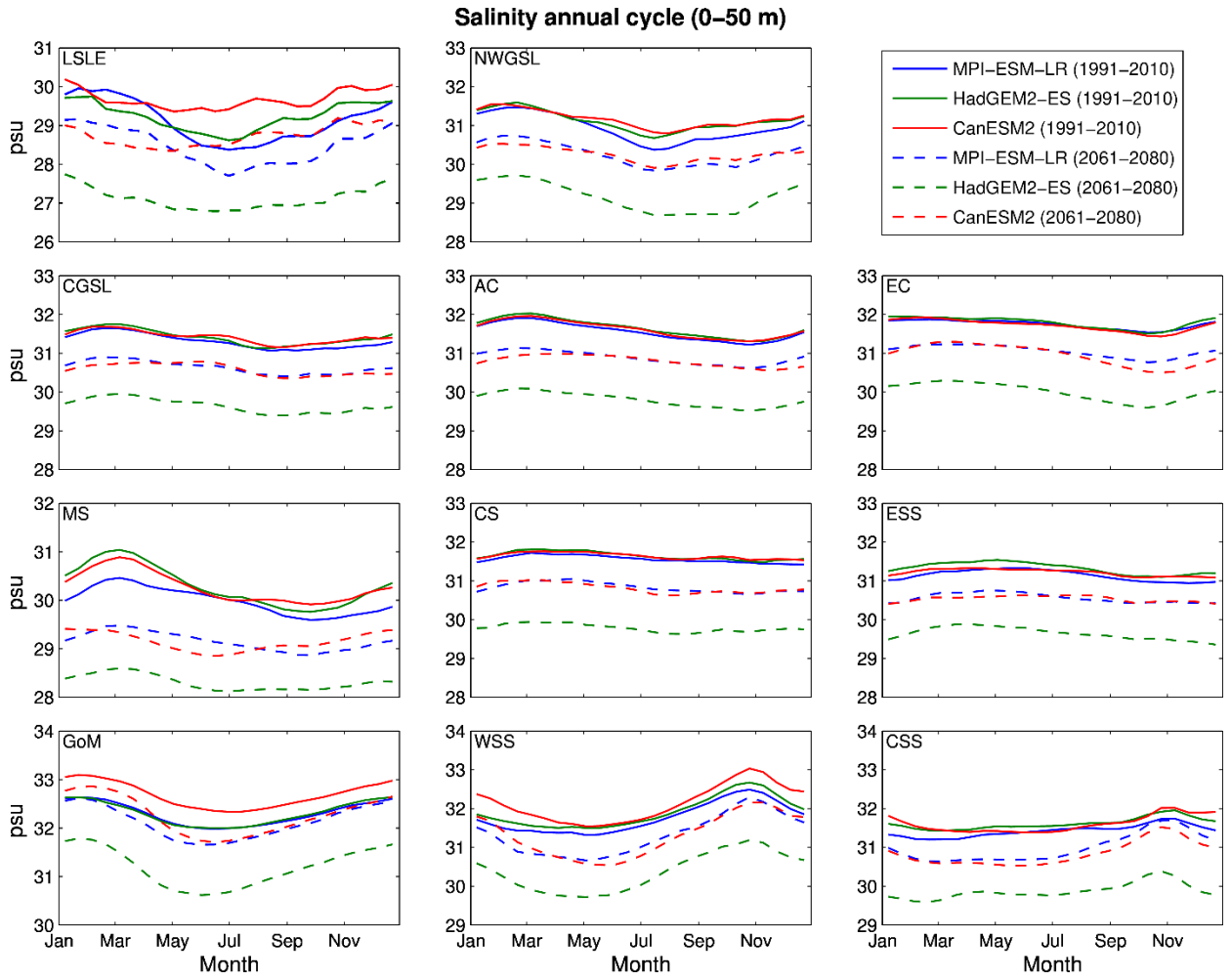


Figure 30. Mean salinity annual cycle inside the zones defined in Figure 23 at the 0-50 m depth interval, for the simulations forced with MPI-ESM-LR, HadGEM2-ES, and CanESM2 under the RCP 8.5 scenario. The annual cycle is defined as the average of each step (25 per year) for the 20 years of the historical (solid lines) and the future periods (dashed lines).

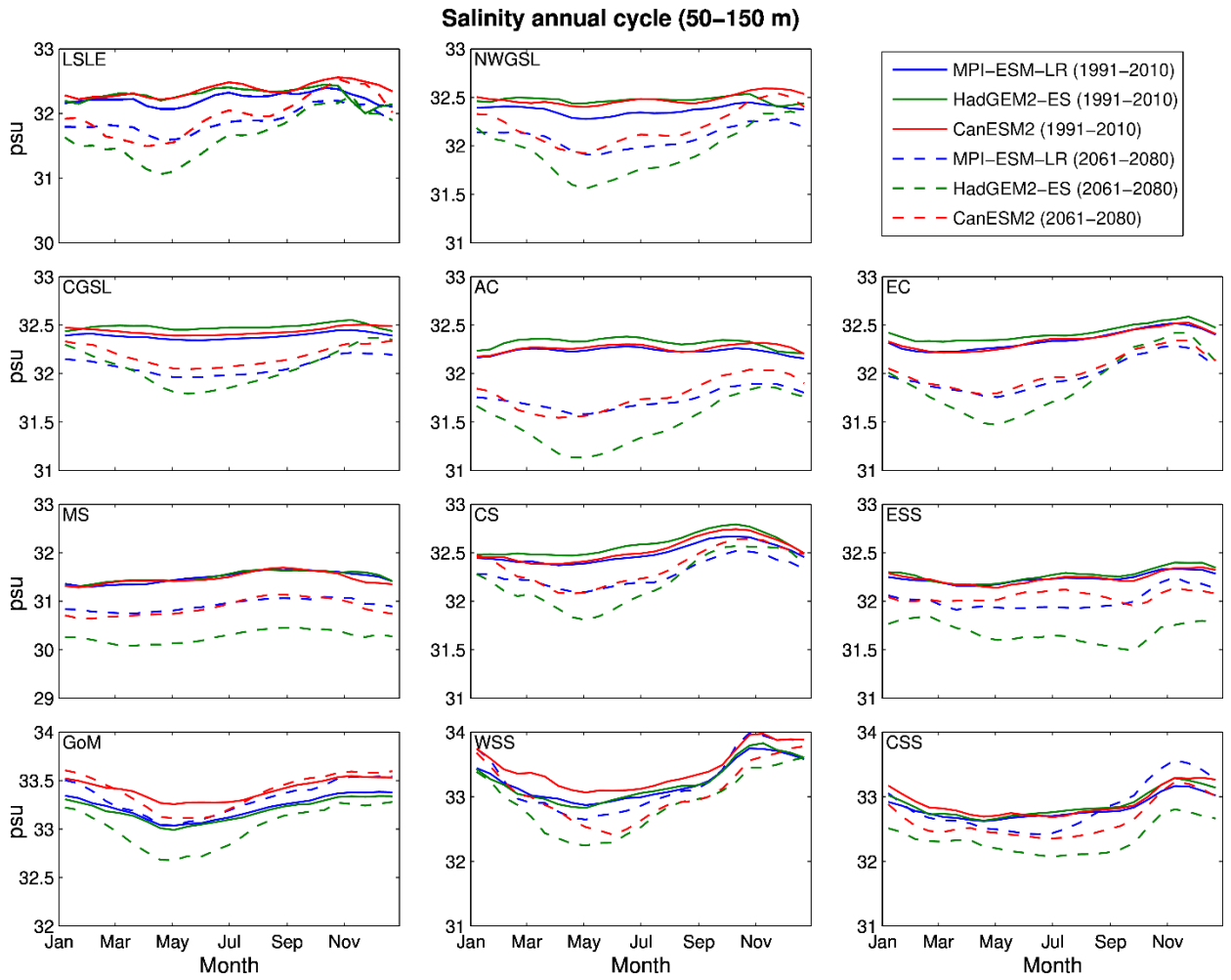


Figure 31. Mean salinity annual cycle inside the zones defined in Figure 23 at the 50-150 m depth interval, for the simulations forced with MPI-ESM-LR, HadGEM2-ES, and CanESM2 under the RCP 8.5 scenario. The annual cycle is defined as the average of each step (25 per year) for the 20 years of the historical (solid lines) and the future periods (dashed lines).

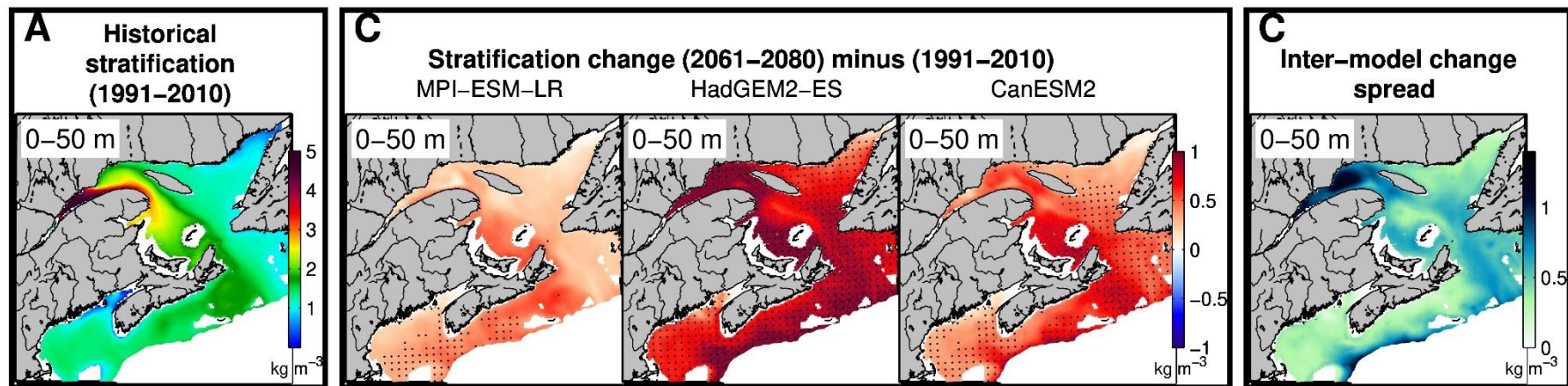


Figure 32. A) Ensemble mean stratification (kg m^{-3}) over the 1991-2010 period at the 0-50 m depth interval for the simulations forced with MPI-ESM-LR, HadGEM2-ES and CanESM2 under the RCP 8.5 scenario, B) Bidecadal stratification change (2061-2080 average minus 1991-2010 average) for each simulation, and C) inter-model change spread. In panel B), the dots represent the area where the future change is greater than three times the standard deviation calculated over the historical period, and where all three simulations agree on the sign of change (positive or negative).

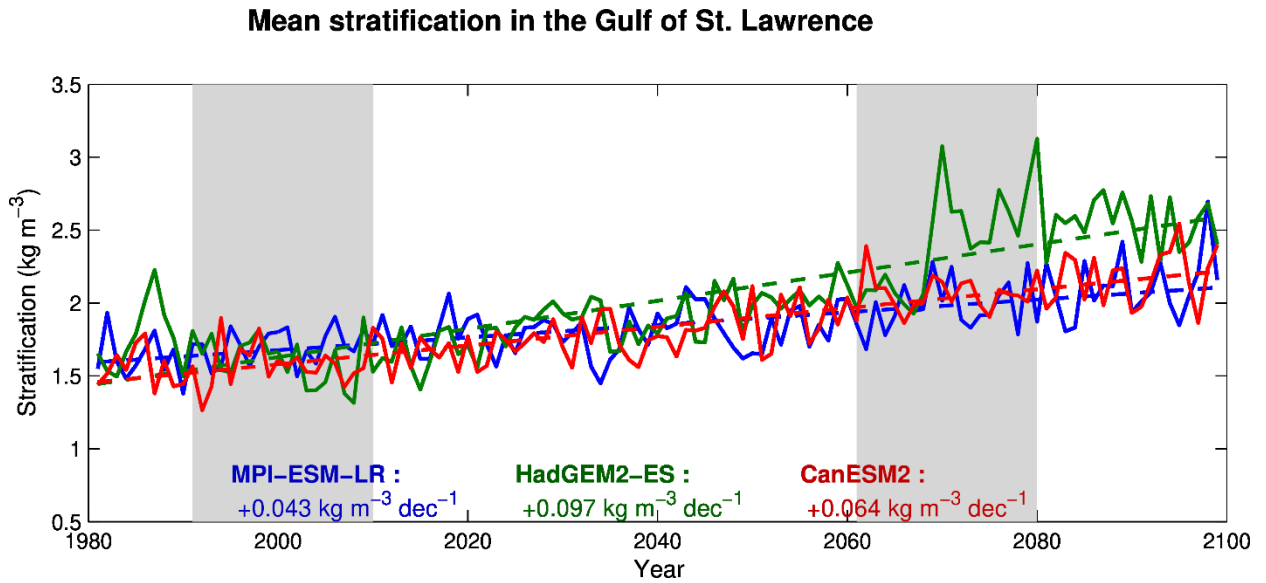


Figure 33. Annual mean stratification in the Gulf of St. Lawrence at the 0-50 m depth interval, along with the trend (dashed lines, kg m^{-3} per decade), calculated from 1980-2099 for the simulations forced with MPI-ESM-LR, HadGEM2-ES, and CanESM2 under the RCP 8.5 scenario. The gray areas cover the historical and future time periods represented in the maps and in the annual cycle (Figures 32 and 34).

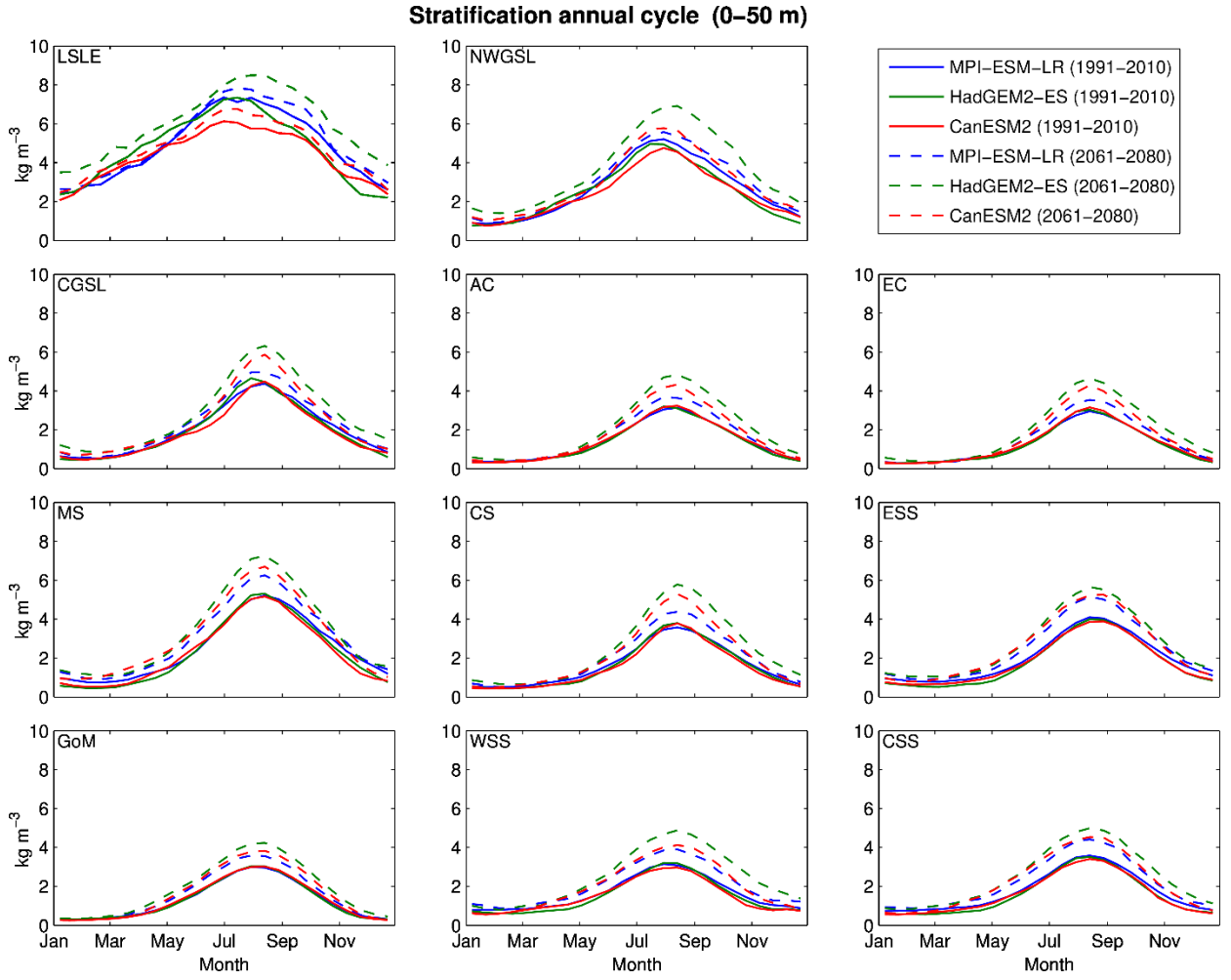


Figure 34. Mean stratification ($\sigma_{50m} - \sigma_{0m}$) annual cycle inside the zones defined in Figure 23 at the 0-50 m depth interval, for the simulations forced with MPI-ESM-LR, HadGEM2-ES, and CanESM2 under the RCP 8.5 scenario. The annual cycle is defined as the average of each step (25 per year) for the 20 years of the historical (solid lines) and the future periods (dashed lines).

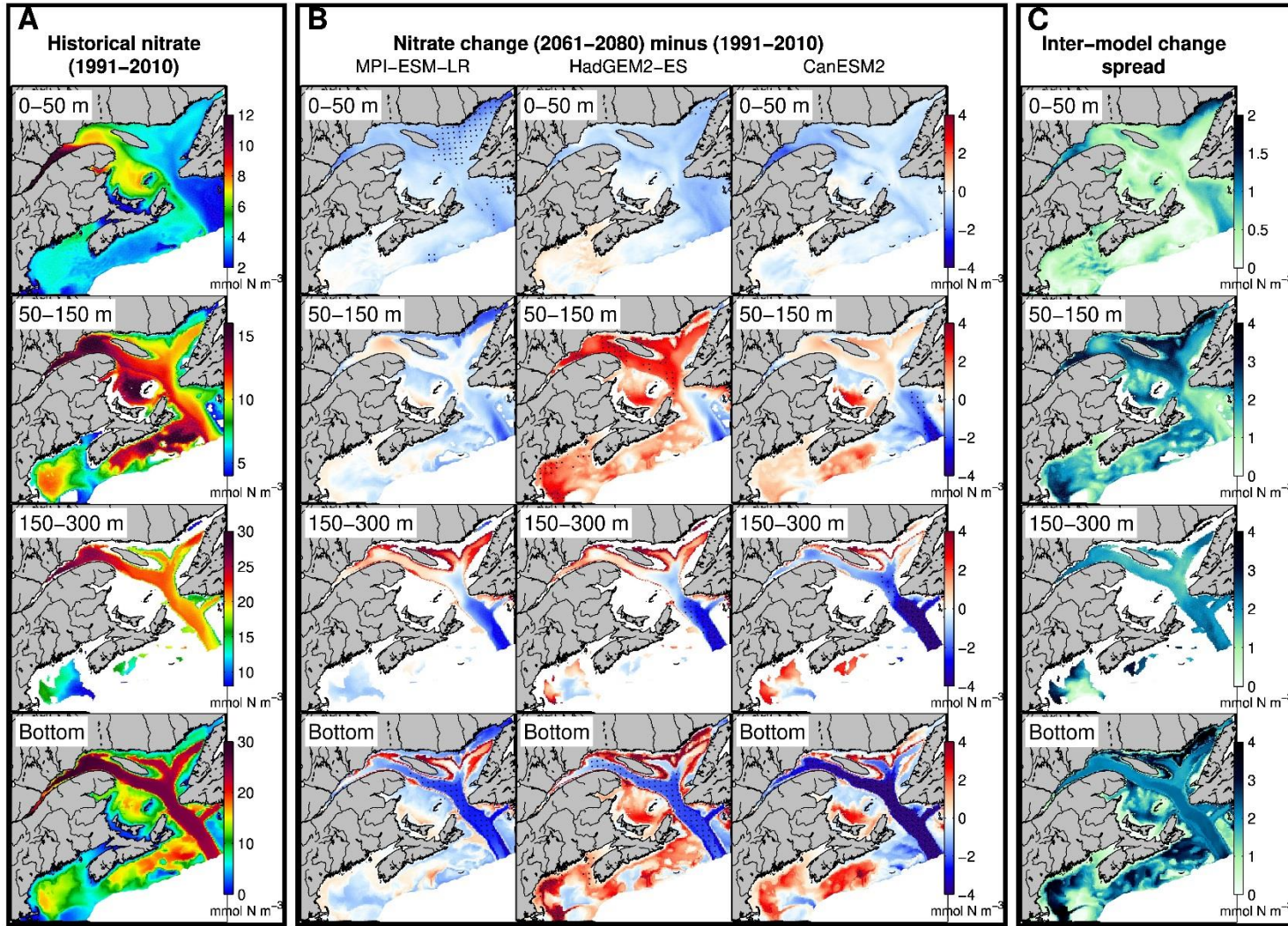


Figure 35. A) Ensemble mean nitrate concentration (mmol N m^{-3}) over the 1991–2010 period at four depth intervals (0–50 m, 50–150 m, 150–300 m, and bottom) for the simulations forced with MPI-ESM-LR, HadGEM2-ES, and CanESM2 under the RCP 8.5 scenario, B) Bidecadal nitrate concentration change (2061–2080 average minus 1991–2010 average) for each simulation, and C) inter-model change spread. Note that the color scale is sometimes different for the different depth layers. In panel B), the dots represent the area where the future change is greater than three times the standard deviation calculated over the historical period, and where all three simulations agree on the sign of change (positive or negative).

Mean nitrate in the Gulf of St. Lawrence

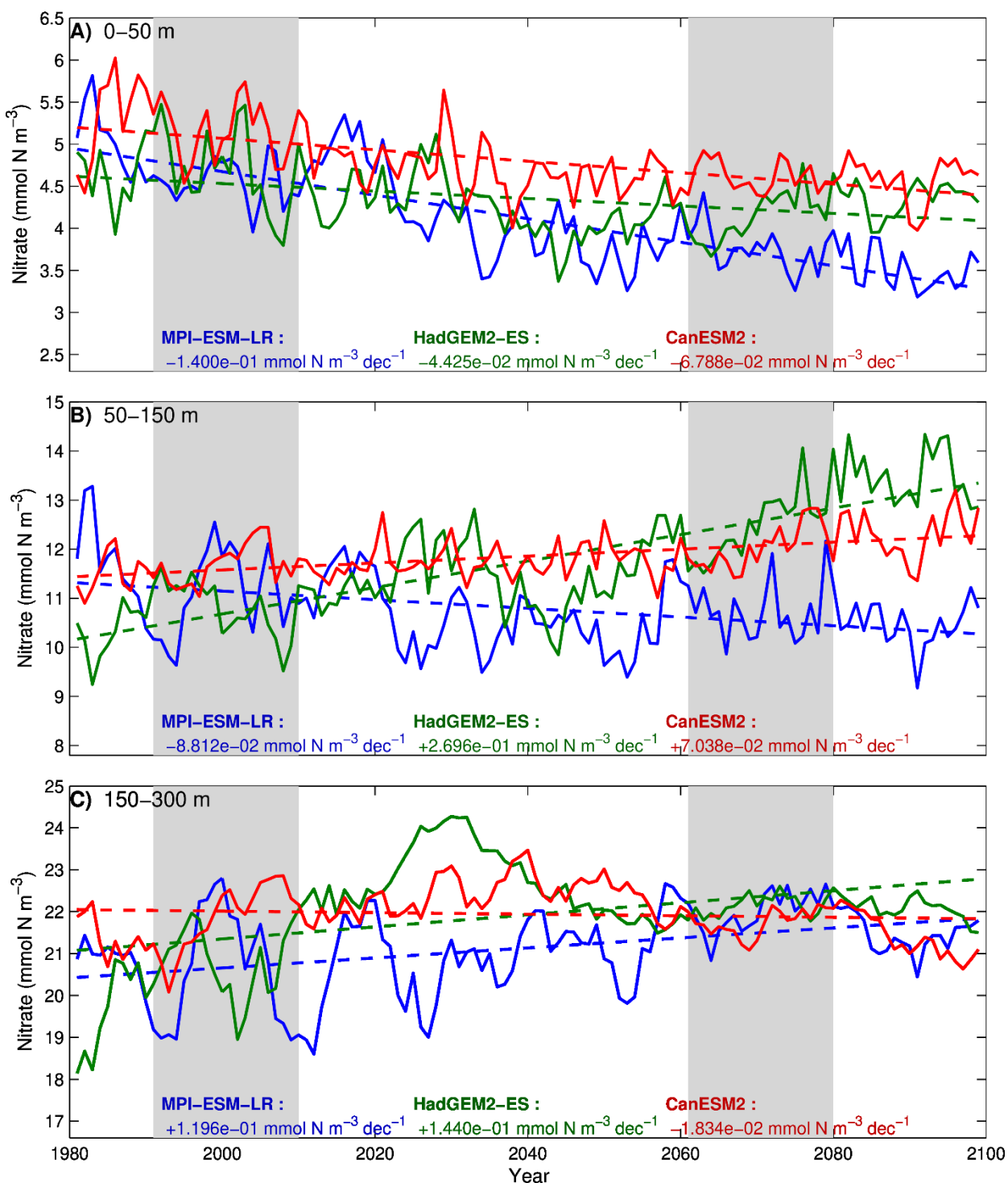


Figure 36. Gulf of St. Lawrence annual mean nitrate concentration at three depth intervals (0–50 m, 50–150 m and 150–300 m), along with the trend (dashed lines, mmol N m^{-3} per decade) calculated from 1980–2099 for simulations forced with MPI-ESM-LR, HadGEM2-ES, and CanESM2 under the RCP 8.5 scenario. The gray areas cover the historical and future time periods represented in the maps and in the annual cycle (Figures 35 and 37).

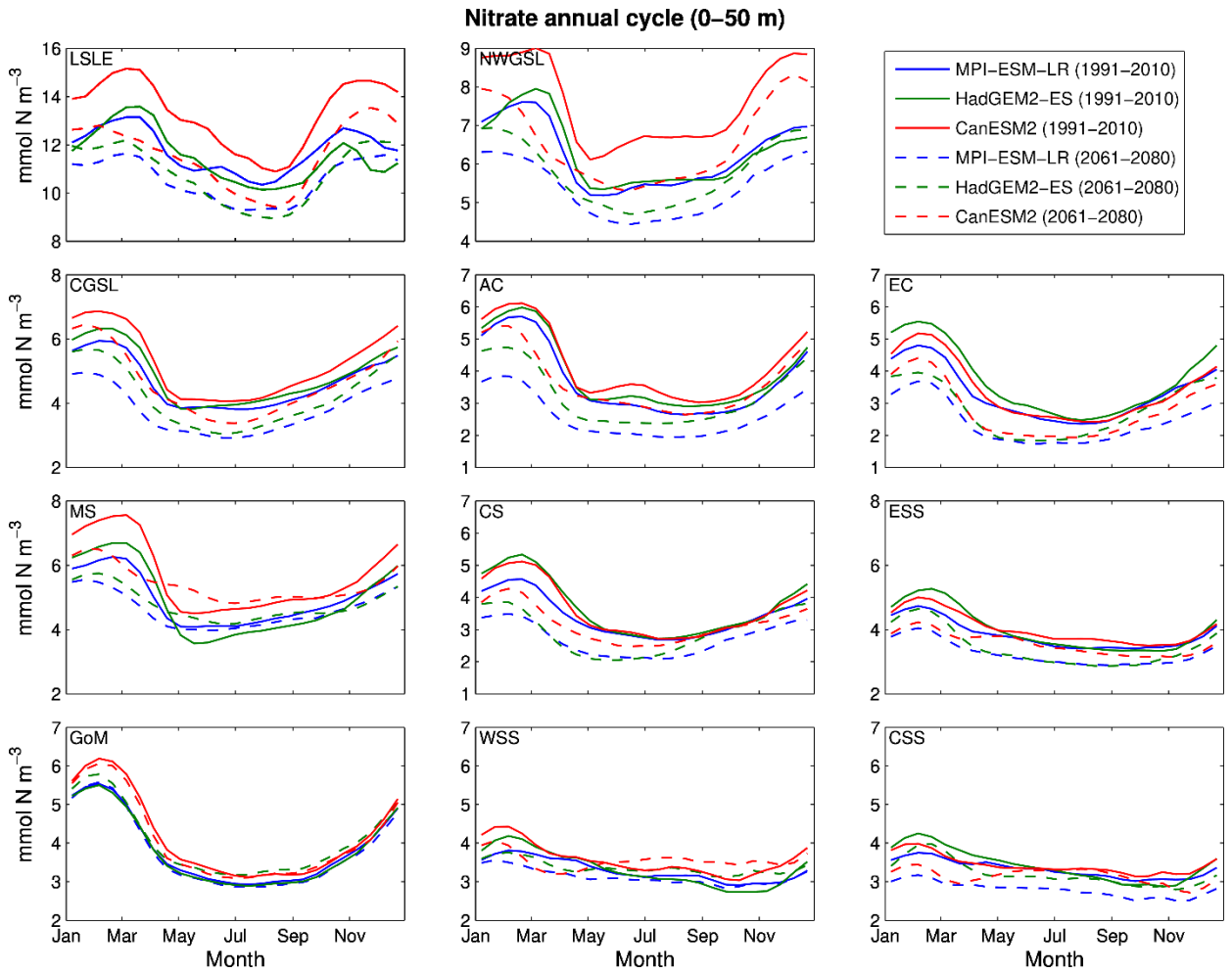


Figure 37. Mean nitrate concentration annual cycle inside the zones defined in Figure 23 at the 0–50 m depth interval, for the simulations forced with MPI-ESM-LR, HadGEM2-ES and CanESM2 under the RCP 8.5 scenario. The annual cycle is defined as the average of each step (25 per year) for the 20 years of the historical (solid lines) and the future periods (dashed lines).

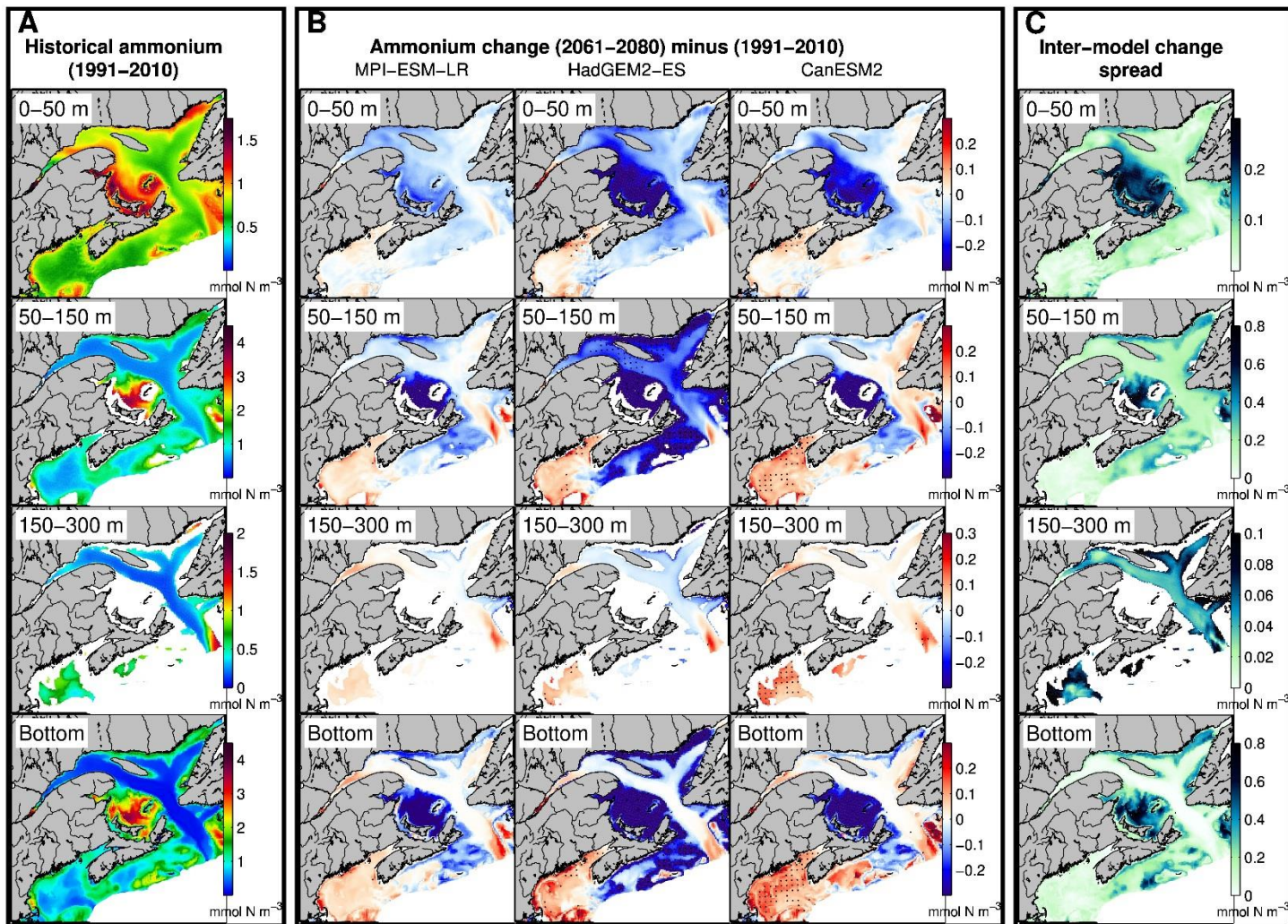


Figure 38. A) Ensemble mean ammonium concentration (mmol N m⁻³) over the 1991–2010 period at four depth intervals (0–50 m, 50–150 m, 150–300 m, and bottom) for the simulations forced with MPI-ESM-LR, HadGEM2-ES, and CanESM2 under the RCP 8.5 scenario, B) Bidecadal ammonium concentration change (2061–2080 average minus 1991–2010 average) for each simulation, and C) inter-model change spread. Note that the color scale is sometimes different for the different depth layers. In panel B), the dots represent the area where the future change is greater than three times the standard deviation calculated over the historical period, and where all three simulations agree on the sign of change (positive or negative).

Mean ammonium in the Gulf of St. Lawrence

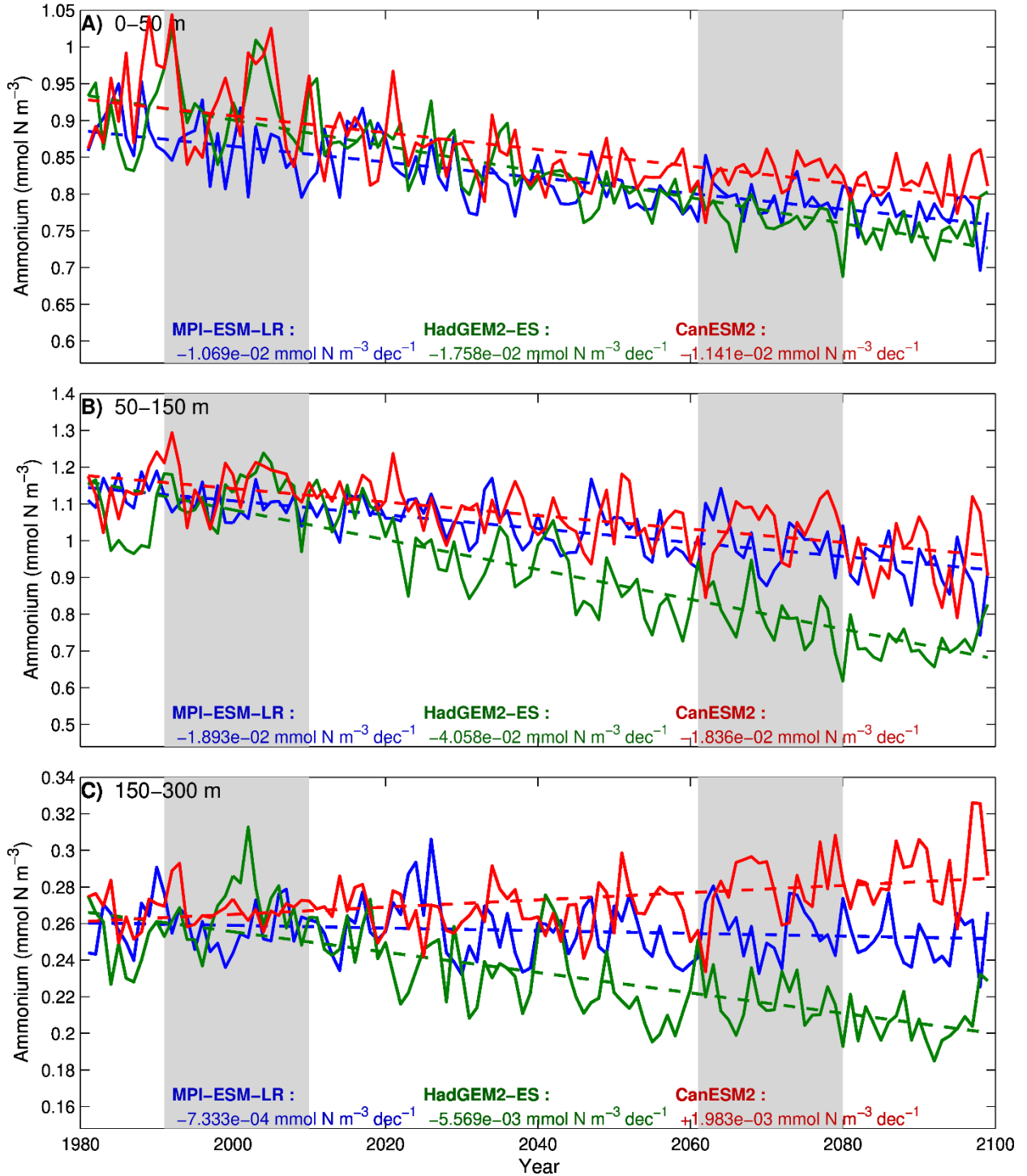


Figure 39. Gulf of St. Lawrence annual mean ammonium concentration at three depth intervals (0-50 m, 50-150 m and 150-300 m), along with the trend (dashed lines, mmol N m⁻³ per decade) calculated from 1980-2099 for the simulations forced with MPI-ESM-LR, HadGEM2-ES, and CanESM2 under the RCP 8.5 scenario. The gray areas cover the historical and future time periods represented in the maps and in the annual cycle (Figures 38 and 40).

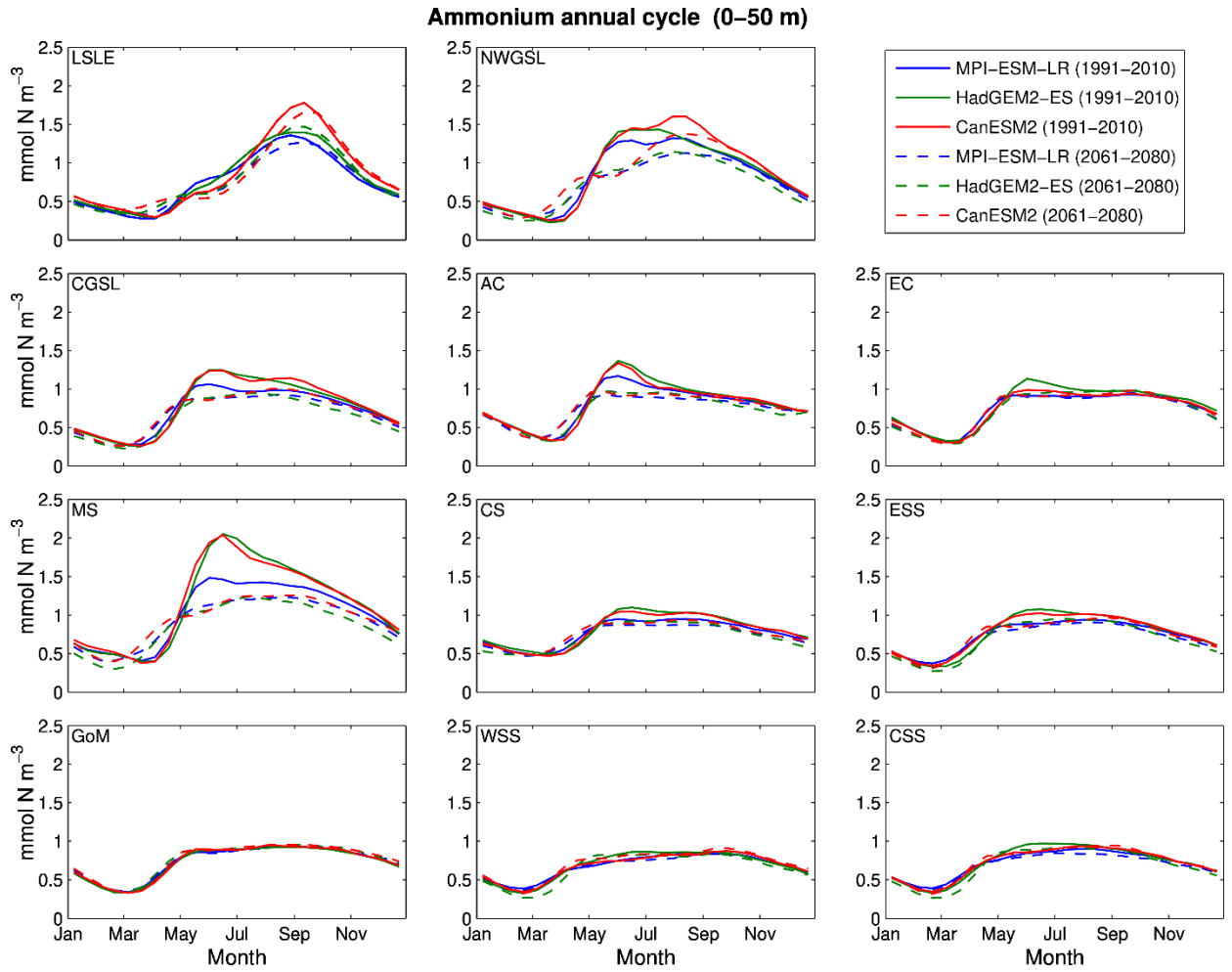


Figure 40. Mean ammonium concentration annual cycle inside the zones defined in Figure 23 at the 0–50 depth interval, for the simulations forced with MPI-ESM-LR, HadGEM2-ES, and CanESM2 under the RCP 8.5 scenario. The annual cycle is defined as the average of each step (25 per year) for the 20 years of the historical (solid lines) and the future periods (dashed lines).

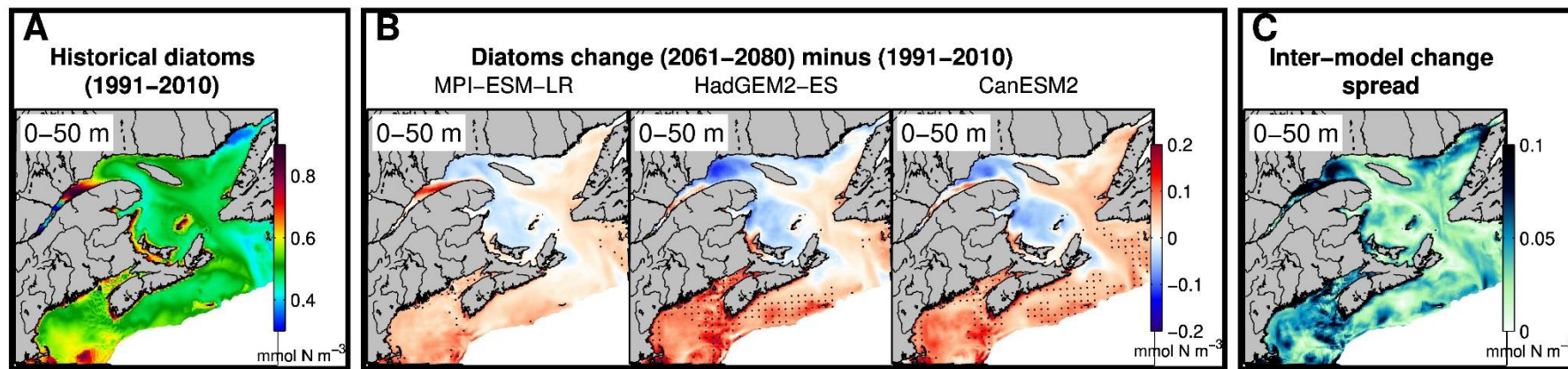


Figure 41. A) Ensemble mean annual diatom-N concentration (mmol N m^{-3}) over the 1991-2010 period at the 0-50 m depth interval, for the simulations forced with MPI-ESM-LR, HadGEM2-ES, and CanESM2 under the RCP 8.5 scenario, B) Bidecadal diatom-N concentration change (2061-2080 average minus 1991-2010 average) for each simulation, and C) inter-model change spread. In panel B) the dots represent the area where the change is greater than three times the historical standard deviation over the historical period and where all three simulations agree on the direction of change (increase or decrease).

Mean diatom concentration in the Gulf of St. Lawrence

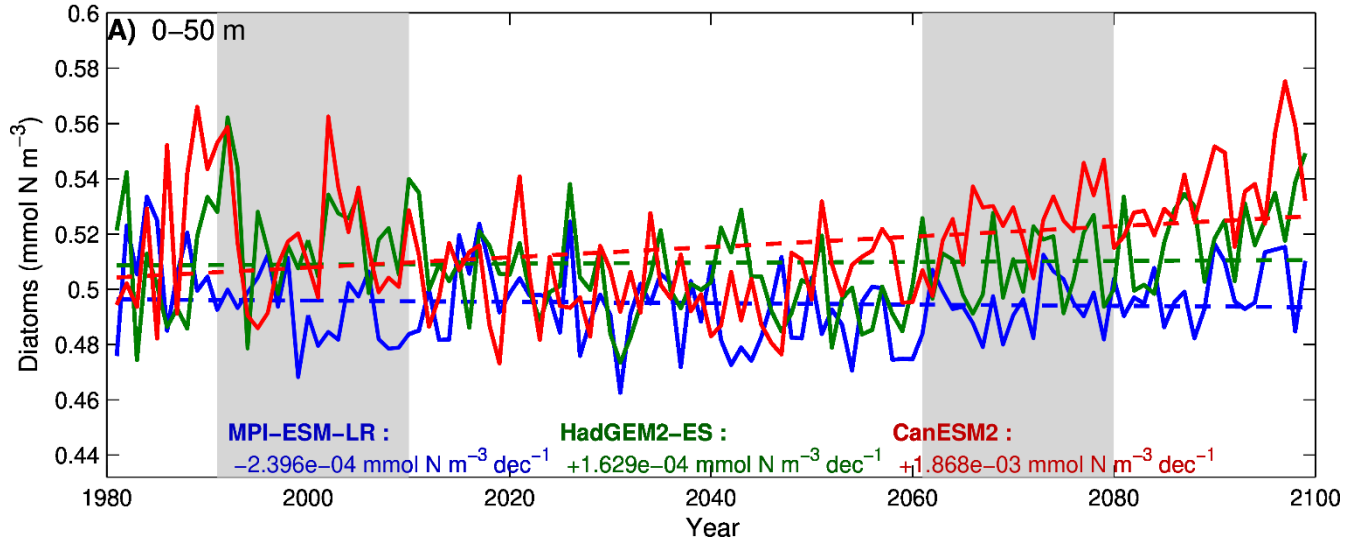


Figure 42. Gulf of St. Lawrence annual mean diatom-N concentration at the 0-50 m depth interval, along with the trend (dashed lines, mmol N m^{-3} per decade) calculated from 1980-2099 for the simulations forced with MPI-ESM-LR, HadGEM2-ES, and CanESM2 under the RCP 8.5 scenario. The gray areas cover the historical and future time periods represented in the maps (Figure 41).

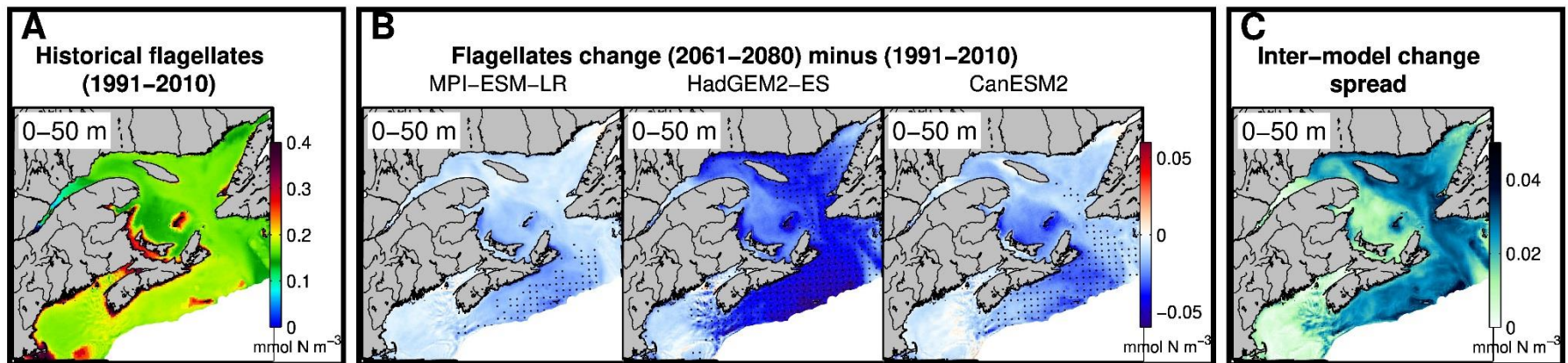


Figure 43. A) Ensemble mean annual flagellate-N concentration (mmol N m⁻³) over the 1991-2010 period at the 0-50 m depth interval for the simulations forced with MPI-ESM-LR, HadGEM2-ES, and CanESM2 under the RCP 8.5 scenario, B) Bidecadal flagellate concentration change (2061-2080 average minus 1991-2010 average) for each simulation, and C) inter-model change spread. In panel B) the dots represent the area where the change is greater than three times the historical standard deviation over the historical period and where all three simulations agree on the direction of change (increase or decrease).

Mean flagellate concentration in the Gulf of St. Lawrence

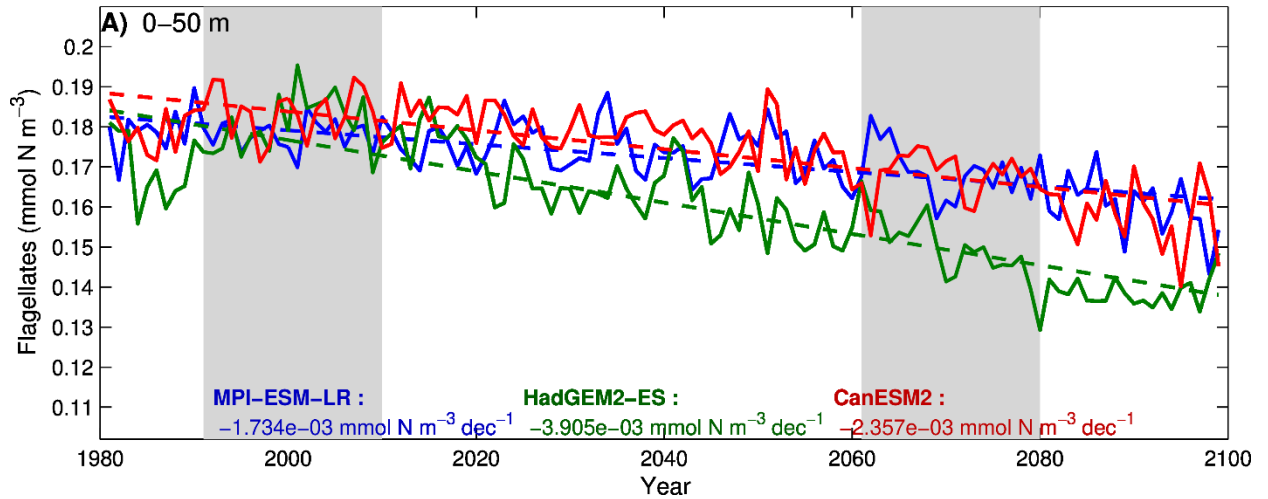


Figure 44. Gulf of St. Lawrence annual mean flagellate-N concentration at the 0-50 m depth interval, along with the trend (dashed lines, mmol N m^{-3} per decade) calculated from 1980-2099 for the simulations forced with MPI-ESM-LR, HadGEM2-ES, and CanESM2) under the RCP 8.5 scenario. The gray areas cover the historical and future time periods represented in the maps (Figure 43).

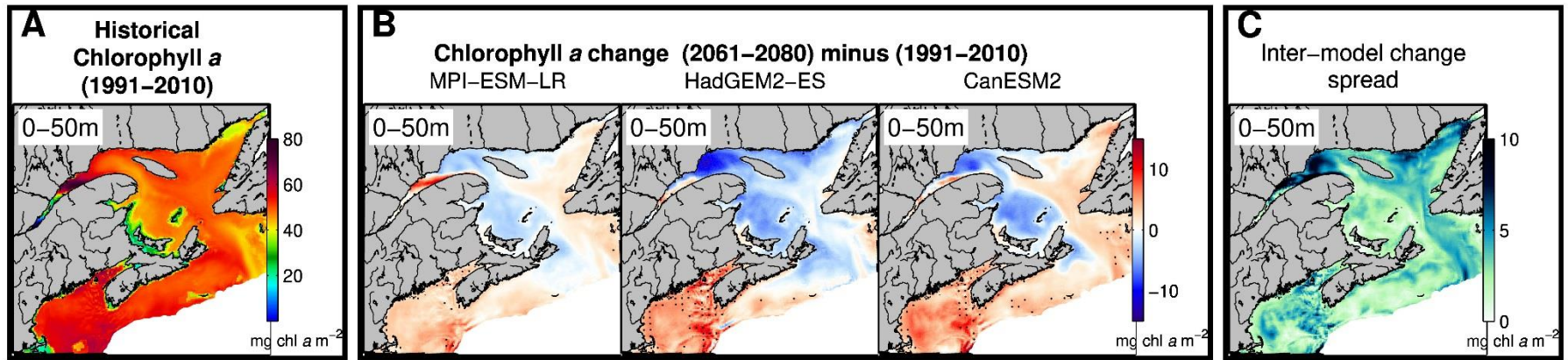


Figure 45. A) Ensemble mean annual chlorophyll *a* biomass (mg chl *a* m⁻²) over the 1991–2010 period at the 0–50 m depth interval for the simulations forced with MPI-ESM-LR, HadGEM2-ES, and CanESM2 under the RCP 8.5 scenario, B) Bidecadal chlorophyll *a* biomass change (2061–2080 average minus 1991–2010 average) for each simulation, and C) inter-model change spread. In panel B) the dots represent the area where the change is greater than three times the historical standard deviation over the historical period and where all three simulations agree on the direction of change (increase or decrease).

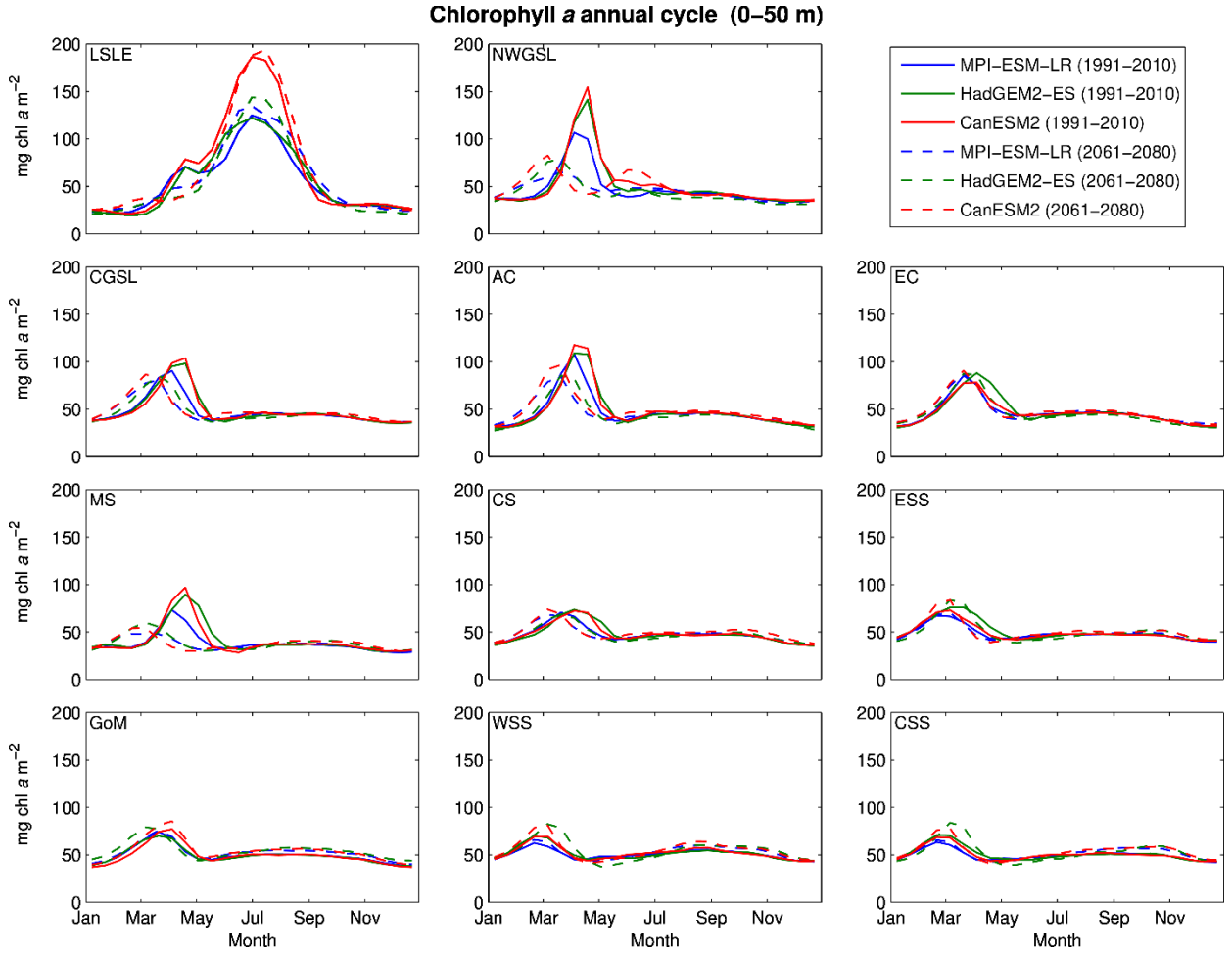


Figure 46. Mean chlorophyll *a* biomass annual cycle inside the zones defined in Figure 23 at the 0–50 m depth interval, for the simulations forced with MPI-ESM-LR, HadGEM2-ES, and CanESM2 under the RCP 8.5 scenario. The annual cycle is defined as the average of each step (25 per year) for the 20 years of the historical (solid lines) and the future periods (dashed lines).

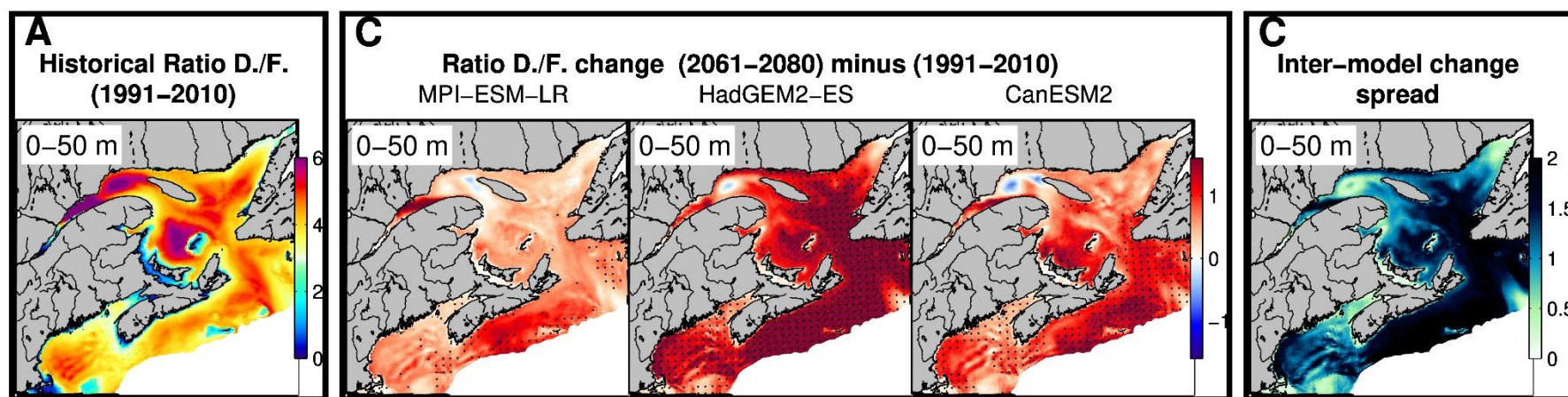


Figure 47. A) Ensemble mean diatom to flagellate ratio (mol N:mol N) over the 1991-2010 period at the 0-50 m depth interval for the simulations forced with MPI-ESM-LR, HadGEM2-ES, and CanESM2 under the RCP 8.5 scenario, B) Bidecadal diatom/flagellate ratio change (2061-2080 average minus 1991-2010 average) for each simulation, and C) inter-model change spread. In panel B) the dots represent the area where the change is greater than three times the historical standard deviation over the historical period and where all three simulations agree on the direction of change (increase or decrease).

Mean diatom to flagellate ratio in the Gulf of St. Lawrence

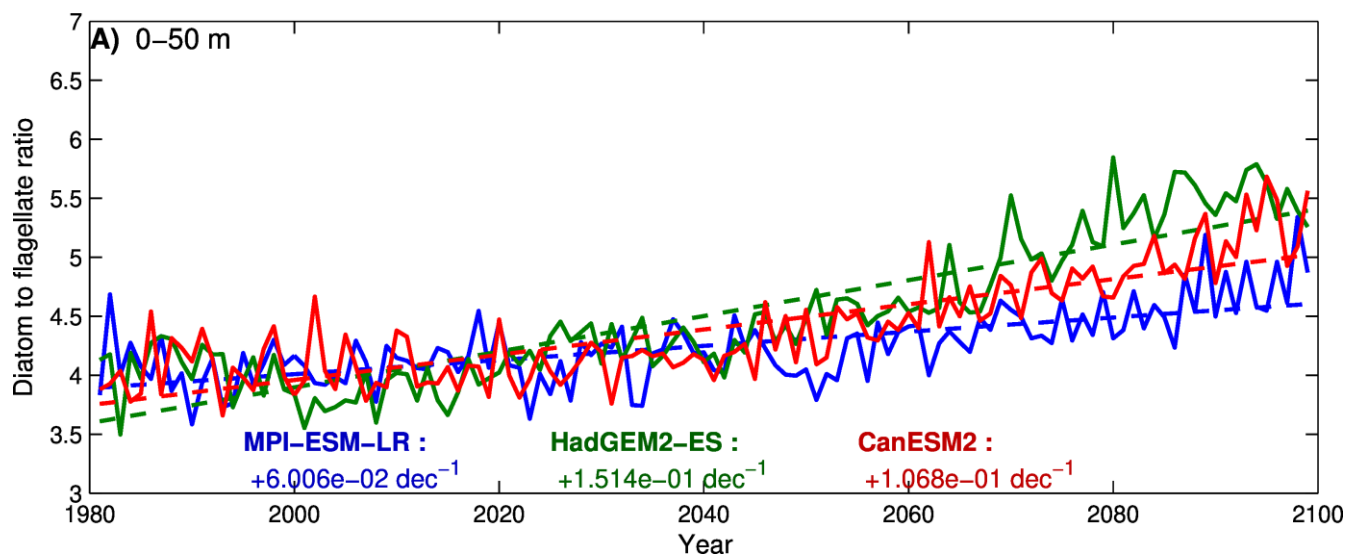


Figure 48. Gulf of St. Lawrence annual mean diatom to flagellate ratio (mol N:mol N) at the 0-50 m depth interval, along with the trend (dashed lines) calculated from 1980-2099 for the simulations forced with MPI-ESM-LR, HadGEM2-ES, and CanESM2 under the RCP 8.5 scenario. The gray areas cover the historical and future time periods represented in the maps and in the annual cycle (Figures 47 and 49).

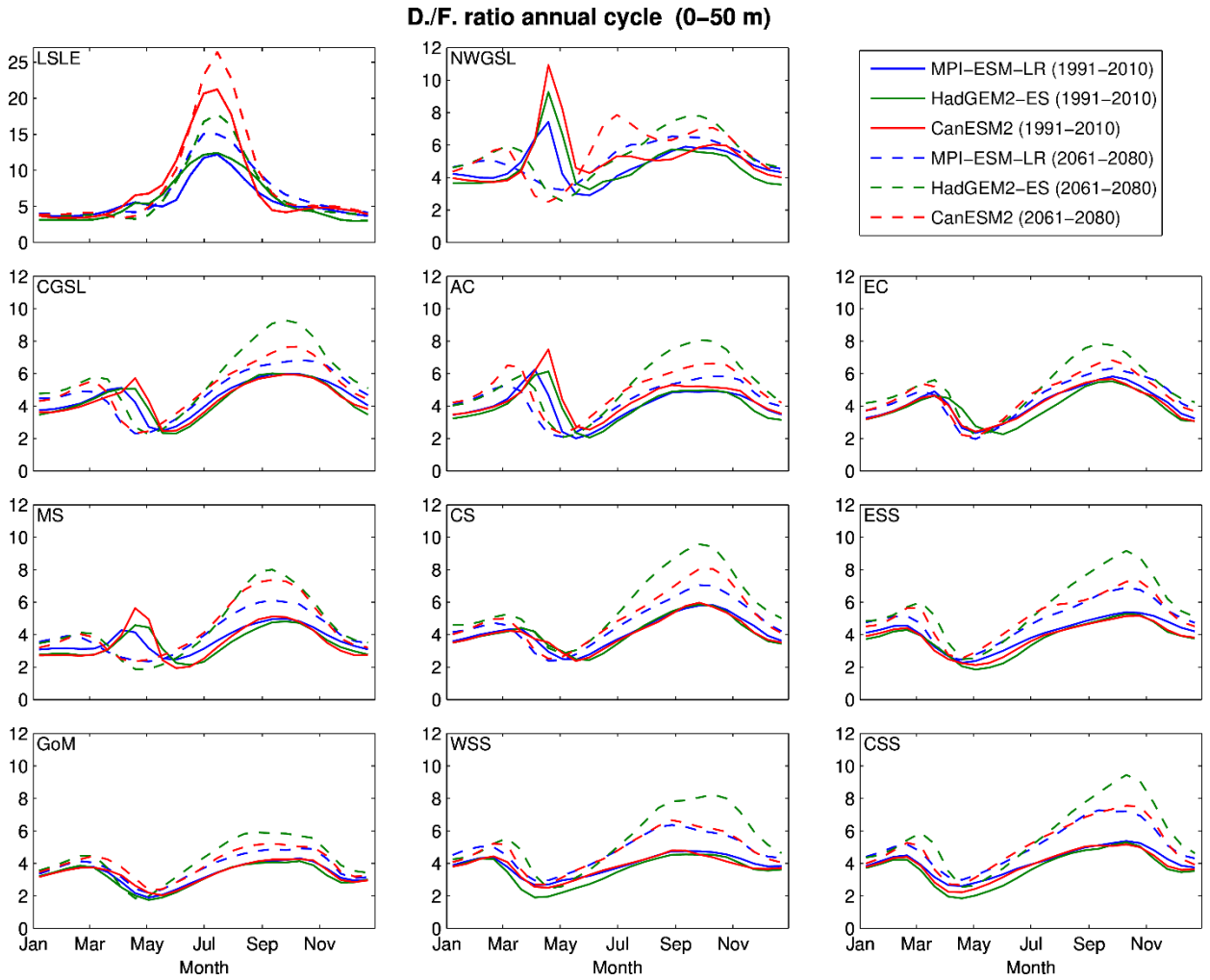


Figure 49. Mean diatom to flagellate ratio (mol N:mol N) annual cycle inside the zones defined in Figure 23 at the 0–50 m depth interval, for the simulations forced with MPI-ESM-LR, HadGEM2-ES, and CanESM2 under the RCP 8.5 scenario. The annual cycle is defined as the average of each step (25 per year) for the 20 years of the historical (solid lines) and the future periods (dashed lines).

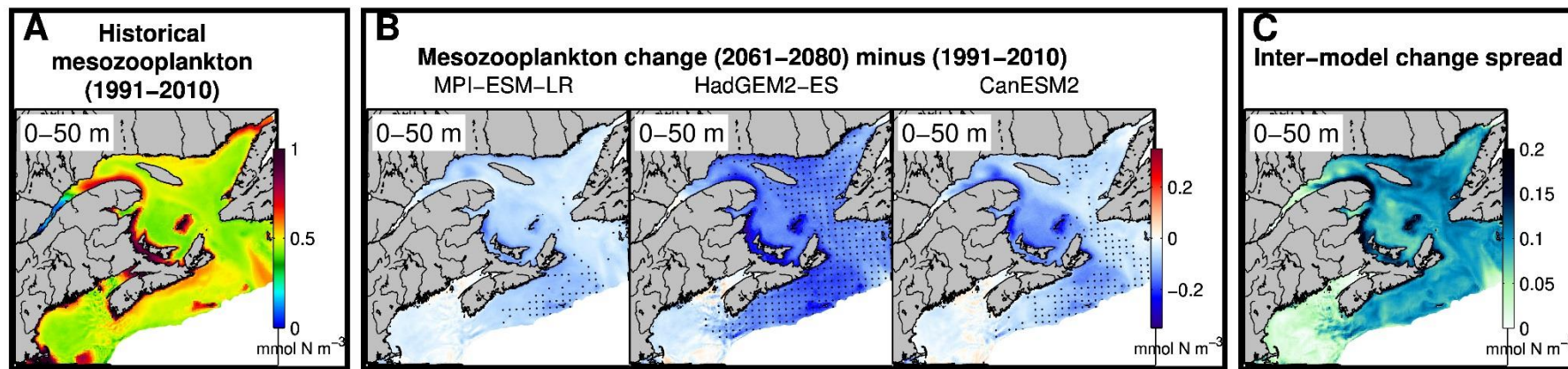


Figure 50. A) Ensemble mean mesozooplankton-N concentration (mmol N m^{-3}) over the 1991-2010 period for the 0-50 m depth interval for the simulations forced with MPI-ESM-LR, HadGEM2-ES, and CanESM2 under the RCP 8.5 scenario, B) Bidecadal mesozooplankton-N concentration change (2061-2080 average minus 1991-2010 average) for each simulation, and C) inter-model change spread. In panel B), the dots represent the area where the future change is greater than three times the standard deviation calculated over the historical period, and where all three simulations agree on the sign of change (positive or negative).

Mean mesozooplankton concentration in the Gulf of St. Lawrence

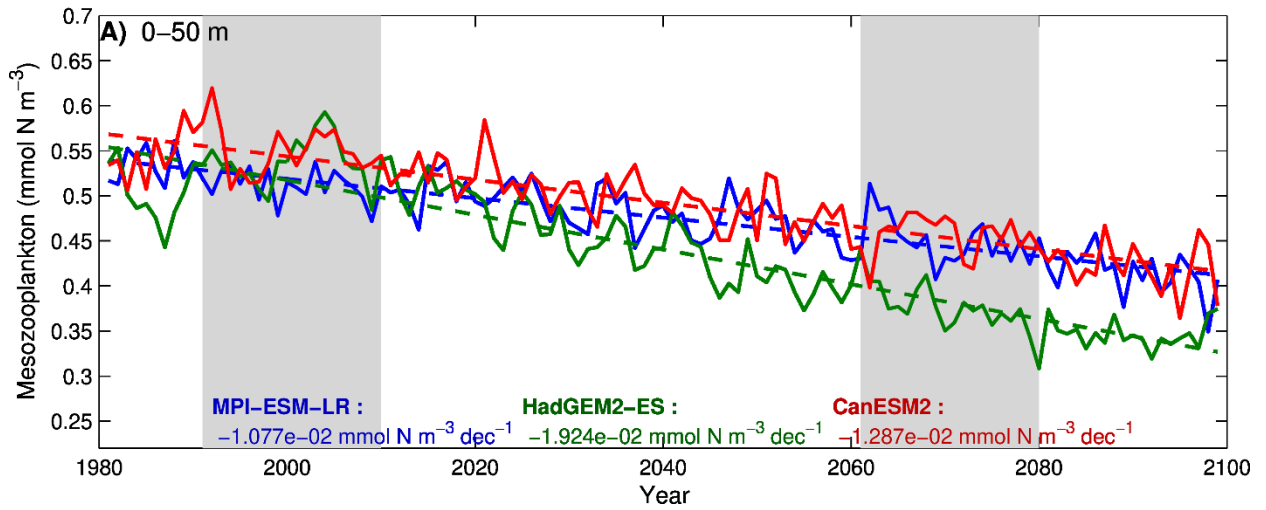


Figure 51. Gulf of St. Lawrence annual mean mesozooplankton-N concentration at the 0-50 m depth interval, along with the trend (dashed lines, mmol N m⁻³ per decade) calculated from 1980-2099 for the simulations forced with MPI-ESM-LR, HadGEM2-ES, and CanESM2 under the RCP 8.5 scenario. The gray areas cover the historical and future time periods represented in the maps and in the annual cycle (Figures 50 and 52).

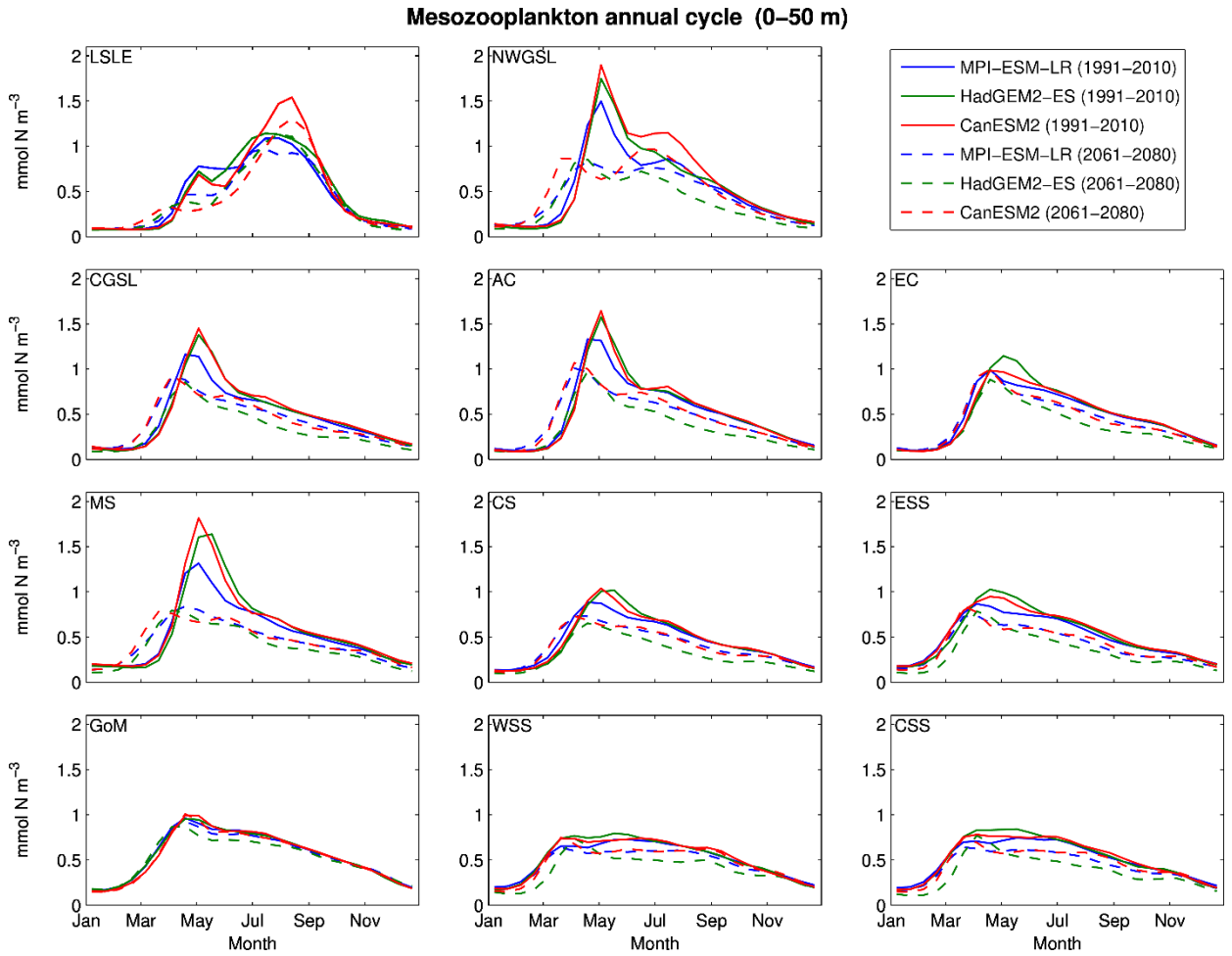


Figure 52. Mean mesozooplankton-N concentration annual cycle inside the zones defined in Figure 23 at the 0–50 m depth interval, for the simulations forced with MPI-ESM-LR, HadGEM2-ES, and CanESM2 under the RCP 8.5 scenario. The annual cycle is defined as the average of each step (25 per year) for the 20 years of the historical (solid lines) and the future periods (dashed lines).

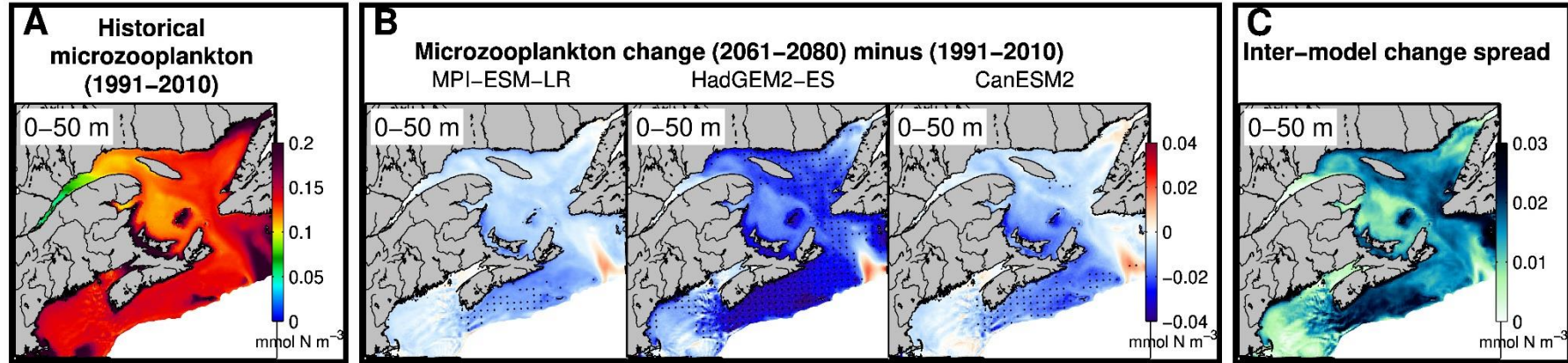


Figure 53. A) Ensemble mean microzooplankton-N concentration (mmol N m^{-3}) over the 1991–2010 period for the 0–50 m depth interval for the simulations forced with MPI-ESM-LR, HadGEM2-ES, and CanESM2 under the RCP 8.5 scenario, B) Bidecadal microzooplankton-N concentration change (2061–2080 average minus 1991–2010 average) for each simulation, and C) inter-model change spread. In panel B), the dots represent the area where the future change is greater than three times the standard deviation calculated over the historical period, and where all three simulations agree on the sign of change (positive or negative).

Mean microzooplankton concentration in the Gulf of St. Lawrence

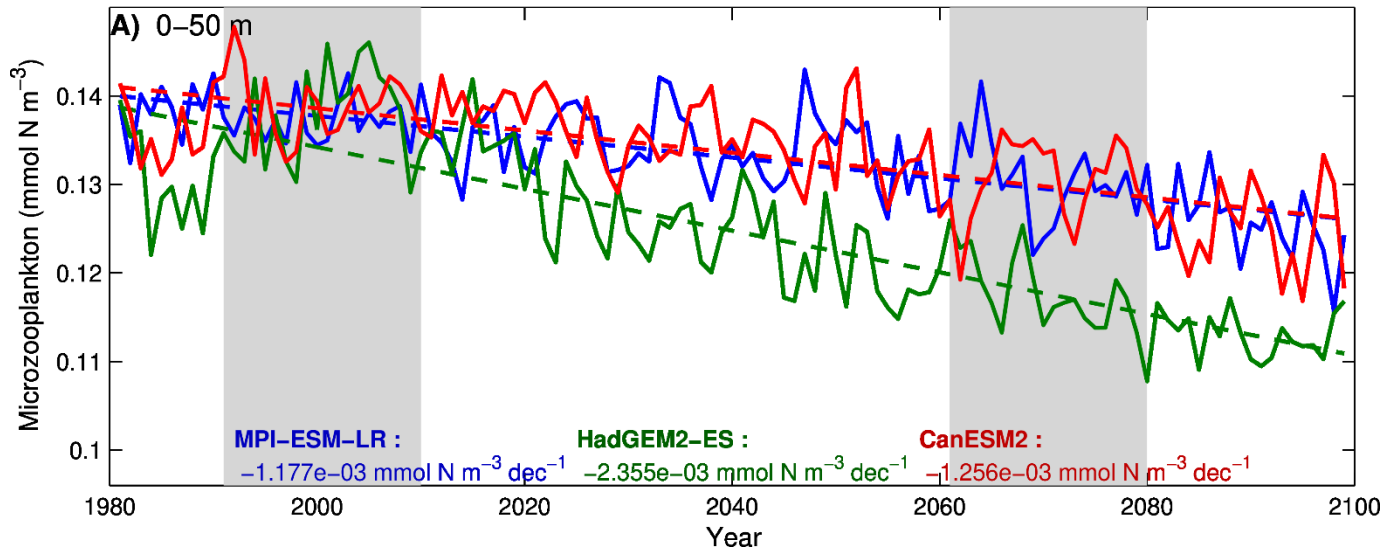


Figure 54. Gulf of St. Lawrence annual mean microzooplankton-N concentration at the 0-50 m depth interval, along with the trend (dashed lines, mmol N m^{-3} per decade) calculated from 1980-2099 for the simulations forced with MPI-ESM-LR, HadGEM2-ES, and CanESM2 under the RCP 8.5 scenario. The gray areas cover the historical and future time periods represented in the maps and in the annual cycle (Figures 53 and 55).

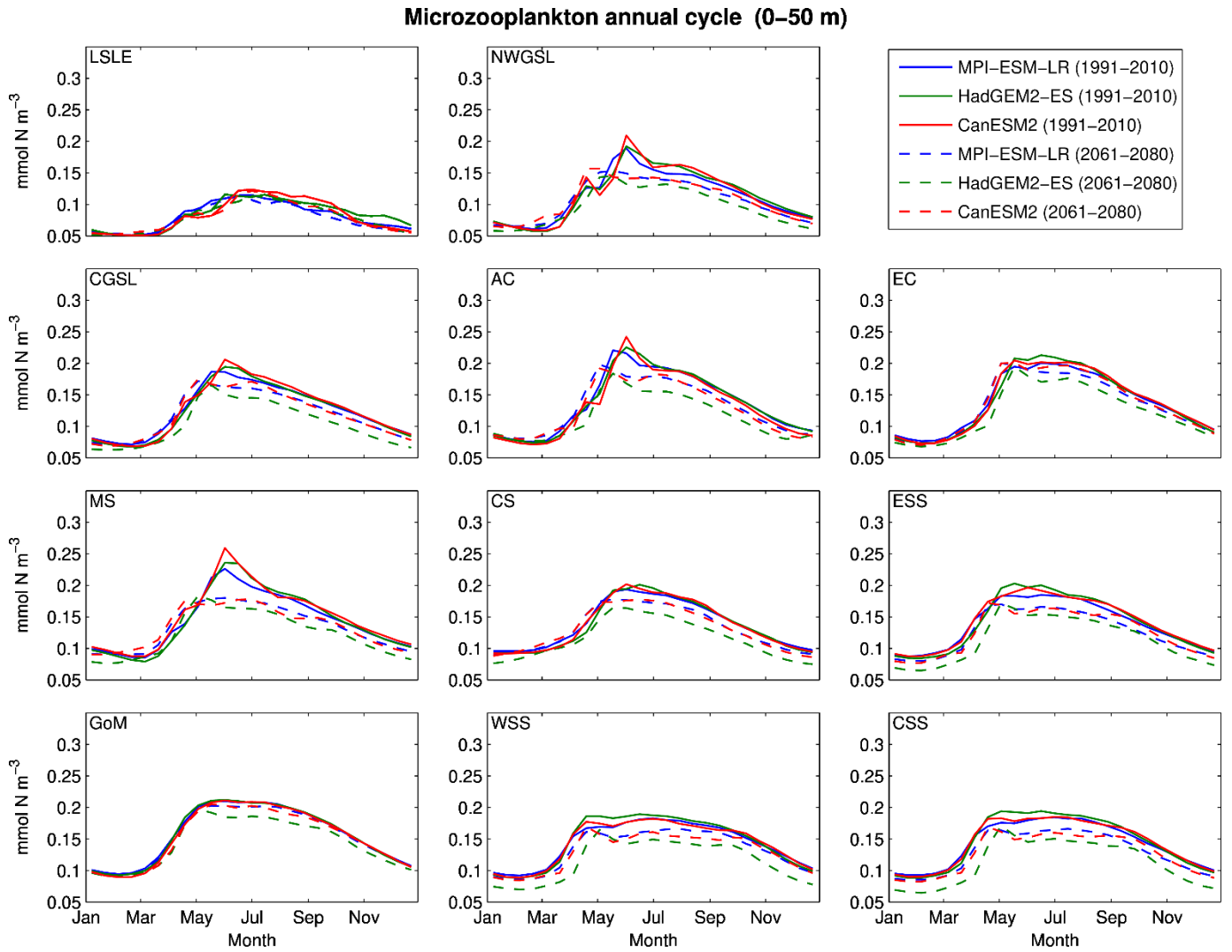


Figure 55. Mean microzooplankton-N concentration annual cycle inside the zones defined in Figure 23 at the 0-50 m depth interval, for the simulations forced with MPI-ESM-LR, HadGEM2-ES, and CanESM2 under the RCP 8.5 scenario. The annual cycle is defined as the average of each step (25 per year) for the 20 years of the historical (solid lines) and the future periods (dashed lines).

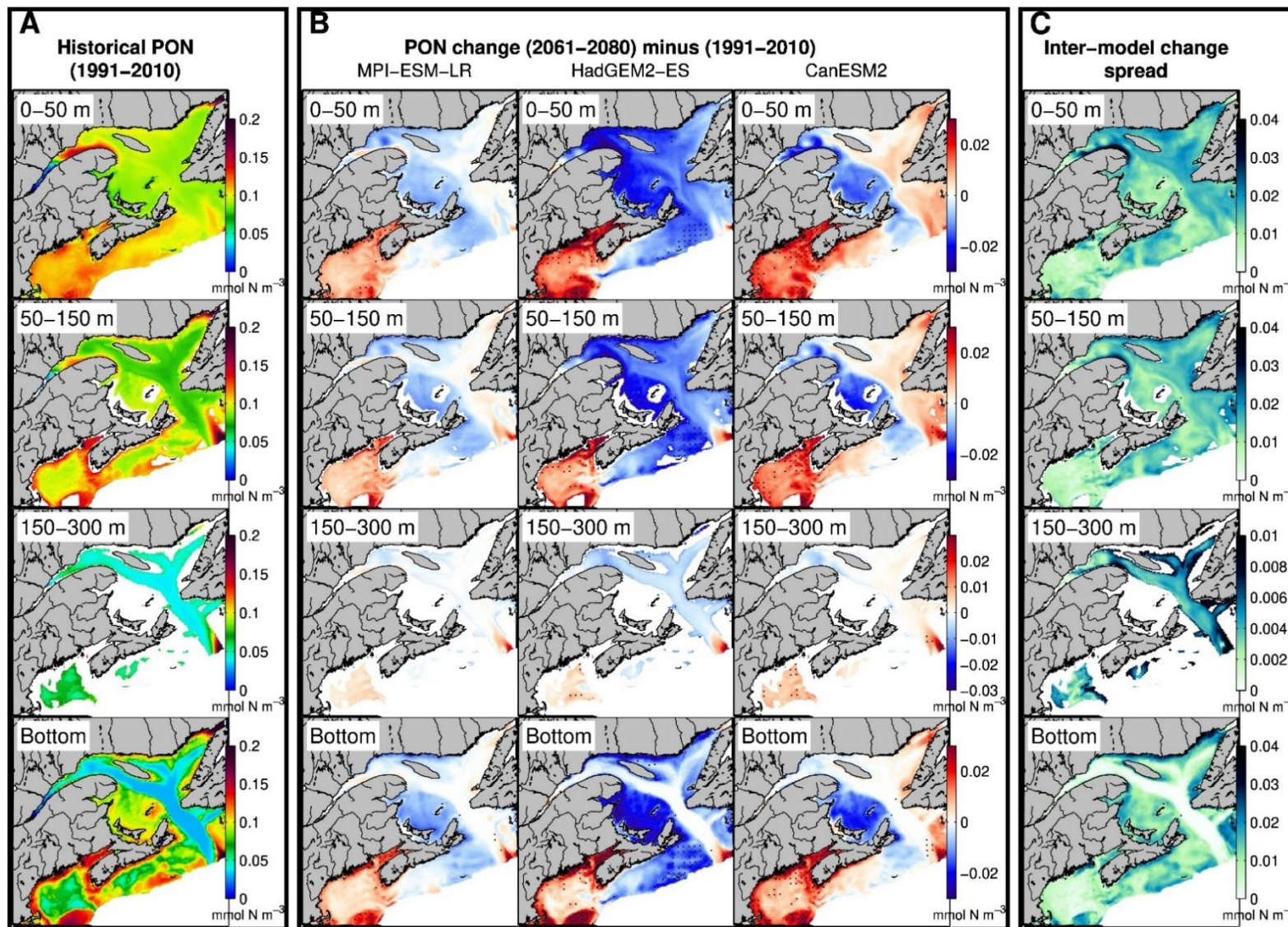


Figure 56. A) Ensemble mean detrital particulate organic nitrogen (PON) concentration (mmol N m^{-3}) over the 1991–2010 period at four depth intervals (0–50 m, 50–150 m, 150–300 m, and bottom) for the simulations forced with MPI-ESM-LR, HadGEM2-ES, and CanESM2 under the RCP 8.5 scenario, B) Bidecadal particulate organic nitrogen concentration change (2061–2080 average minus 1991–2010 average) for each simulation, and C) inter-model change spread. Note that the color scale is sometimes different for the different depth layers. In panel B), the dots represent the area where the future change is greater than three times the standard deviation calculated over the historical period, and where all three simulations agree on the sign of change (positive or negative).

Mean PON concentration in the Gulf of St. Lawrence

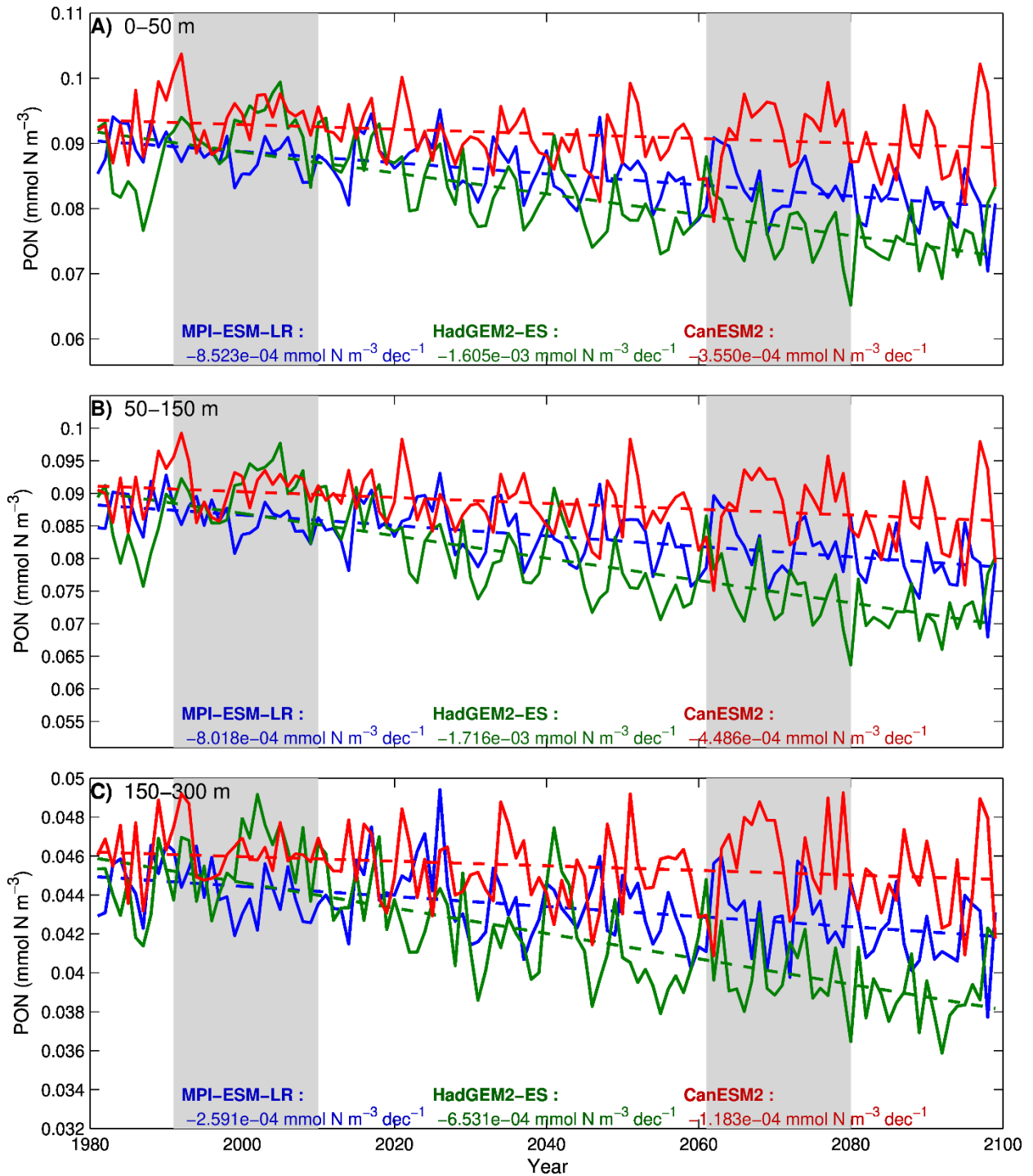


Figure 57. Gulf of St. Lawrence annual mean detrital particulate organic nitrogen (PON) concentration at three depth intervals (0-50 m, 50-150 m and 150-300 m), along with the trend (dashed lines, mmol N m⁻³ per decade) calculated from 1980-2099 for the simulations forced with MPI-ESM-LR, HadGEM2-ES, and CanESM2 under the RCP 8.5 scenario. The gray areas cover the historical and future time periods represented in the maps (Figure 56).

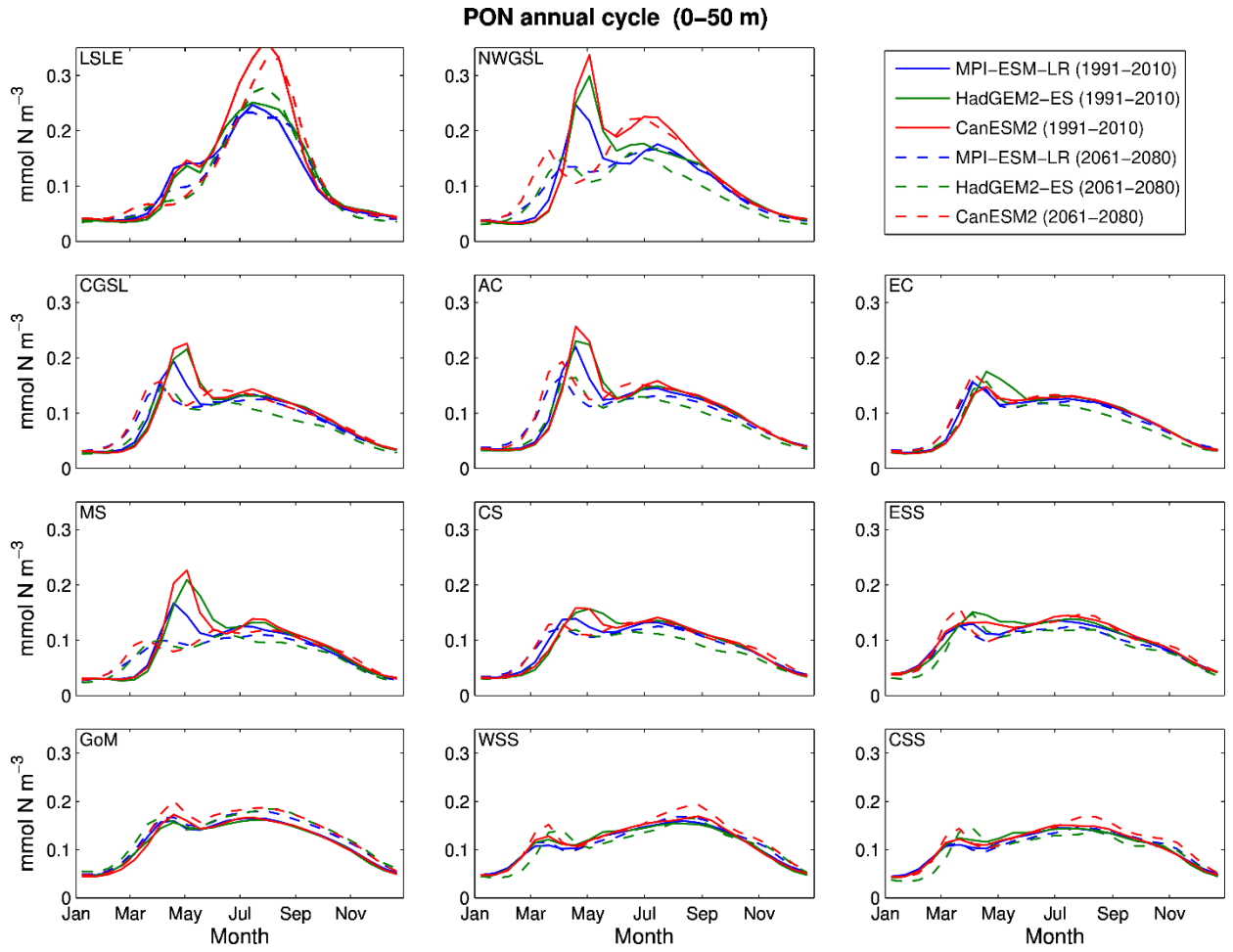


Figure 58. Mean detrital particulate organic matter (PON) concentration annual cycle inside the zones defined in Figure 23 at the 0–50 m depth interval, for the simulations forced with MPI-ESM-LR, HadGEM2-ES, and CanESM2 under the RCP 8.5 scenario. The annual cycle is defined as the average of each step (25 per year) for the 20 years of the historical (solid lines) and the future periods (dashed lines).

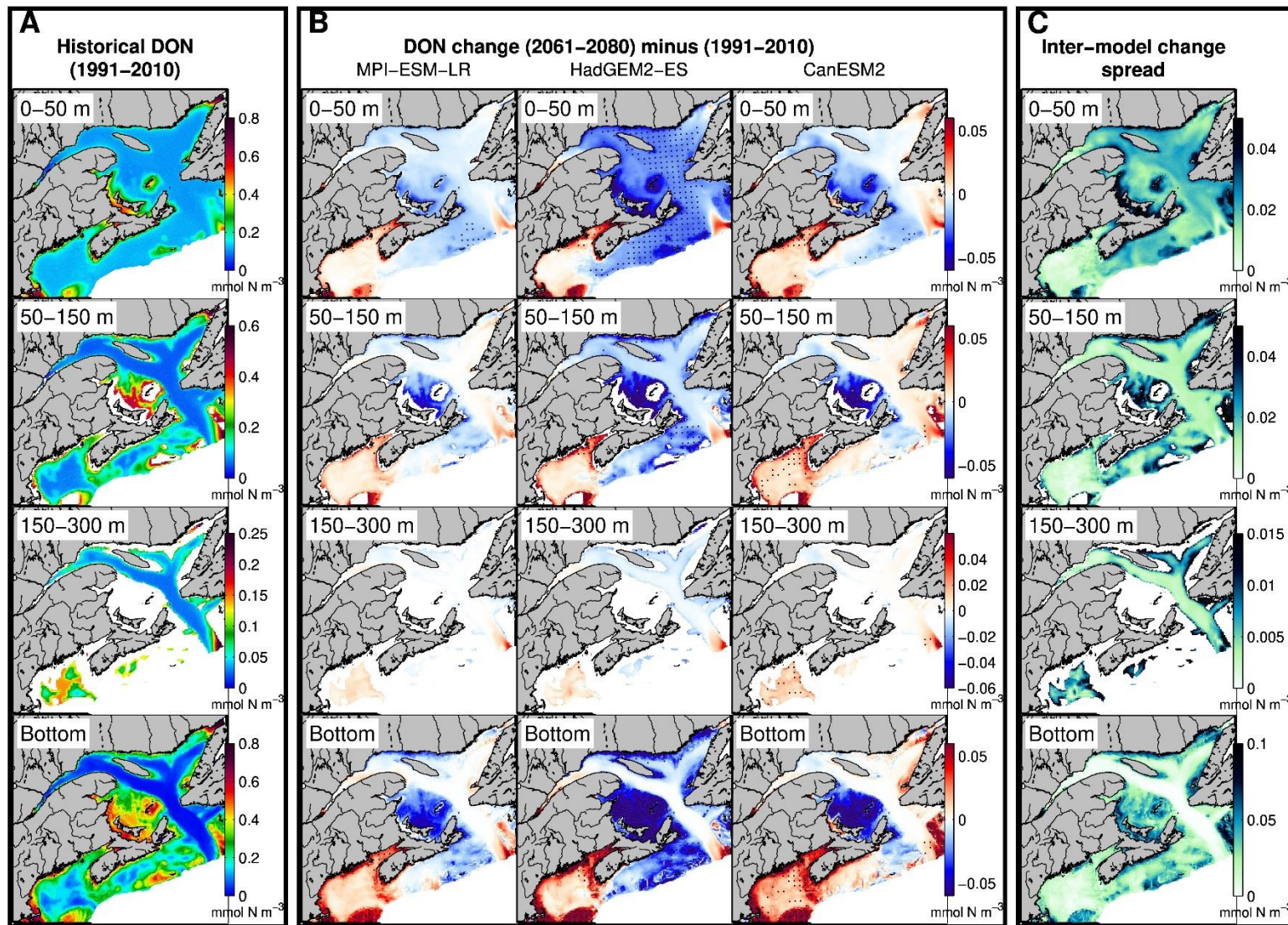


Figure 59. A) Ensemble mean dissolved organic nitrogen (DON) concentration (mmol N m^{-3}) over the 1991-2010 period at four depth intervals (0-50 m, 50-150 m, 150-300 m, and bottom) for the simulations forced with MPI-ESM-LR, HadGEM2-ES, and CanESM2 under the RCP 8.5 scenario, B) Bidecadal dissolved organic nitrogen concentration change (2061-2080 average minus 1991-2010 average) for each simulation, and C) inter-model change spread. Note that the color scale is sometimes different for the different depth layers. In panel B), the dots represent the area where the future change is greater than three times the standard deviation calculated over the historical period, and where all three simulations agree on the sign of change (positive or negative).

Mean DON concentration in the Gulf of St. Lawrence

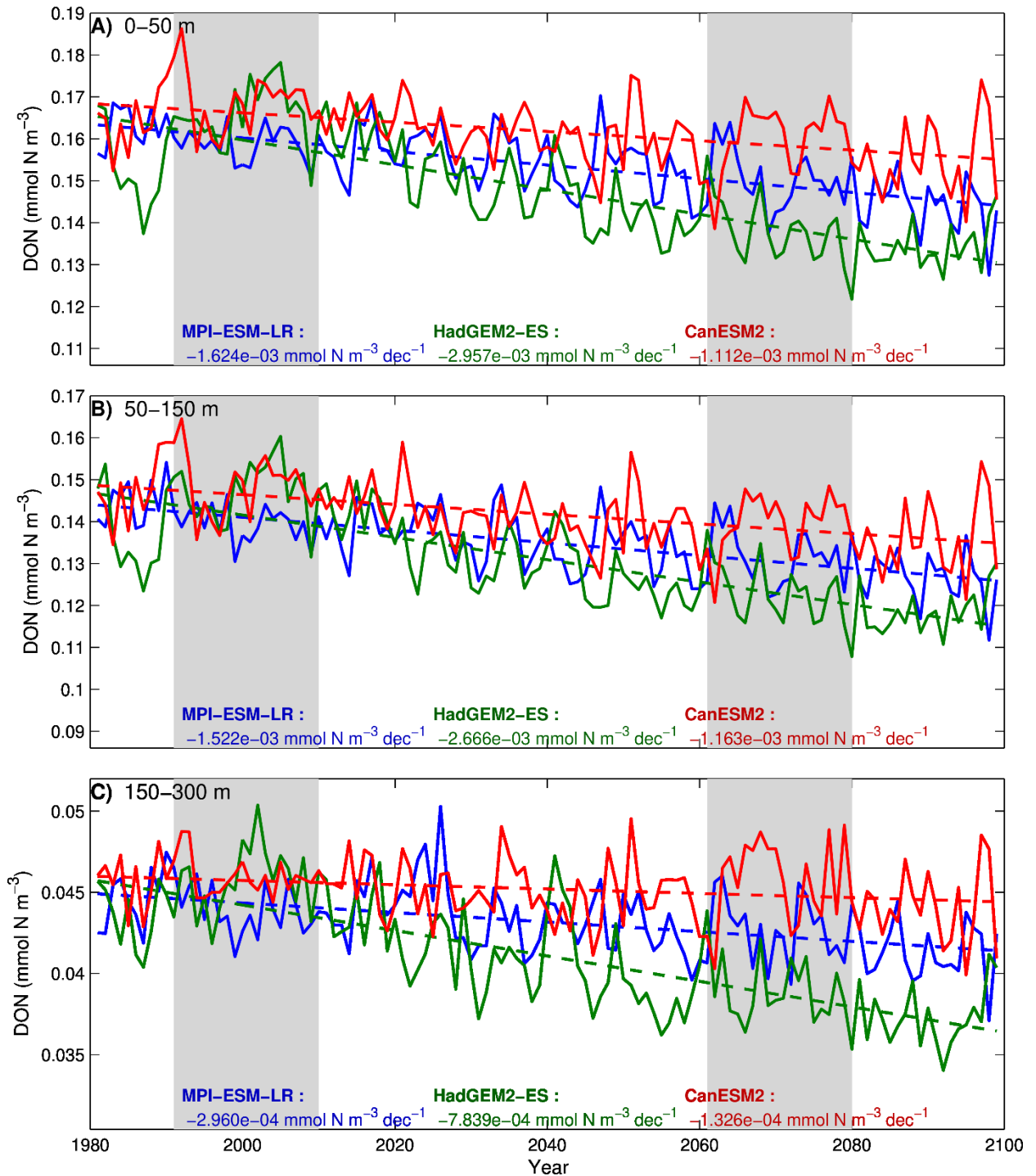


Figure 60. Gulf of St. Lawrence annual mean dissolved organic nitrogen (DON) concentration at three depth intervals (0-50 m, 50-150 m and 150-300 m), along with the trend (dashed lines, mmol N m⁻³ per decade) calculated from 1980-2099 for the simulations forced with MPI-ESM-LR, HadGEM2-ES, and CanESM2 under the RCP 8.5 scenario. The gray areas cover the historical and future time periods represented in the maps (Figure 59).

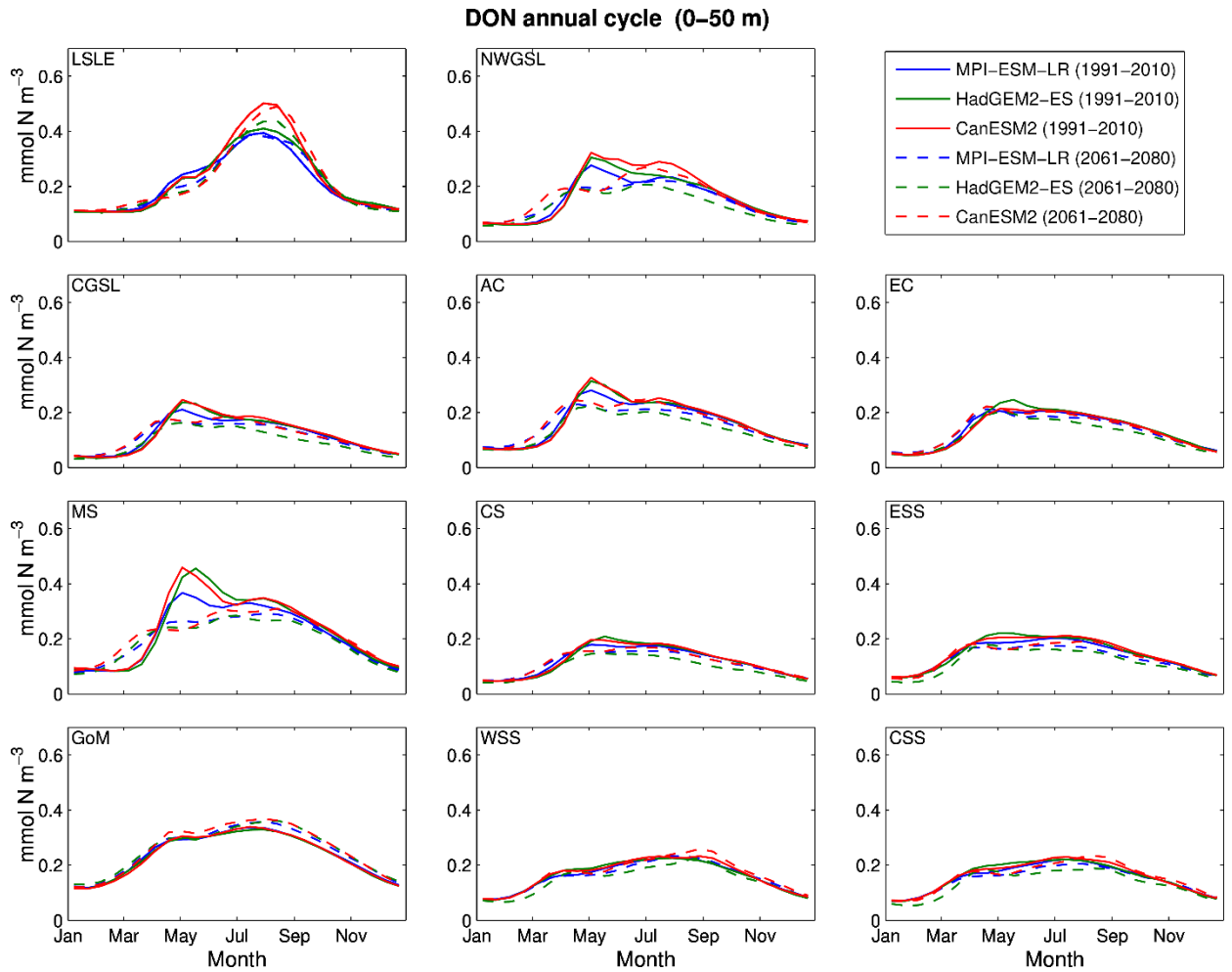


Figure 61. Mean dissolved organic matter (DON) concentration annual cycle inside the zones defined in Figure 23 at the 0–50 m depth interval, for the simulations forced with MPI-ESM-LR, HadGEM2-ES, and CanESM2 under the RCP 8.5 scenario. The annual cycle is defined as the average of each step (25 per year) for the 20 years of the historical (solid lines) and the future periods (dashed lines).

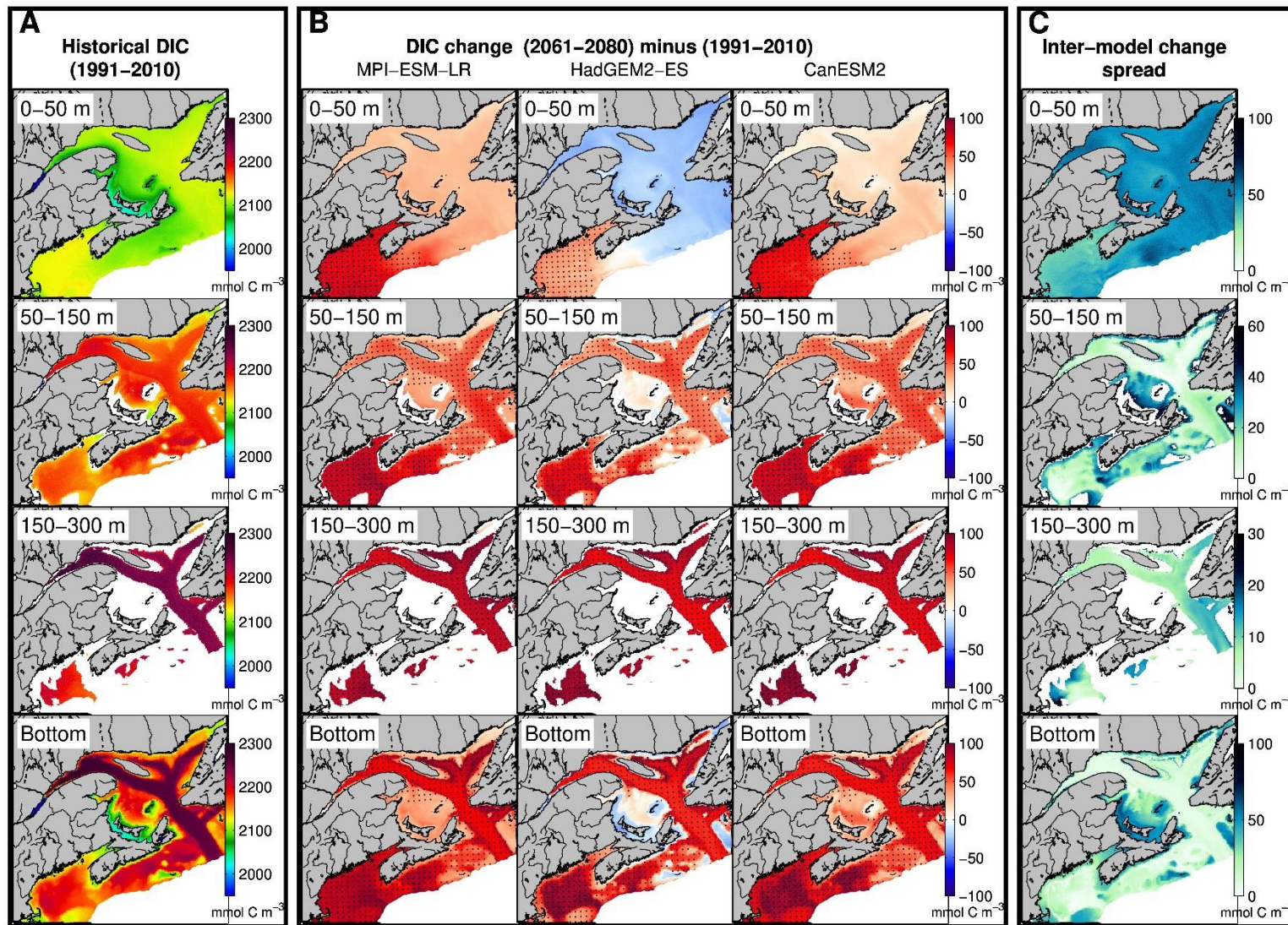


Figure 62. A) Ensemble mean dissolved inorganic carbon (DIC) concentration (mmol C m^{-3}) over the 1991–2010 period at four depth intervals (0–50 m, 50–150 m, 150–300 m, and bottom) for the simulations forced with MPI-ESM-LR, HadGEM2-ES, and CanESM2 under the RCP 8.5 scenario, B) Bidecadal dissolved inorganic carbon concentration change (2061–2080 average minus 1991–2010 average) for each simulation, and C) inter-model change spread. Note that the color scale is sometimes different for the different depth layers. In panel B), the dots represent the area where the future change is greater than three times the standard deviation calculated over the historical period, and where all three simulations agree on the sign of change (positive or negative).

Mean DIC in the Gulf of St. Lawrence

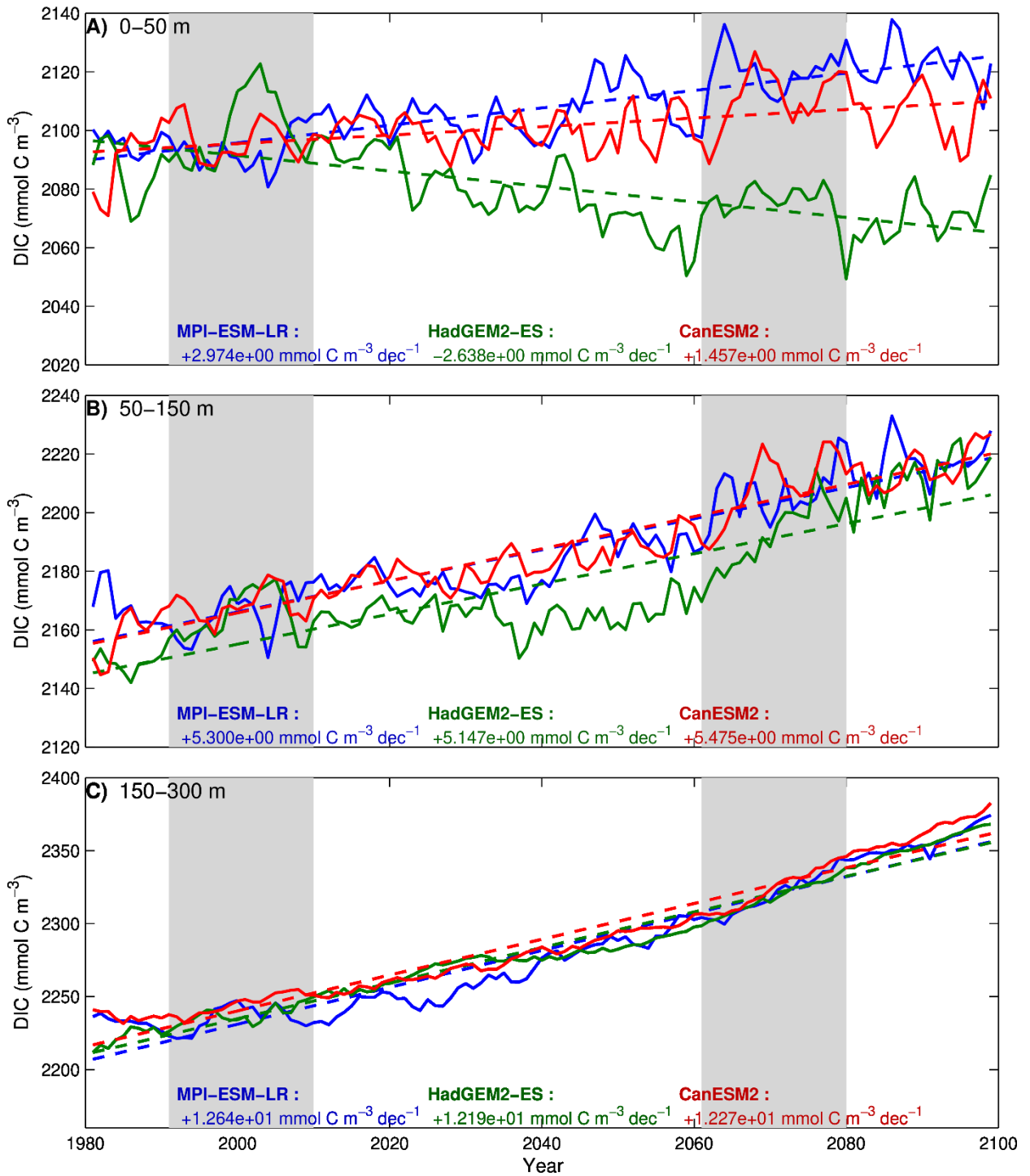


Figure 63. Gulf of St. Lawrence annual mean dissolved inorganic carbon (DIC) concentration at three depth intervals (0–50 m, 50–150 m and 150–300 m), along with the trend (dashed lines, mmol C m^{-3} per decade) calculated from 1980–2099 for the simulations forced with MPI-ESM-LR, HadGEM2-ES, and CanESM2 under the RCP 8.5 scenario. The gray areas cover the historical and future time periods represented in the maps (Figure 62).

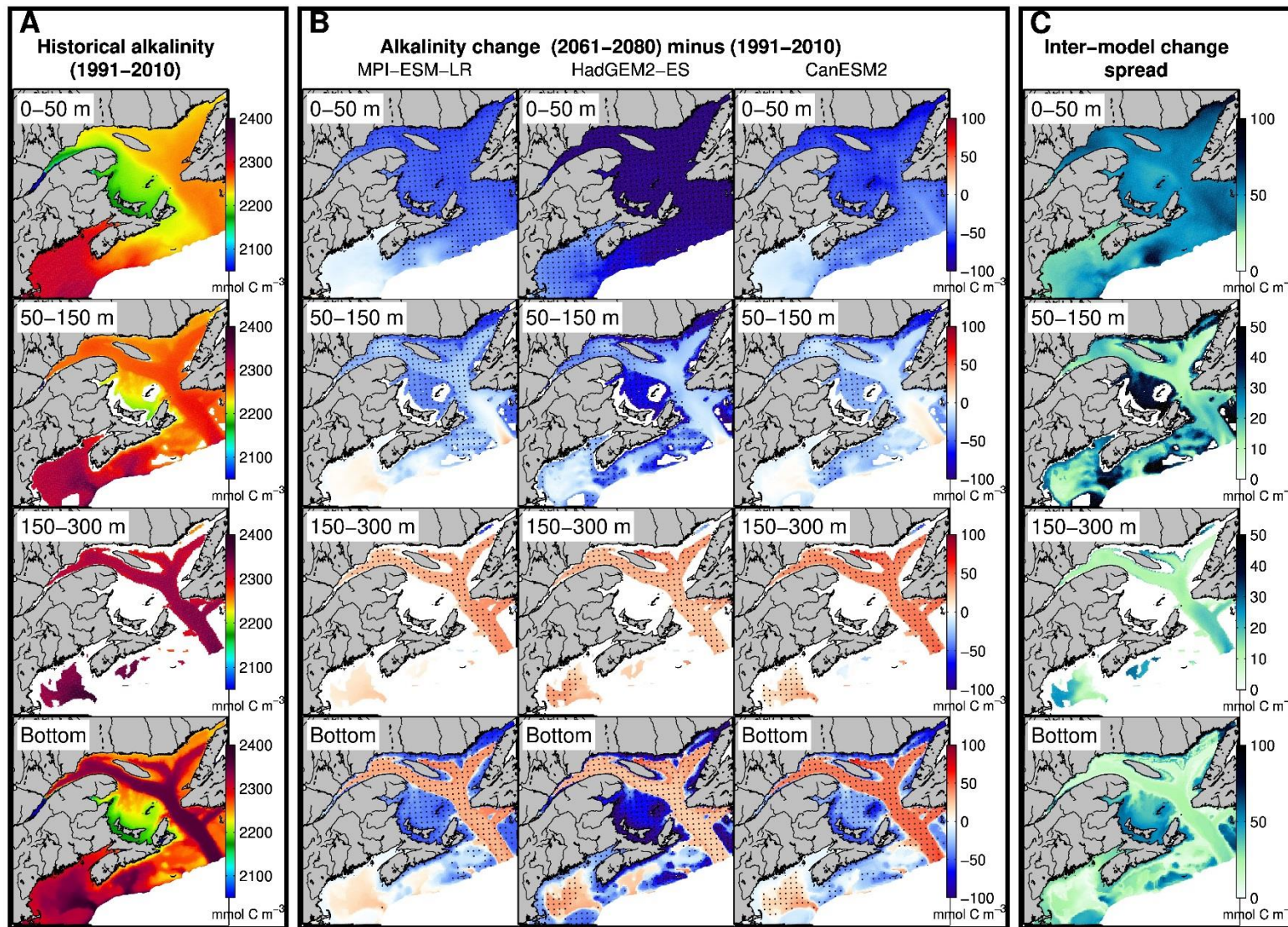


Figure 64. A) Ensemble mean alkalinity (mmol C m^{-3}) over the 1991–2010 period at four depth intervals (0–50 m, 50–150 m, 150–300 m, and bottom) for the simulations forced with MPI-ESM-LR, HadGEM2-ES, and CanESM2 under the RCP 8.5 scenario, B) Bidecadal alkalinity change (2061–2080 average minus 1991–2010 average) for each simulation, and C) inter-model change spread. Note that the color scale is sometimes different for the different depth layers. In panel B), the dots represent the area where the future change is greater than three times the standard deviation calculated over the historical period, and where all three simulations agree on the sign of change (positive or negative).

Mean alkalinity in the Gulf of St. Lawrence

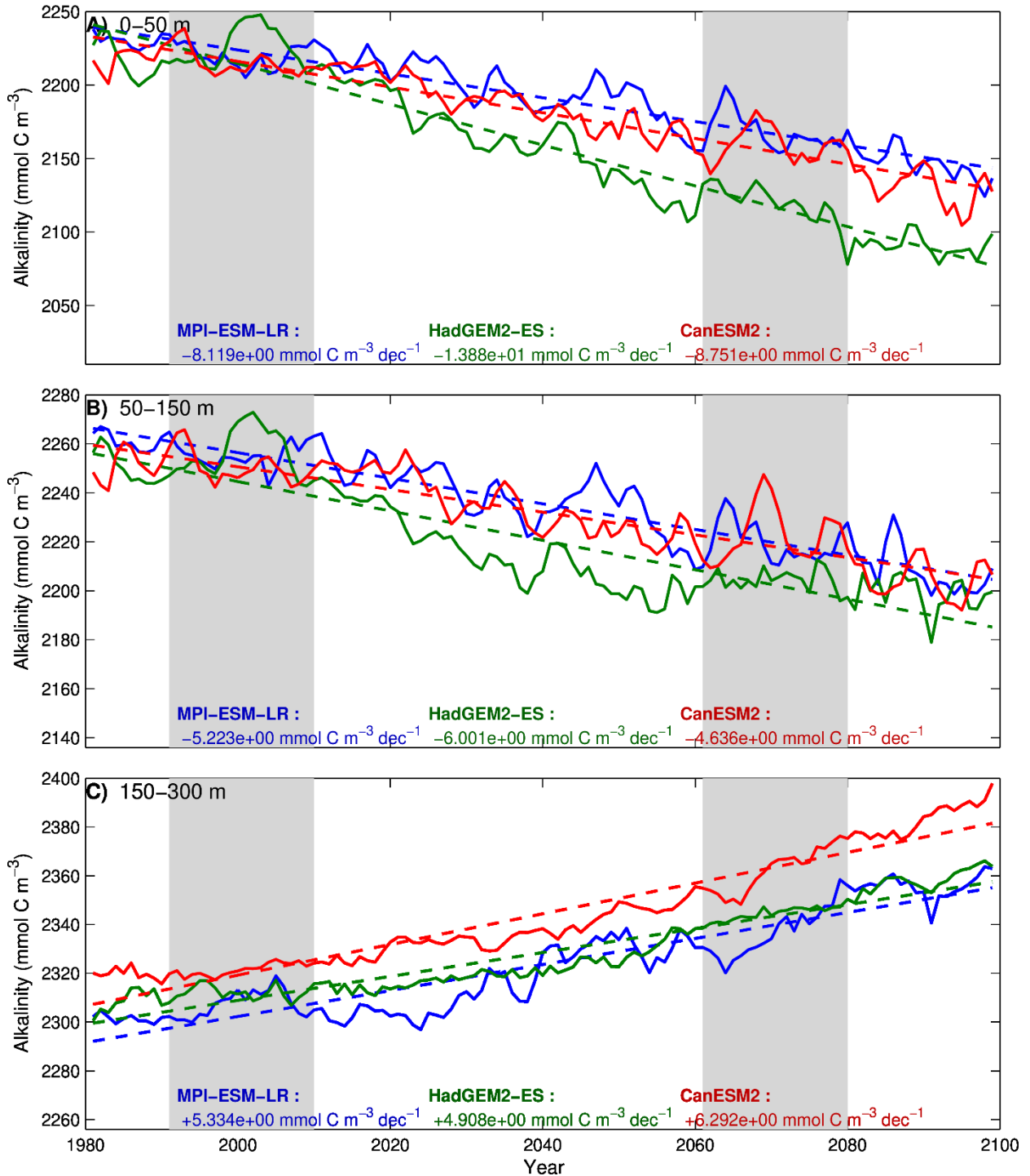


Figure 65. Gulf of St. Lawrence annual mean alkalinity at three depth intervals (0–50 m, 50–150 m and 150–300 m), along with the trend (dashed lines, mmol C m^{-3} per decade) calculated from 1980–2099 for the simulations forced MPI-ESM-LR, HadGEM2-ES, and CanESM2 under the RCP 8.5 scenario. The gray areas cover the historical and future time periods represented in the maps (Figure 64).

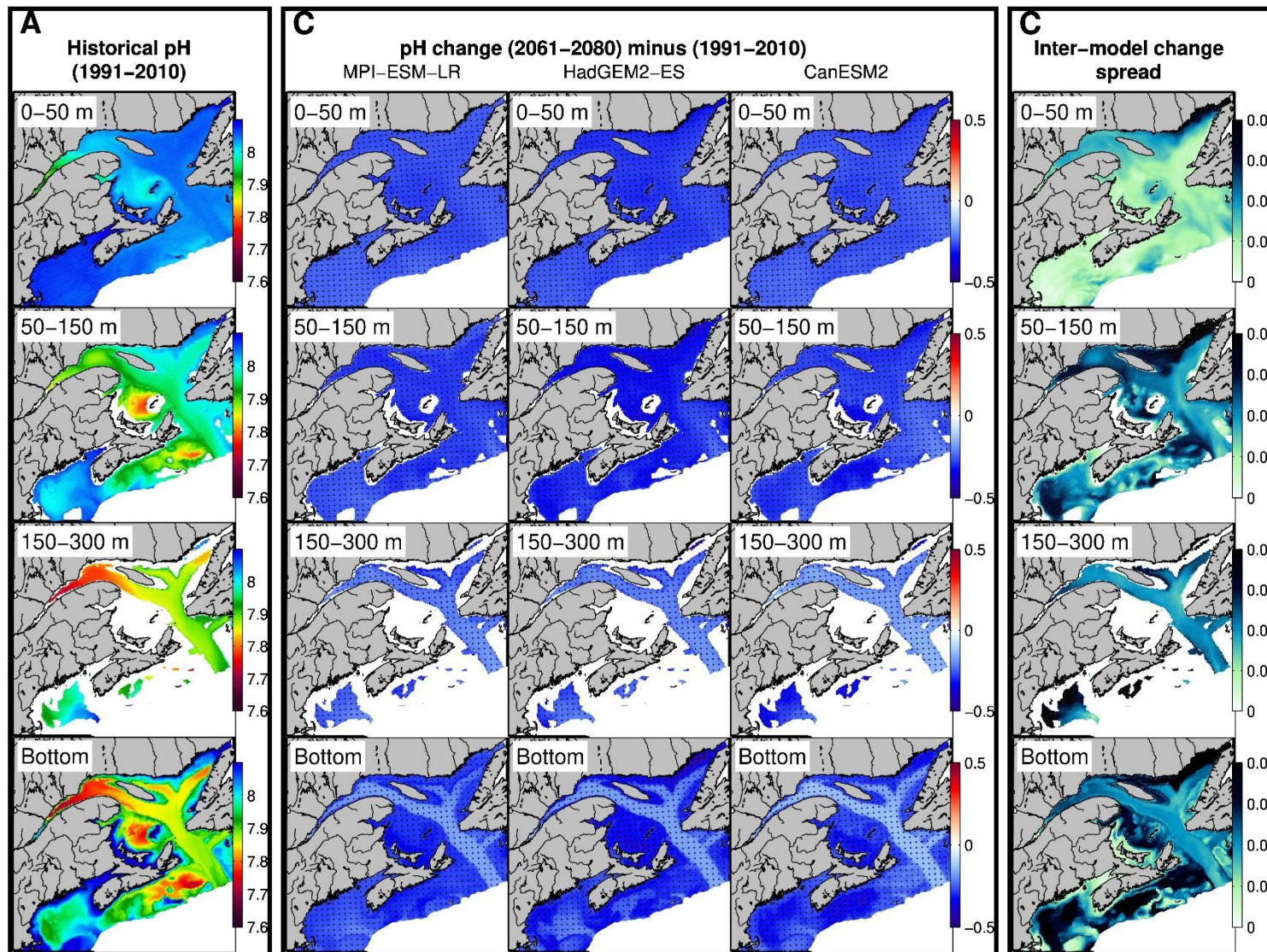


Figure 66. A) Ensemble mean pH_{total} over the 1991–2010 period at four depth intervals (0–50 m, 50–150 m, 150–300 m, and bottom) for the simulations forced with MPI-ESM-LR, HadGEM2-ES, and CanESM2 under the RCP 8.5 scenario, B) Bidecadal pH_{total} change (2061–2080 average minus 1991–2010 average) for each simulation, and C) inter-model change spread. Note that the color scale is sometimes different for the different depth layers. In panel B), the dots represent the area where the future change is greater than three times the standard deviation calculated over the historical period, and where all three simulations agree on the sign of change (positive or negative).

Mean pH in the Gulf of St. Lawrence

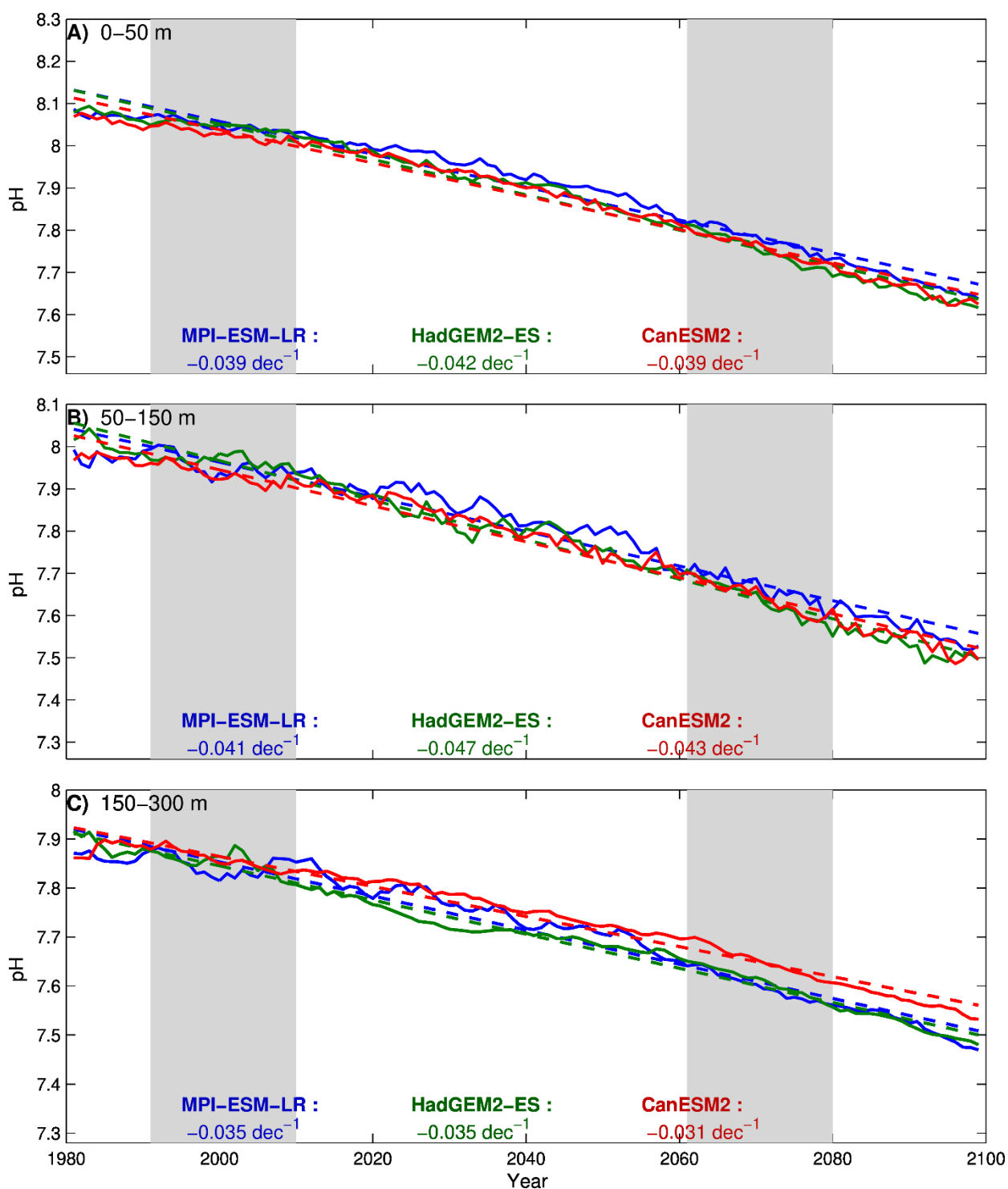


Figure 67. Annual mean pH_{total} in the Gulf of St. Lawrence at three depth intervals (0–50 m, 50–150 m and 150–300 m), along with the trend (dashed lines) calculated from 1980–2099 for the simulations forced MPI-ESM-LR, HadGEM2-ES, and CanESM2 under the RCP 8.5 scenario. The gray areas cover the historical and future time periods represented in the maps (Figure 66).

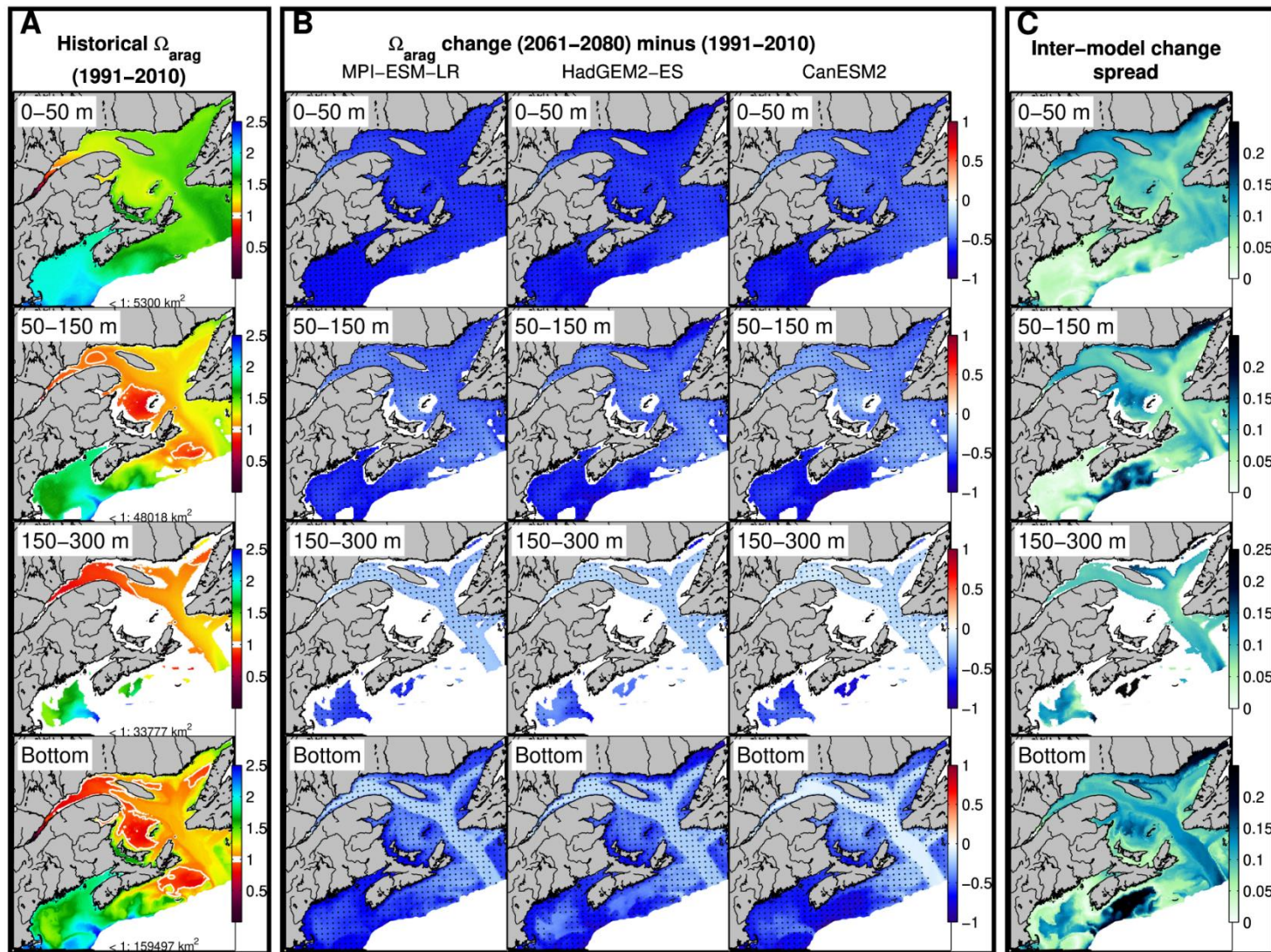


Figure 68. A) Ensemble mean aragonite saturation state (Ω_{arag}) over the 1991-2010 period at four depth intervals (0-50 m, 50-150 m, 150-300 m, and bottom) for the simulations forced with MPI-ESM-LR, HadGEM2-ES, and CanESM2 under the RCP 8.5 scenario. The white line represent the $\Omega_{\text{arag}}=1$ threshold and the area bathing in water with $\Omega_{\text{arag}}<1$ is indicated at the bottom of the graph. B) Bidecadal aragonite saturation state change (2061-2080 average minus 1991-2010 average) for each simulation, and C) inter-model change spread. In panel B), the dots represent the area where the future change is greater than three times the standard deviation calculated over the historical period, and where all three simulations agree on the sign of change (positive or negative).

Mean Ω_{arag} in the Gulf of St. Lawrence

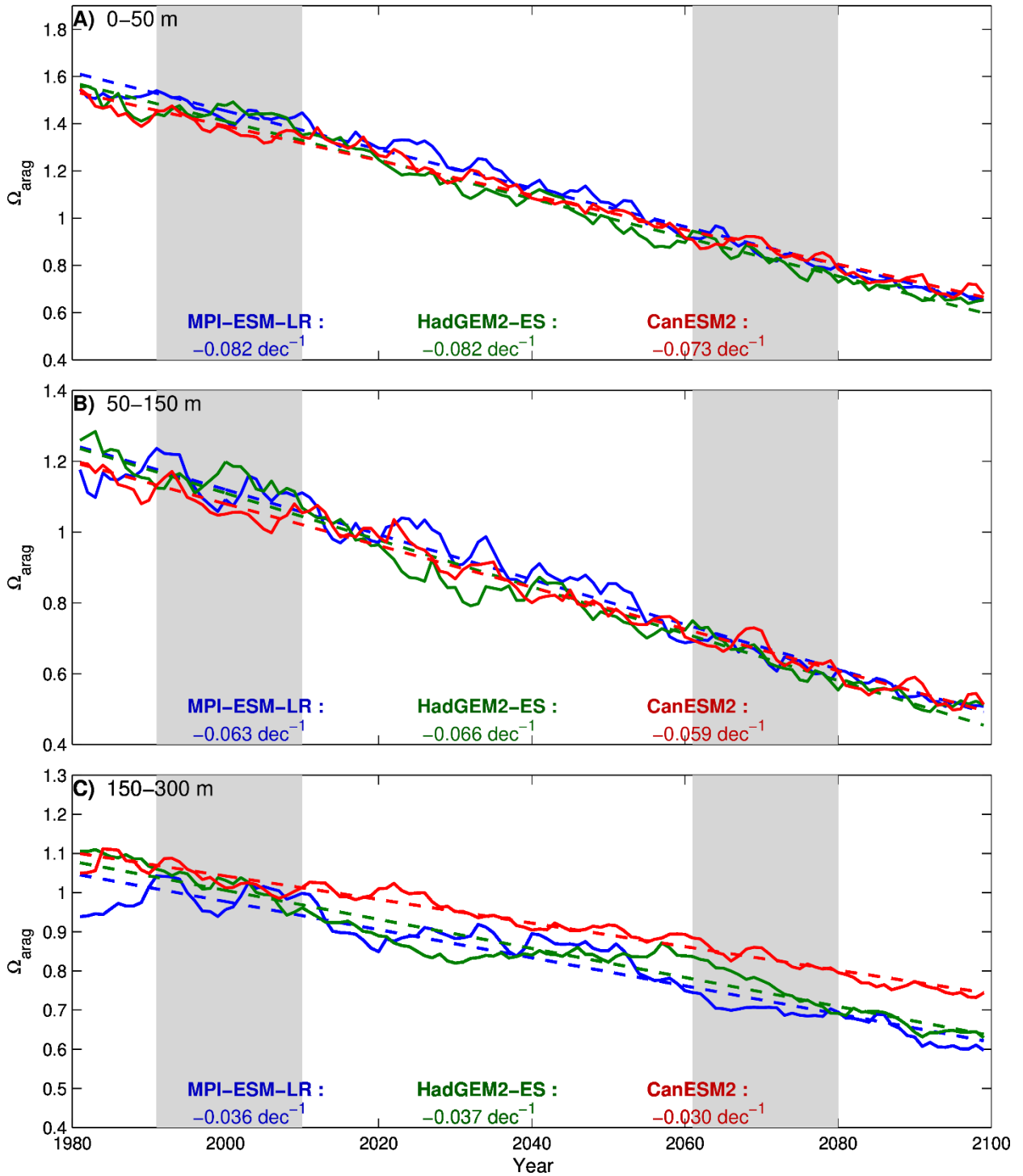


Figure 69. Annual mean aragonite saturation state (Ω_{arag}) in the Gulf of St. Lawrence at three depth intervals (0–50 m, 50–150 m and 150–300 m), along with the trend (dashed lines) calculated from 1980–2099 for the simulations forced MPI-ESM-LR, HadGEM2-ES, and CanESM2 under the RCP 8.5 scenario. The gray areas cover the historical and future time periods represented in the maps (Figure 68).

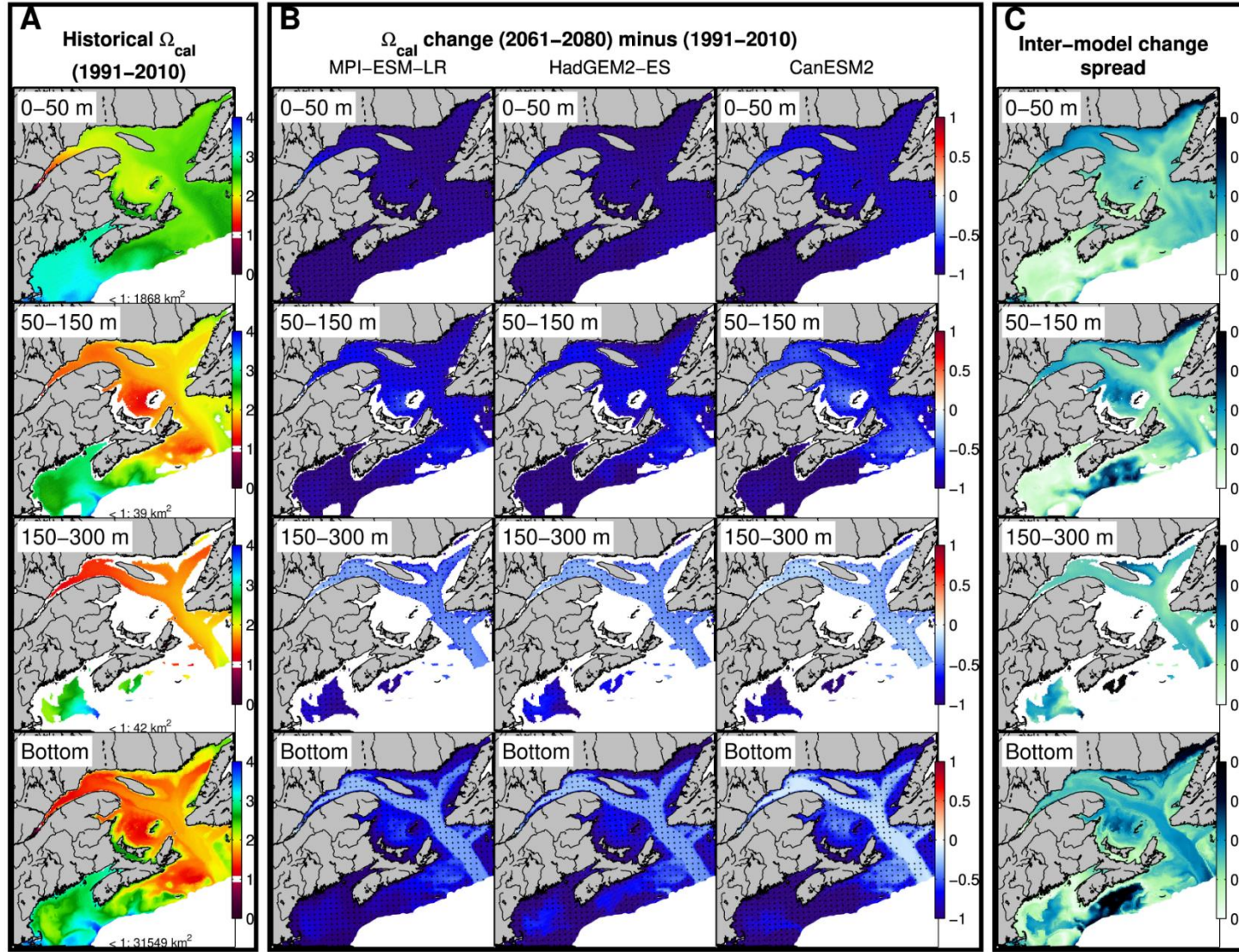


Figure 70. A) Ensemble mean calcite saturation state (Ω_{cal}) over the 1991–2010 period at four depth intervals (0–50 m, 50–150 m, 150–300 m, and bottom) for the simulations forced with MPI-ESM-LR, HadGEM2-ES, and CanESM2 under the RCP 8.5 scenario. The white line represent the $\Omega_{cal}=1$ threshold and the area bathing in water with $\Omega_{cal}<1$ is indicated at the bottom of the graph. B) Bidecadal calcite saturation state change (2061–2080 average minus 1991–2010 average) for each simulation, and C) inter-model change spread. In panel B), the dots represent the area where the future change is greater than three times the standard deviation calculated over the historical period, and where all three simulations agree on the sign of change (positive or negative).

Mean Ω_{cal} in the Gulf of St. Lawrence

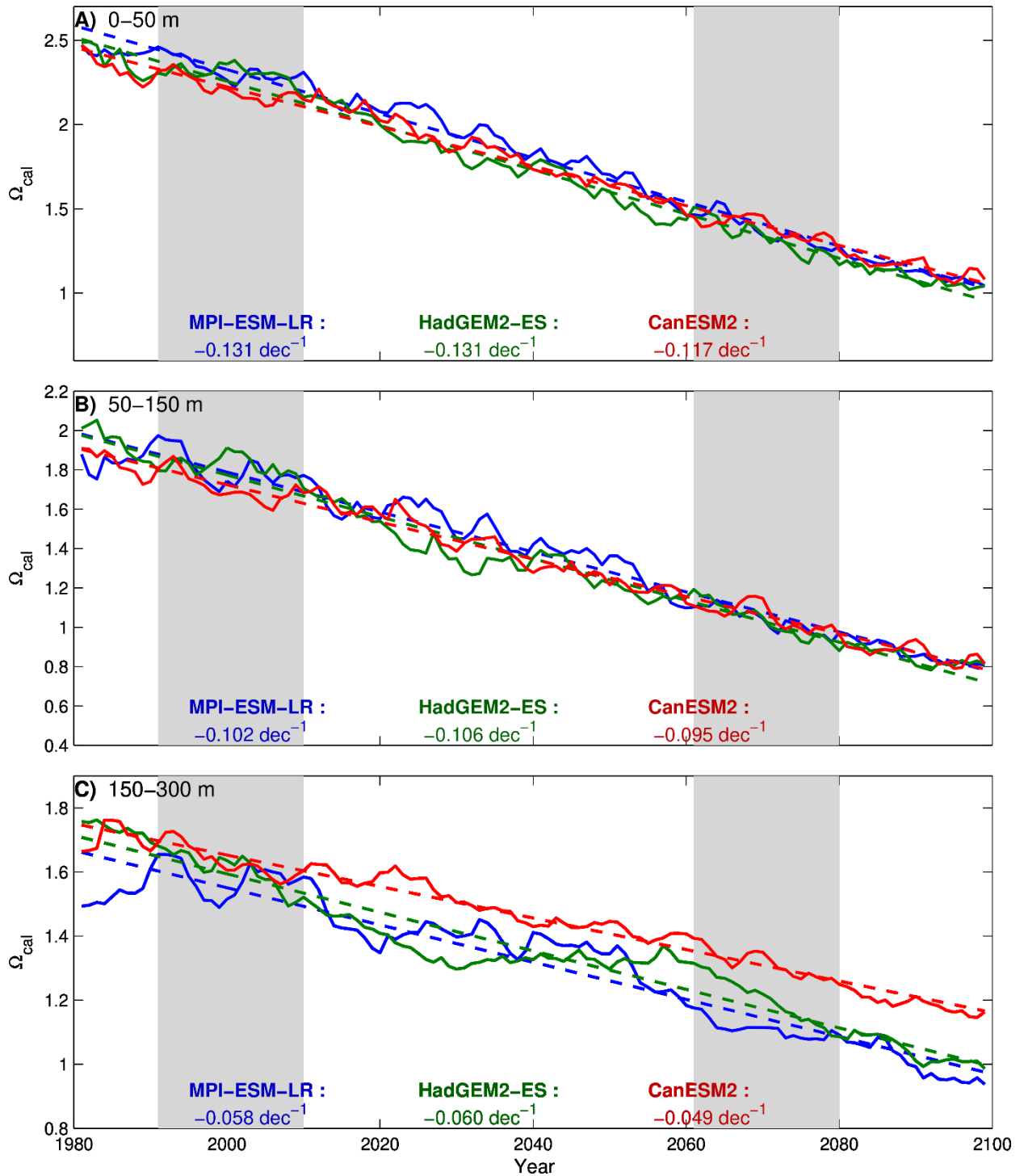


Figure 71. Annual mean calcite saturation state (Ω_{cal}) in the Gulf of St. Lawrence at three depth intervals (0–50 m, 50–150 m and 150–300 m), along with the trend (dashed lines) calculated from 1980–2099 for the simulations forced MPI-ESM-LR, HadGEM2-ES, and CanESM2 under the RCP 8.5 scenario. The gray areas cover the historical and future time periods represented in the maps and in the annual cycle (previous and next figures).

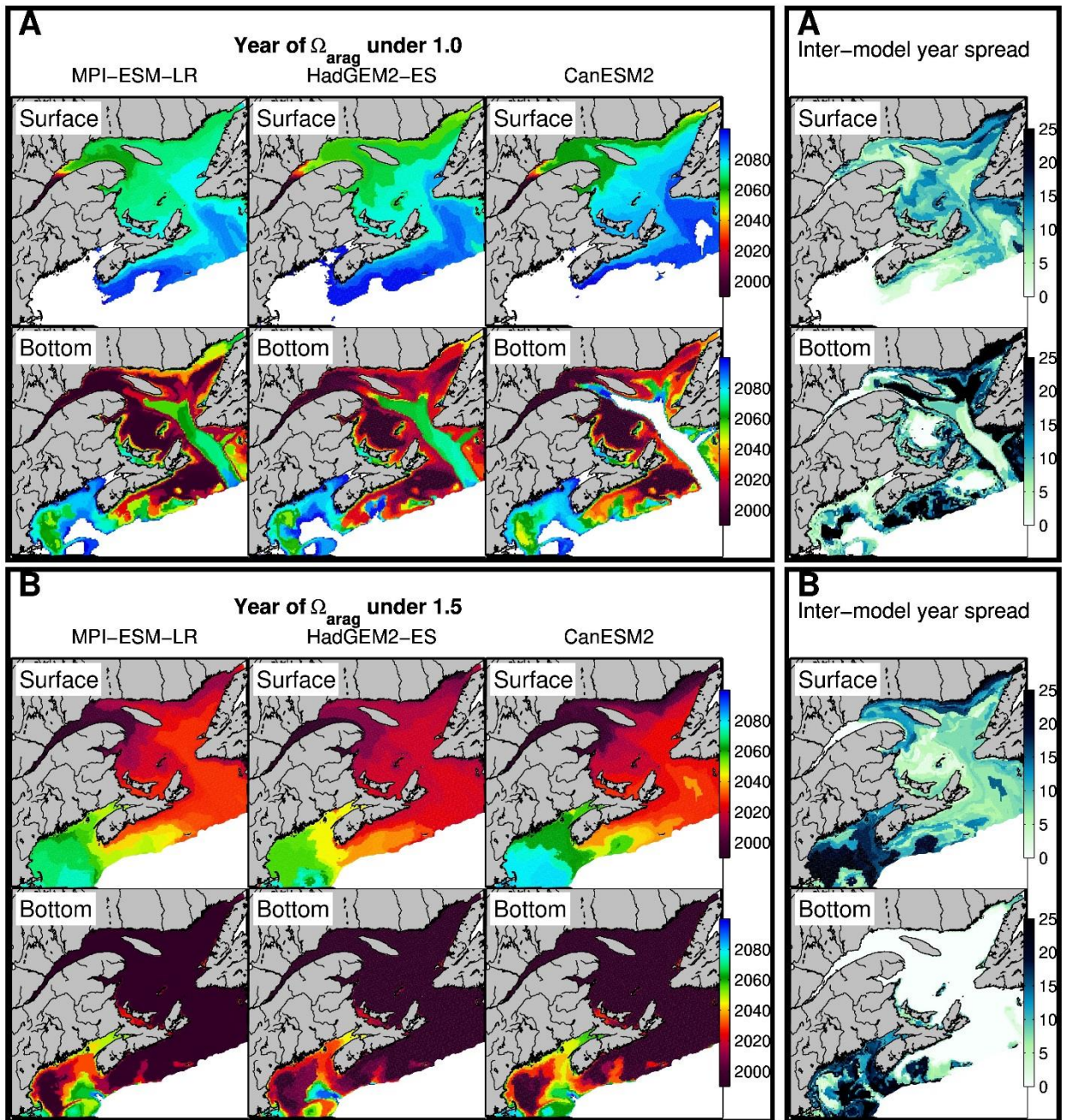


Figure 72. Year at which the surface and bottom aragonite saturation state (Ω_{arag}) reach a value of 1.0 (A) and a value of 1.5 (B). White areas mean that saturation states do not reach these critical values during the study period. Right panels show the inter-model change spread in the calculated year.

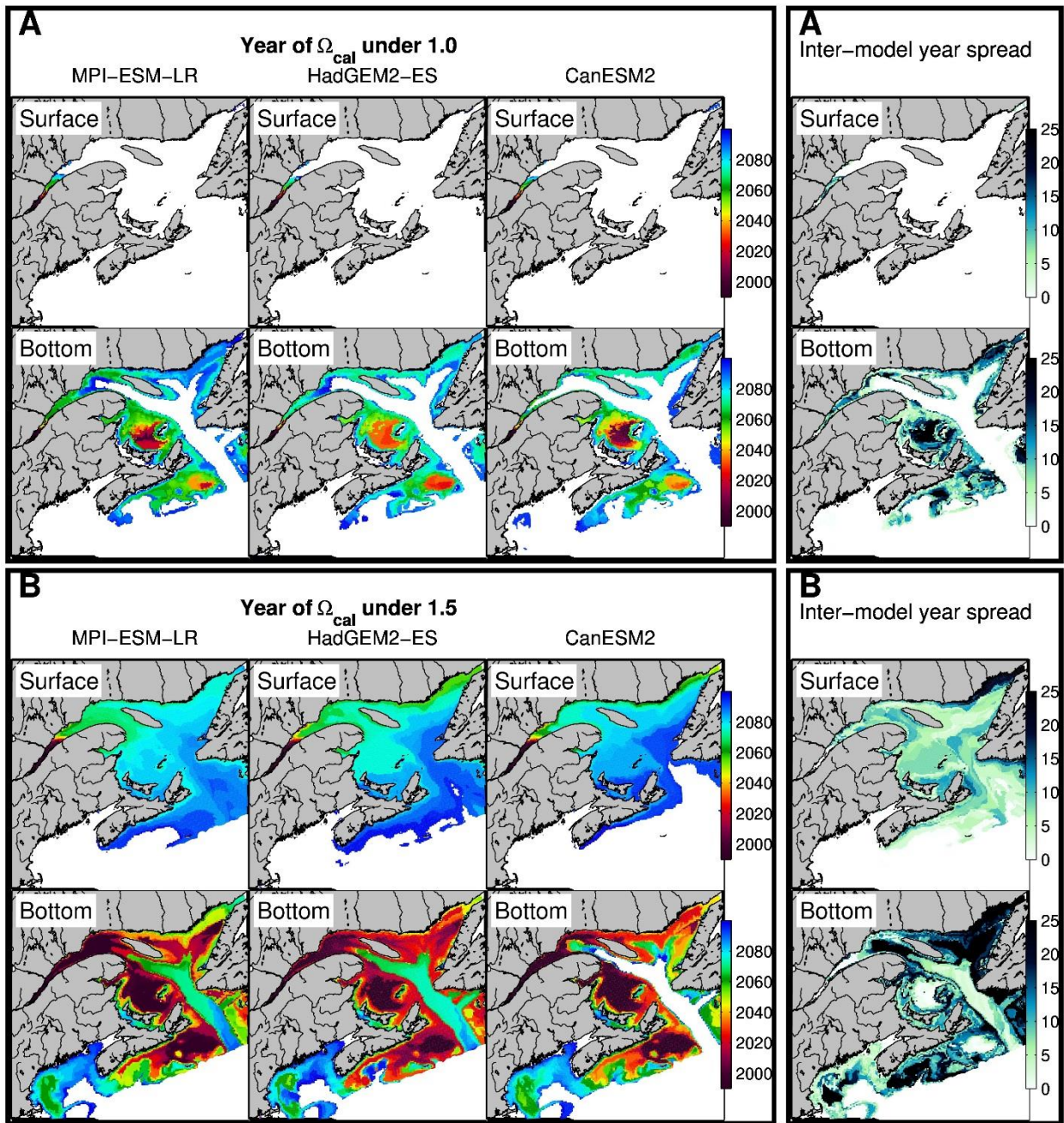


Figure 73. Year at which the surface and bottom calcite saturation states (Ω_{cal}) reach a value of 1.0 (A) and a value of 1.5 (B). White areas mean that saturation states do not reach these critical values during the study period. Right panels show the inter-model change spread in the calculated year.

Cumulative stressor index (2061–2080) minus (1991–2010)

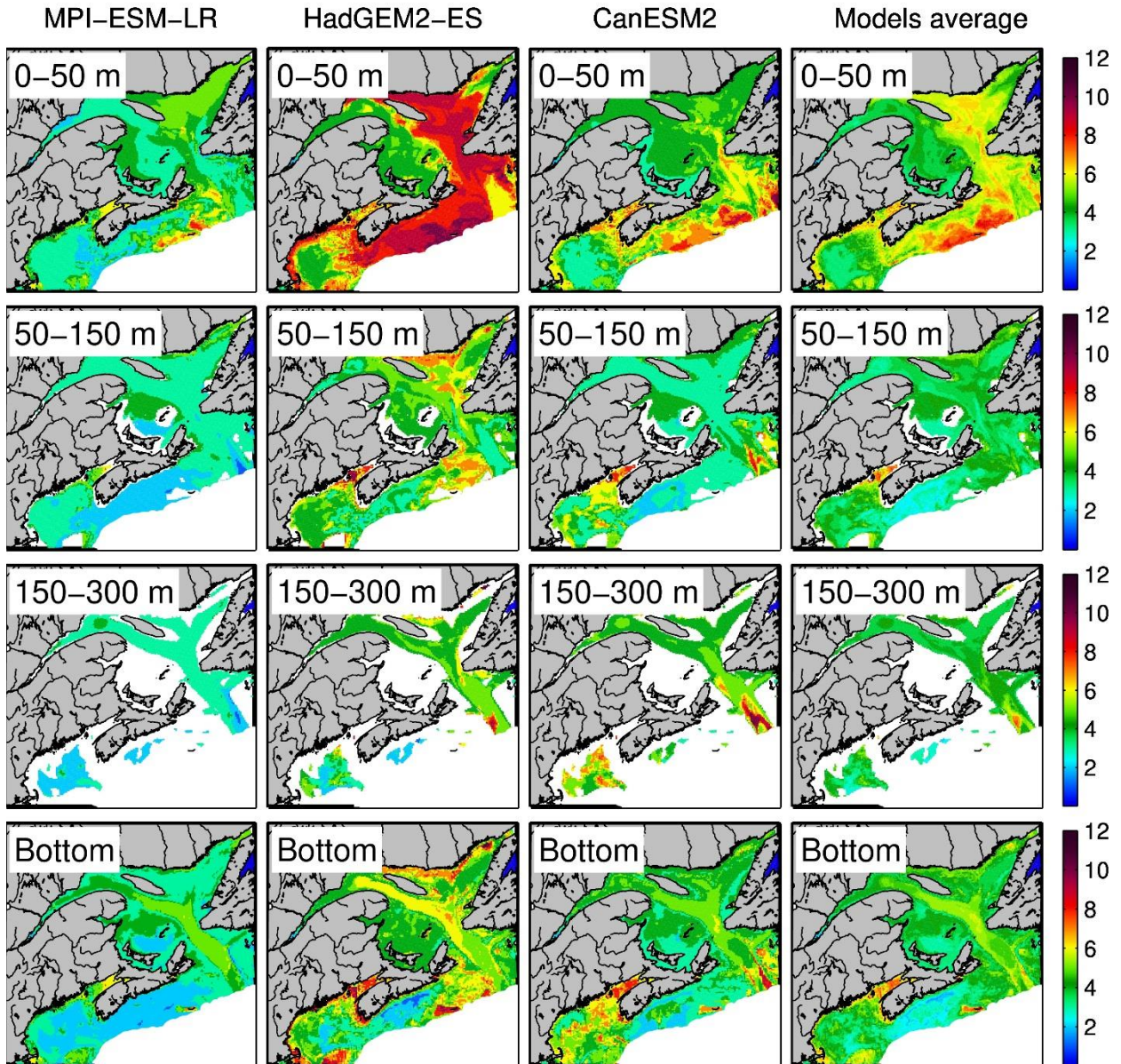


Figure 74. Number of variables in each grid cell that show a change (2061–2080 average minus 1991–2010 average) greater than three times the standard deviation calculated over the historical period. The 12 variables considered are temperature, salinity, nitrate, ammonium, diatoms, flagellates, mesozooplankton, microzooplankton, detrital particulate organic nitrogen, dissolved organic nitrogen, pH, and aragonite saturation. The reader can refer to the bi-decadal change figures for each variable to determine which ones are included here.